ABSTRACT

Title of Document:	BOOSTING ELECTRICAL GENERATION OF A PHOTOVOLTAIC ARRAY BY THERMAL HARVEST FROM p-Si CELLS: AN EXPERIMENTAL AND THEORETICAL STUDY
	Joshua Edward Kelley, Master of Science, 2015
Directed By:	Dr. Michael Ohadi, P.E., Mechanical Engineering

Solar power generation deployment is increasing globally with photovoltaic modules. Most energy available to conventional PV is absorbed as heat or passes through. Performance of Photovoltaic Thermal (PVT) collectors which mimic currently available, polycrystalline, commercial PV modules was measured in the mid-Atlantic US. A linear model is developed for their performance which uses values available in Typical Meteorological Year files and shows daily accuracies to within 11%. Pressure losses for the collectors were measured and an empirical model established. Electrical generation is modeled by PVT in conjunction with an Organic Rankine Cycle. 20% - 45% boosts to electricity production in the Southwest are projected. 5%-15% boosts are projected in the mid-Atlantic.

BOOSTING ELECTRICAL GENERATION OF A PHOTOVOLTAIC ARRAY BY

THERMAL HARVEST FROM p-Si CELLS: AN EXPERIMENTAL AND

THEORETICAL STUDY

By

Joshua Edward Kelley

Thesis submitted to the Faculty of the Graduate School of the
University of Maryland, College Park, in partial fulfillment
of the requirements for the degree of
Master of Science
2015

Advisory Committee:

Professor Michael Ohadi, Department of Mechanical Engineering, Chair
Professor Reinhard Radermacher
Professor Jelena Srebric

Dedication

For Sarah

Acknowledgments

Dr. Michael Ohadi

Dr. Serguei Dessiatoun

Dr. Amir Shooshtari

Veena Venkoba Rao

Table of Contents

List of Figures

Executive Summary

The world needs electricity to satisfy the demands of modern life. However it must meet these demands while balancing greenhouse gas emissions. Photovoltaic (PV) modules are showing a steep increase in deployment (more than 40% year over year growth in Q3 of 2014) while decreasing in installation costs (about a 13% / year drop in Q1 – Q3 2014.)[1] However, the low efficiency of the cells, their inability to be a dispatchable* resource without battery backups, and the large area they cover restrict the potential of the technology.

In a typical solar array, about 50% of the capital cost is included the cost of the system independent of the PV modules. Incident light on the array which is not converted into electricity by the modules is converted into heat, reflected, or passes through the modules to the surroundings. Photovoltaic Thermal (PVT) collectors are examined in this work for the purposes of producing electricity for export to the grid or the system's host's electrical loads in conjunction with the electricity harvested from the

---

* While not all power generation is required to be dispatchable, grid operators require some level of dispatchable resources on hand at all times to prevent cascading events. If intermittent generation's contribution to the grid requirements exceeds some limit, the operator may order the intermittent generation off-line (curtailment.)

semi-conductor PV cells themselves.

This work seeks as its objective to:

1. Construct a model which, based on a selected geometry of a designed PVT collector and known climatic conditions, determines the harvestable energy from the PVT collectors;

2. Project the amount of electricity that might be generated from this energy via an organic Rankine cycle using different PVT collector geometries.

Parameters measured include ambient air temperature, module surface temperature, entrance and exit coolant temperatures, mass flow rates, plane of array irradiance, wind speeds, voltage and current.

Three different novel geometries of PVT collectors (serpentine, single-tube, and double tube) are built and tested in and around the Smart & Small Thermal Systems (S2TS) at University of Maryland under measured climatic conditions. The PVT collectors were constructed with single glazing and a simple insulation scheme with the intention of providing as little deviation with the addition of a PVT collector from a commercially available framed PV module. Their thermal resistances were calculated, and the correlation between their laminate temperatures and the exit water temperatures for set mass flow rates were determined. At the flow rates used, resistances between the cell and the heat transfer fluid used (water) ranged from 0.008 to 0.035 m^2K/W depending upon the geometry of the module.

Thermal efficiencies were calculated by the equation: $\eta_{TH} = q_{Harvest} / q_{POA}$, where

η_{TH} is the thermal efficiency, $q_{Harvest}$ is the heat recovered from the collector, and q_{POA} is the energy available to the harvester's plane of array from the sun. Values of η_{TH} as high as 54% were observed, although instantaneous values were recorded as low as 0% (see Thermal Efficiency of Collectors for details.)

For stipulated weather conditions of 800 W/m² in plane of array irradiance, 25 °C ambient air temperature, and wind speeds of 1.5 m/s[*], mass flow rates were calculated to provide the best performance of the PVT collectors between 2.0 g/s and 3.6 g/s, [m² of module] depending upon the module geometry.

A model was developed which predicts the harvested energy from the modules for a set mass flow rate based upon generally available Typical Meteorological Year 2 (TMY2) data.[†] The model, coupled with a simulated organic Rankine cycle, shows that the PVT system is capable of increasing the electrical production of a generator by approximately 34% relative to a generator driven by a conventional PV system operating under the same thermal characteristics, but without thermal harvesting.

[*] These parameters were selected for general compliance with Normal Cell Operating Temperatures.

[†] TMY data sets are compiled by NREL by selecting typical weather data at a given location in order to produce a typical year. The data are selected from several years of records and are entered into the TMY records in calendar month blocks. Data fields include temperatures, wind speeds, and solar radiation. For further reference, the reader is directed to:

Marion, W., and K. Urban. *User's Manual for TMY2s: Typical Meteorological Years.* Golden, Colorado: National Renewable Energy Laboratory, 1995. Print.

Chapter 1: Rationale for Work and Review of Previous Work

1.1 Introduction

1.1.1 Existing Electrical Needs

Humanity's population presses towards eight billion, developing countries are rapidly industrializing, and the modern world continues to shift into data-driven economies – all of which create needs for energy. The requirements for energy have progressed from those which could be satisfied by fire and photosynthesis into the current requirements which necessitate the immense electrical energy infrastructure of developed countries.

In the United States, much of this electricity is obtained by burning carbon-based fuels or by nuclear power.[2] In a demonstration of energy demand's growth: even during the 2008 recession, carbon fuel demands in Asia increased.[3] A small but growing percentage of the U.S.' energy portfolio is produced by renewable energy sources (wind, photovoltaic, solar thermal, geothermal, wave capture)[4].

These renewable energy sources hold promise for the future as national or even global carbon markets are considered in the public sphere to combat the effects of greenhouse gas (GHG) induced climate change and as the recent disaster at the Fukishima nuclear reactors in Japan remain in the public psyche.

1.1.2 Solar Energy's Trends and Challenges

Of these renewables, solar energy holds promise due to its distributed generation (installing generation assets across the electric grid as opposed to a central power plant) and its output being configurable so that its generation peaks coincide with electric demands.[5] However solar energy is not without drawbacks. It is expensive and receives (in the United States) government subsidies[6]. Photovoltaic collectors are inefficient, with the most efficient p-n cells producing electricity at just 24%[7,8] and with module manufacturers offering commercial modules with efficiencies of less than 19%.[9] Furthermore, the resource is intermittent due to cloud cover, so that at least one utility is now requiring ramp rate control.[10] This rate control could introduce the need for batteries in pure PV installations.

The cost of photovoltaic systems has dropped precipitously in the past several years. Between 2008 and 2012 the system price has fallen about 3.30USD/W. A 2.60USD/W drop in module prices was largely responsible for this price change. This module price drop has caused a larger proportion of a photovoltaic system's price to come from the other pieces of the system (e.g. wires, inverters, and engineering time).[11] So while focusing on reducing the price of modules in 2008 offered a large impact to the total system cost, that impact has been lessened in recent years.

If one considers the means by which a dollar-per-watt calculation is arrived, (price/capacity) it becomes evident that in order to further reduce the installed cost of systems, either the price of these other portions of the system must be reduced or the

capacity which can be derived from them must be increased. Corresponding with this price drop, the global installation of PV increased at an annual rate of 40% in 2010, indicating a sizable increase in the technology base.[12]

The theoretical efficiency of the cells themselves has been found to be limited to 33.7%[13], the so-called "Shockley Quiesser limit." As the cells move towards this limit, the room for improvement in the cells becomes restricted. Some of the efficiency limit is due to the inability of crystalline silicon to absorb light with a wavelength greater than 1.11 μm[14], meaning that any capture of that energy must be derived from other means.

Furthermore, higher efficiency modules have higher costs than less efficient modules.[15] These relative differences of the modules' costs mean that more efficient modules may be cost prohibitive. This is because in solar plants with these modules even the balance of system (BoS) cost reductions associated with the efficiency gains created by the modules are outweighed by the increase in module price.

To summarize: additional increases in module efficiency are becoming more difficult as the gap between commercially available efficiency and the Shockley Quiesser limit becomes smaller. Further increases are also less effective at reducing the total system cost. This troubling confluence suggests looking into other means of generating electricity and energy from PV based systems.

1.1.3 PVT advantages

Photovoltaic thermal (PVT) modules may hold some application in this arena. This work uses a PVT array to generate electricity both from the electron cascade of the

photovoltaic cells and from a harvest of the thermal energy from the modules, which is then converted into electrical energy via some thermodynamic cycle (e.g. Rankine.) Such a system could have several advantages such as:

1. The fixed cost of the BoS would be reduced over a larger footprint, driving the dollar-per-watt down. Since racking, fencing, site preparation work, contractor mobilization, and other labor at the site is either already performed and included in the cost of a photovoltaic system or at least subject to economies of scale, the thermal system it is handicapped by the photovoltaic system. Simply put, the additional dollar-per-watt cost of the entire thermal portion of the system needs to only be equal to the dollar-per-watt cost of the entire photovoltaic portion of the system and its ancillary conditions, not equal to the dollar-per-watt of the modules, in order to have an advantage.

2. Environmental work associated with land use may not change substantially. While a complete treatment of environmental regulations affecting the development of land in the U.S. is well beyond the scope of this work, the timescales can be on the orders of tens of months.[16] By not substantially increasing the size of the array itself, it is hoped that the environmental impacts of the additional capacity from a PVT electric system would be lessened and the time and money needed to develop such projects would remain relatively near their previous fixed costs, again reducing the dollar-per-watt.

3. Curtailment risk of the projects may be reduced. Certain utilities have the right,

under certain circumstances, to curtail unwanted electrical output from the grid.[17]
[18] In the case of solar and wind installations (unlike CCGTs or other fuel based technologies), this financial risk is not partially offset by the avoided cost of fuel which is not burned during a curtailment. Curtailment is further increased by the intermittency of the solar arrays themselves, especially as intermittent generators become more widespread.[19] A PVT array would have some portion of its generation driven by a thermal cycle, with its associated thermal mass enabling a slower ramp rate and potential storage opportunities. Accordingly, it may be possible to reduce the risk of curtailment by implementing a PVT system.

These reasons, among others, form the basis of the rationale for examining PVT as a portion of the electrical generation in a solar array. To date, the bulk of PVT acceptance has been centered on heating air or water[20].

This work seeks to address the following questions:

1. Using a standard poly-silicon module layout as a starting point, how does changing the geometry of heat exchangers coupled to the modules impact the performance of the exchanger?

2. Is enough power extractable from the low temperatures that modules produce to allow an organic Rankin cycle produce energy?

3. If enough power is extractable, how does the total energy extracted from the array's thermal system compare to the electrical system's harvest?

In order to answer these questions, three PVT collectors were built for testing

purposes. (The collector's construction is described in Module Construction.)

These modules were then tested over the course of July and August 2013 in Maryland. Weather data was recorded and some values interpolated. This weather information was subsequently used to build models for the behavior of the modules. These models were then used to extrapolate climatic performance, the results of which in turn show how some areas of the country are more suitable to this application than others, how the climate impacts the operation of the collectors, and what the electrical generation opportunities are from PVT arrays.

1.2 Literature Review

Some previous work has been done on the development of PVT collectors.

1.2.1 Modeling of Collectors

Bergene and Løvvik proposed a complete analytical model for PVT flat-plate modules.[21] These models were constructed around an energy-mass balance of the collector and the use of Kirchoff's laws for optics. They modeled several η_{TH} values for different ratios of tube diameter to spacing between tubes and materials, showing values of over 60% in some applications.

Zondag et al. developed a 3-D, 2-D and 1-D model of the performance of a single-glazed, air gap included, flat plate PVT collector.[22] These models were subsequently checked against experimental data, with which they showed reasonable agreement. They found that a tuned 1-D model produced results similar to the 2-D and 3-D models, but with far less computation time. They caution against blindly adopting the 1-D model without empirical support, as they believe the 2-D and 3-D models will provide better results for varied designs of PVT collectors.

Zhao et al. proposed a PVT system with a flat plate heat pipe for electricity and heat production which used micro channels to reduce thermal resistance in the exchanger and to improve uniformity of the module temperatures.[23] By means of this control, an improvement of η_{Elec} of 15-30% was suggested.

Cristofari et al. studied a PVT module which featured a reverse face insulated with expanded polyurethane, a copolymer absorber, and a 4 mm glass front.[24] The fluid

was uniformly distributed in the module. This module was then numerically applied against domestic requirements. It was found that the use of the copolymer in the module allowed weight of the module to be decreased, while maintaining efficiencies of η_{TH} = 29%, η_{Elec} = 14%, and η_{Elec} = 43%.

Hegenzy analyzed several different models of PVT applications which used air as their cooling fluid and differed in ducting means.[25] He determined, among other things, that the best performance could be had by passing parallel flows of air over and under the PV laminates, that the ideal depth of the air channels had a ratio to their length of 2.5 x 10^{-3}, and that selective PV cells should not be used because they would reduce the harvest of high quality electricity.

Corbin and Zhai produced a CFD model of a PVT system which they installed to examine how building integrated PVT (BIPVT) might be applied.[26] Their module was constructed to emphasize the capture of high quality electricity above the capture of low-grade heat. Using a 10°C water inlet temperature, they were able to parametrically model a 5.3% increase in the electrical efficiency of the module's cells (meaning that η_{Elec} increased by a factor of 1.053). Their η_{TOTAL} was 34.9% and agreed well with the results of a parametric study using the CFD based model.

Chow developed an algorithm to model the performance of a PVT collector dynamically.[27] His technique uses several nodes and thermal resistances. By solving these resistances and nodes, he was able to show more accurate results for the transport of the fluids in a PVT collector and to run this computation on a low-grade computer with

little computational time required.

1.2.2 Experimental Results from PVT Collector Designs

Sandnes and Rekstad performed experiments with a polymer based absorber coupled to a monocrystalline silicon PV module and compared it to a pure thermal absorber.[28] They concluded that introducing the PV to the front of the module reduced the energy harvested by the absorber. They also produced an analytical model that should provide good results relative to the measured performance of the units with a total error estimate of 10%.

Chow et al. worked on a PVT collector designed for electrical production and for naturally circulated production of domestic hot water.[29] They examined the impact of not completely covering the collector with PV cells or simply leaving it totally uncovered. While their experiments indicate that both thermal efficiency and electrical efficiency may be enhanced by applying the PV cells only to the lower half of a module, they are not certain that real world applications of the modules will see the improvements since rainfall tends to drag dirt and soil to the lower sections of modules. Their simulations showed that as the percentage of the module which was covered with cells increased, the η_{TH} decreased and the η_{Elec} increased noticeably.

Fujisawa and Tani designed a PVT collector for purposes of testing via exergy, since they contended that exergy enables an apples-to-apples comparison of the electrical and thermal outputs of the PVT modules.[30] They found that the construction of the module resulted in about the same thermal outputs when the module was constructed

with a single cover as when it was built with a flat plate.

Ito et al. developed an aluminum PVT module made of two aluminum sheets bound together.[31] Although the design was deliberately made to be compatible with existing standard PV module designs, they did not bond the HX onto modules. Using R-22 as the working fluid, they were able to drive a heat pump with a COP of between 4.5 and 6.5. Following some revisions to the design, which decreased the pressure losses of the working fluid as seen in Table 1, the COP was increased by 5-10%.

ΔP	Evaporator Water Temperature	
	30°C	40°C
Type 1	350kPa	290kPa
Type 2	90kPa	80kPa

Table 1– Reported Pressure Losses in the Refrigerant Loop of a Direct Expansion Heat Pump Coupled to a PVT Heat Exchanger

Via the use of feeler bulbs they were able to control the flow of the R-22 relative to the temperature available at the same point in the loop, thereby providing ΔT control to the system. Because the flow rates through the system were low, the Type 2 heat exchanger was designed with the feeler bulb located as near the evaporator exits as practical.

Tripanognostopoulos et al. produced a set of testing results for several arrangements of heat exchangers and insulation in a PVT collector.[32] Their collectors were built in the laboratory and so lacked the finesse that might be expected in a proper manufacturing environment. Their tests were performed primarily around the noon hours, lacking the complete diurnal cycle to which solar installations are actually subjected. In spite of this, they were able to show a linear relation between η_{TH} and a

parameter they defined as $\Delta T/G$. They also found that introducing a second level of glass increased the thermal output at the expense of a decrease of electrical output.

Joshi et al. examined the impact of a glass to glass encapsulation as opposed to a glass to tedlar back sheet encapsulation upon air based PVT.[33] Running their experiments at a New Delhi site, they were able to show only an increase in η_{TH} of about 2% by replacing the tedlar back sheet with a glass reverse face. They were able to develop a model that showed agreement with their thermal results.

Kalogirou and Tripanognostopoulos examined the performance of PVT collectors based upon versions constructed in Greece and then extrapolated via TRANSYS to Madison, Wisconsin.[34] The modules were built with both polycrystalline silicon and amorphous silicon. They concluded that where DHW needs for large installations like office parks or apartment buildings existed in sunny areas, a coupled PVT collector could make economic sense. They saw a lessened economic argument in their simulated Madison site and saw that polycrystalline silicon performed better in all sites than did amorphous silicon.

1.2.3 Implications of PV Cells

Garg and Agarwal studied the implication of using circular cells versus square or rectangular cells and found that for most purposes, the difference in thermal harvest between a solar collector that was totally covered in silicon cells and one totally uncovered in silicon cells was negligible.[35] They further found that a 2 m^2 solar module would be sufficient for about 320Wh of electrical output with a PVT system attached for

the purposes of producing DHW.

1.2.4 Applications of PVT Collectors to Thermodynamic Cycles

Ji et al. performed numerical simulations of a direct expansion solar-assisted heat pump (DXSHP.) This model was able predict relevant thermodynamic properties for the heat pump and showed agreement with the PV electrical and the thermal harvest to within an 8% deviation. They were also able to produce a 2-D model of the exchanger[36].

Zhao et al. examined the application of a PVT module to a residential heat pump application.[37] They determined that the η_{Elec} changes were relatively small for large changes in η_{TH}. For applications in the UK, they believed their results would provide better performance than separated DXHP's and PV arrays.

Tonui and Tripanognostopoulos ran a study on the use of fins in an air-based PVT application with a single axis, fixed tilt tracker.[38] Their experimental results, coupled with their model, gave them η_{TH} increases of 2 percentage points against a flat plate (that is to say, η_{TH} increased by 0.02).

Dubey et al. examined the impact of forced air cooling in the field on the efficiency of the solar modules.[39] They found that for a glass-to-glass module, the efficiency increased by 0.66% by applying ducting to the reverse side of the module.

Ji et al. produced a model of a solar direct expansion heat pump (SDXHP) with heat being provided by a PVT module.[40] The model was designed to produce the thermodynamic properties of the working fluid while the fluid was inside the collectors. The model was found to underestimate the refrigerant losses, but to predict the

efficiencies of the thermal and electrical portions of the system well.

Otincar et al. created a model for the behavior of a concentrated PVT system with triple glazing and the working fluid running over top of the final layer of glazing and the PV cells themselves located behind this last glazing.[41] Applying this fluid to a Carnot cycle and combining the thermal, photoelectric, and Carnot efficiencies, they modeled a total efficiency of 32.3% with proper band gap selection in the working fluids and the PV cells.

1.2.5 Justification for this study

In general, PVT research to date has centered on heat extraction for low grade energy harvest. PVT collectors have also been commonly designed with sophisticated heat exchangers, significant ratios of fluid contact to cell areas, and large differences between the collectors and a traditional module.

These changes create a requirement for substantially different tooling between fabrication lines for traditional modules and the PVT collectors. By examining PVT collectors which could be produced with smaller changes in the fabrication lines, the set up cost of these modules might be decreased.

The study examines PVT collectors which are constructed with smaller fluid to cell ratios, simpler exchangers, and as minimal a difference between the collector and a traditional module as possible.

Chapter 2: Technical Background of Hardware Used in this Work

2.1 Principles of Operation

PVT collectors operate by harvesting both the electrical and the thermal energy of Earth-bound solar radiation. Obviously, these two harvesting means have different modeling descriptions.

2.1.1 Electrical Modeling

Electrical harvesting is done via the photoelectric effect. The cells themselves are impacted by incoming photons from the sun and the photons, if absorbed by the cells' material, knock electrons lose from their respective atoms. As electric fields are applied to the cells front and rear faces, the electrons are carried along the current path as direct current.[42] A common means of modeling the performance of a PV module is some variation of the "single diode model." A single diode model is used as a basis of this work.
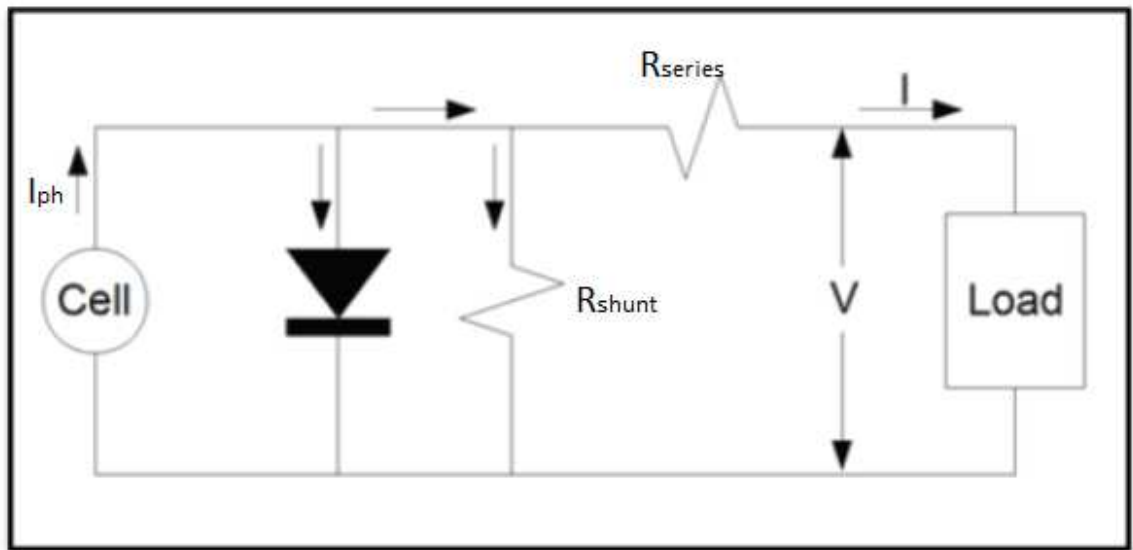
Figure 1 – Single Diode Model Circuit Diagram

The model assumes an internal cell circuit as shown in Figure 1 – Single Diode Model

Circuit Diagram. Mermoud presents an equation for the current, I, and the voltage, V, as

follows:

$$I = I_{ph} - I_0\left(\left(\frac{q_{electron}(V + IR_{series})}{N_{cells}\sigma\gamma T_{cell}}\right) - 1\right) - \frac{V + IR_{series}}{R_{shunt}}$$

2-1

Where: I is the module current, V is the module voltage, T_{cell} is the cell temperature in

Kelvin, I_{ph} is the photocurrent, I_0 is the diode saturation current, R_{series} is the series

resistance, R_{shunt} is the shunt resistance, N_{cells} is the number of cells, γ is the diode quality

factor, σ is the Stefan-Boltzmann constant, and $q_{electron}$ is the electrical charge of an

electron.[43]

This produces an I/V curve such as shown in Figure 2. In general, as the

18

irradiance available to the cells changes, the V_{OC} remains approximately constant while the I_{SC} changes approximately proportionately to the irradiance. The V_{mpp}* shifts slightly as well.
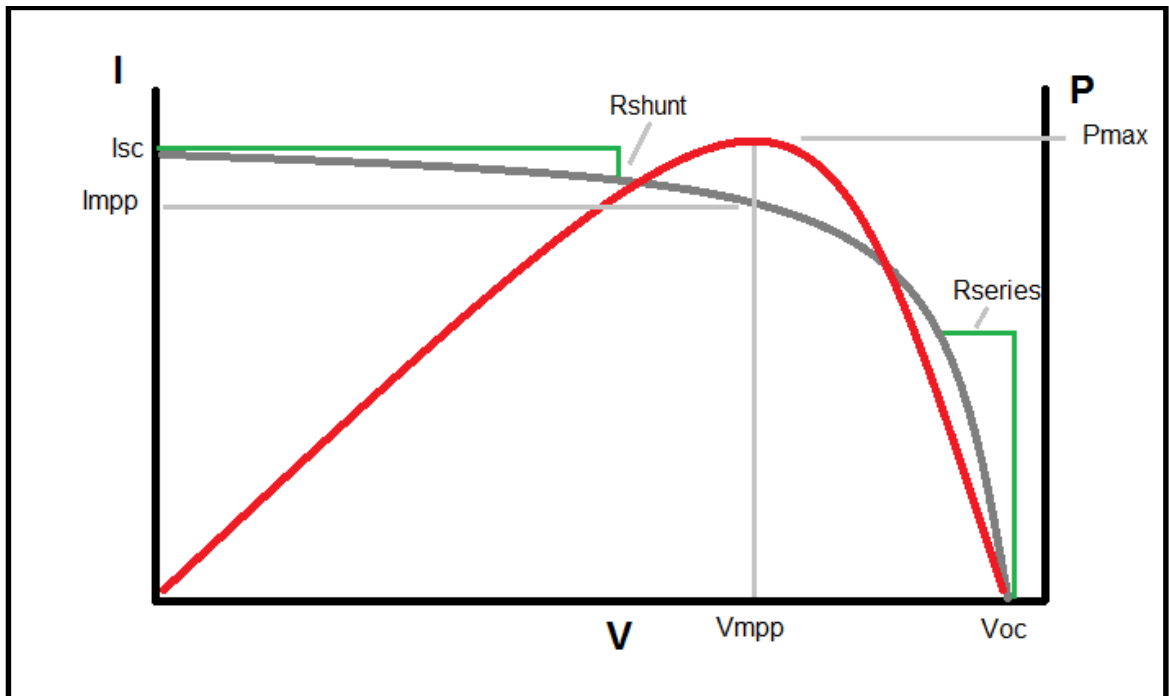
Figure 2 – I/V curve shown in gray, P/V curve shown in red

For any given I/V pair, the electrical power, P, is the product of I and V. From this the power can be determined:

$$P = V \left[I_{ph} - I_0 \left(exp \left(\frac{q_{electron}(V + IR_{series})}{N_{cells} \gamma \sigma T_{cell}} \right) - 1 \right) - \frac{V + IR_{series}}{R_{shunt}} \right]$$

2-2

---

* The maximum power point being the I/V pair such that the P is maximized.

and in order to determine the maximum power's voltage V_{mpp} we have:

$$\frac{\partial P}{\partial V} = I_{ph} - \frac{N_{cells}\gamma\sigma T_{cell}(IR_{series} + R_{shunt}(1 + C_1) + 2V) + q_{electron}R_{shunt}VC_1}{N_{cells}\gamma\sigma T_{cell}R_{shunt}}$$

2-3

where:

$$C_1 = I_0 exp\left(\frac{q_{electron}(V + IR_{series})}{N_{cells}\gamma\sigma T_{cell}R_{shunt}}\right)$$

But setting 2-2 to 0 and solving for V_{mpp} does not yield a clean closed form solution, so solutions are generated numerically.

I_0 is defined thus:

$$I_0 = I_{0,Ref}\left(\frac{T_{cell}}{T_{cell,Ref}}\right)^3 exp\left(\frac{q_{electron}}{\gamma\sigma}\left(\frac{E_{gap,Ref}}{T_{Ref}} - \frac{E_{gap}}{T_{cell}}\right)\right)$$

2-4 [44]

Where E_{gap} is the electron energy gap of the material. E_{gap} is modeled thus:

$$E_{gap} = E_{gap,Ref}\left(1 - 0.0002677(T_{cell} - T_{cell,Ref})\right)$$

2-5

with a literature provided value of $E_{gap,\,Ref}$ of 1.121eV for silicon based cells.[45]

I_{ph} is defined thus:

$$I_{ph} = \frac{G}{G_{Ref}}\left(I_{ph,Ref} + \mu_{I_{SC}}(T_{cell} - T_{cell,Ref})\right)$$

2-6 [46]

R_{shunt} can be determined by the resistance in the region of I_{SC} via:

$$\frac{\Delta V}{\Delta I} = R_{shunt}$$

2-7

where ΔV will be the higher (second) voltage reading since V_{SC} is 0 by definition and ΔI will be the second current reading minus I_{SC}.

γ is a value of between 1.3 and 1.35.

R_{series} can then be determined by minimizing the error resulting from the model and the measurements. [47]

As the process of solving these equations can be computationally intensive, a value of the electrical efficiency can be used:

$$\eta_{Elec} = \eta_{Elec,Ref}\left(1 - \beta\left(T_{cell} - T_{cell,Ref}\right)\right)$$

2-8 [48]

2.1.2 Thermal Modeling

Thermal harvest is reliant upon the ΔT between the coolant (in this work water) temperature and the cell temperatures according to Newton's law of cooling:

$$q_{HTF}^{''} = h_{Conv}(T_{cell} - T_{HTF})$$

2-9

In order to model the thermal harvest, some understanding of the construction of the PVT collector and the energy-mass balance is necessary. If one considers the construction shown below in Figure 3, it is possible to determine the mass energy balance easily. A diagram of the energies involved is shown in Figure 4.
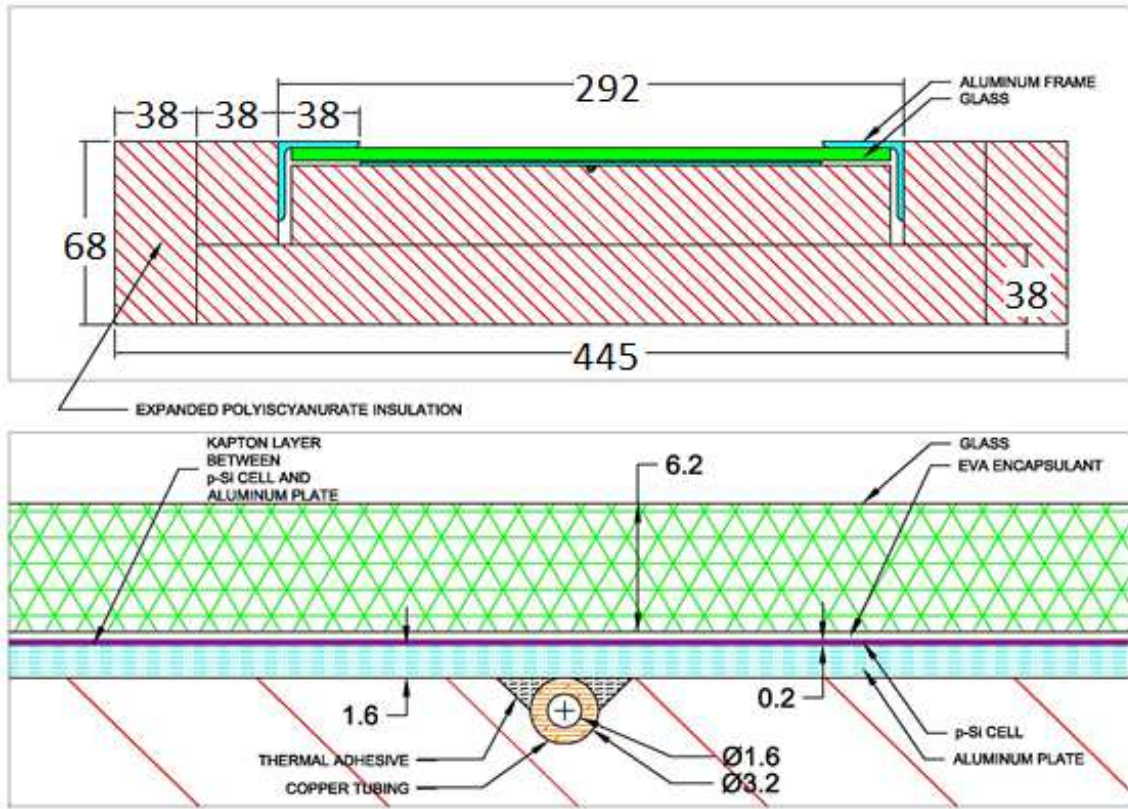
Figure 3 – Equipment Cross Section (Dimensions in mm)

For purposes of this work, energy into the control volume of the collector is considered positive and energy out of the control volume is considered negative.

Therefore conservation of energy dictates:

$$q_{sun} - q_{reflect} - q_{sky,rad} - q_{sky,conv} - q_{back,conv} - q_{elec} - q_{OUT,H2O} - q_{stored} = 0$$

2-10
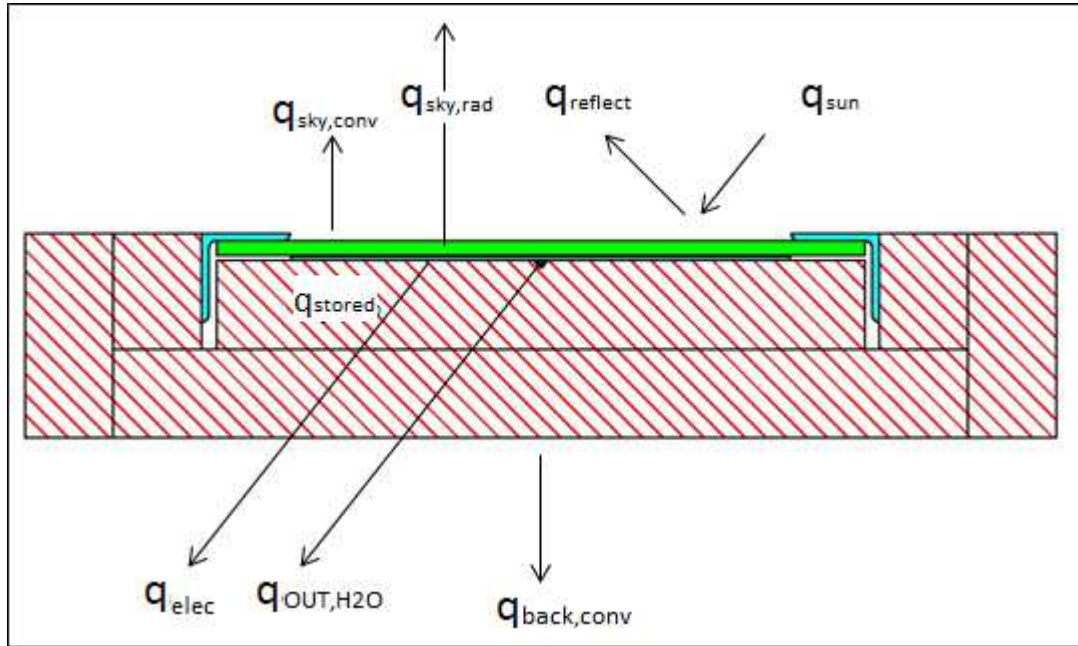
Figure 4 – Energy Balance of Collector

where q_{sun} is the energy rate received as radiation from the sun, $q_{reflect}$ is the energy rate reflected away from the collector which never enters the collector, $q_{sky,rad}$ is the energy rate radiated into the sky and surroundings from the collector, $q_{sky,conv}$ is the energy rate convected into the ambient air from the front face of the collector, $q_{back,conv}$ is the energy rate convected from the rear face of the collector, q_{elec} is the electrical energy rate the PV cells convert, $q_{OUT,H2O}$ is the energy rate of heat removed from the collector via the HTF (water) flow, and q_{stored} is the rate of energy stored in the collector.

Several simplifying assumptions are made in the construction of 2-10's terms. These assumptions are:

1. The system can be modeled in a 0-D, steady-state form without significant loss of information. This is supported by the work of Zondag et al., who determined that

23

time dynamics did not greatly reduce modeling error[49].

Further support of the steady state assumption is given by the low thermal mass of a collector. If one considers the masses of the constituent components in the collector and their specific heats (excepting the insulation), a sum of the product of the specific heat and the mass can be calculated for the collectors. This sum is approximately 4.3kJ/K. For comparison sake, if the collector is subjected to 500W/m² of irradiance and is 80% efficient, this sum would allow the collector's temperature to increase 1°C in 10.7s. This rapid increase supports the concept that changes to the temperature of the collector are accomplished quickly and provide little change to the energy balance of the collector.

2. All energy entering the collector is either reflected or absorbed. That is to say, the transmissivity of the collector is zero.

3. The radiative properties of the cells and the absorber plate are assumed to be the same. This and assumption 2 is supported by the work of Garg and Agawal.[50] For sake of simplicity, the emissivity of the polysilicon, $\varepsilon_{p\text{-}Si}$ is assumed to be 0.80, which is in line with typical values[51].

4. No radiative losses are assumed to exist between the earth and the front face of the collector (that is to say, the view factor between the collector and the sky is unity and between the collector and the earth is zero.) Also, no radiative losses are assumed to exist between the collector's reverse side and the earth (they are assumed to be of approximately equal temperature.)

This work models the terms of 2-10 as follows:

$$q_{sun} = (G_b + G_{Diffuse} + G_{ground})A_{col} = G_{POA}A_{col}$$

2-11

where G_b is the beam component, $G_{Diffuse}$ is the diffuse component, G_{ground} is the ground-reflected component of the irradiance available to the collector, and G_{POA} is the irradiance in the plane of the collector array. These terms can be modeled thus:

$$G_b = \cos(AOI)G_{DNI}$$

2-12

where G_{DNI} is the direct normal irradiance and AOI is the angle of solar incidence of the sun's beams onto the collector.[52] The calculation of the AOI is a simple matter of applied trigonometry and astronomical constants.[53]

For a flat plate collector, the *cos(AOI)* term becomes unity and the G_b term equals the G_{DNI} term.

Several different means of calculating $G_{Diffuse}$ are available; however this work uses the simplest isotropic model, which assumes that the diffuse irradiance is uniformly distributed across the visible sky. This model is:

$$G_{Diffuse} = G_{DHI}\frac{\cos(\theta_{tilt})}{2}$$

2-13

where G_{DHI} is the diffuse horizontal irradiance and θ_{tilt} is the tilt of the collector.[54]

The ground-reflected component describes the incoming irradiance which is seen by the ground and subsequently reflected to the collectors, rather than absorbed. It is

described thus:

$$G_{ground} = \alpha_r G_{GHI} \frac{1 - cos(\theta_{tilt})}{2}$$

2-14

where α_r is the albedo of the ground and G_{GHI} is the global horizontal irradiance.[55]

Reflection is modeled using the ASHRAE IAM model.

$$q_{reflect} = q_{sun} IAM_b$$

2-15

where IAM_b is:

$$IAM_b = 1 - b_0 \left(\frac{1}{cos(AOI)} - 1 \right)$$

2-16

and b_0 is considered a constant of 0.05.[56]

$q_{sky,rad}$ is modeled according to the technique of Zondag et al. [57]:

$$q_{sky,rad} = F_{sky,top} \sigma \left(T_{top}^4 - T_{sky}^4 \right) + F_{earth,top} \sigma \left(T_{top}^4 - T_{earth}^4 \right)$$

which, since the assumption is made that $F_{earth} = 0$, reduces to

$$q_{sky,rad} = F_{sky,top} \sigma \left(T_{top}^4 - T_{sky}^4 \right)$$

2-17

$q_{sky,conv}$ is calculated according to Newton's law of cooling, using the following definition of the Nusselt number:

$$Nu_{L_c} = 0.54 Ra_{L_c}^{1/4}$$

2-18

26

which is valid for $2.6 \times 10^4 < Ra_{Lc} < 10^7$ and where the characteristic length, L_c is:

$$L_c = \frac{Plate\ Area}{Plate\ Perimeter}\text{58}$$

Likewise, $q_{back,\ conv}$ is calculated from a Nusselt number:

$$Nu_{L_C} = 0.27Ra_{L_C}^{1/4}$$

2-19

where L_c shares its definition with 2-18. [59]

Because of the complications with calculating the I/V curve for any given set of conditions, q_{elec} is calculated via the efficiency referenced in 2-8:

$$q_{elec} = \eta_{elec}q_{sun}$$

2-20

$q_{out,\ H2O}$ is calculated via the obvious:

$$q_{out,H_2O} = c_p \dot{m}_{H_2O}(LWT - EWT)$$

2-21

where $\dot{m}_{H_2O}$ is the mass flow rate of the cooling water, LWT is the leaving water temperature, and EWT is the entering water temperature.

2.2 Instrumentation – Direct Parameters

Several parameters are measured for the experiments. These include:

1. Temperatures

2. Wind Speed

3. Irradiance

4. Mass

5. Time

6. Voltage

7. Current

8. Resistance

A description of the means of measurement or calculation is detailed in the following section. A summary table for the relevant measurements appears Table 4 – Summary of Directly Measured Parameters.

2.2.1 Temperature

Temperature is measured via two means: direct equipment temperatures are measured via calibrated T-type thermocouples while atmospheric temperatures (T_{Amb}, WB, and DPt) are measured via the weather station located at Baltimore Washington International Airport. This airport is approximately 29.5km from the test site. The airport's weather station is understood for purposes of this work to be controlled by the National Weather Service standards (NWSI 10-1301.) The temperature readings from the airport are presented in hourly observations.

Temperature instrumentation was generally accomplished by calibrated T-thermocouples, a basic irradiance meter, and a scale for measuring delivered water mass. The T-thermocouples were epoxied into the entrance and exits of the copper tubing from the modules, one was located in the external water supply, another was located underneath the center PV cell (between the cell and the collector plate.) The T-type thermocouples were recorded by means of Visalia SP-1700 thermocouple data loggers.

These data loggers are four channel units and have an ambient temperature sensor in them; however they are not shielded from solar gain and are not appropriate for measuring the T_{Amb} as a result.

Calibration of the T-type thermocouples was accomplished by subjecting them to a high and low temperature reservoir of water and determining their biases. The calibration values are contained in Table 2 – Thermocouple Calibration.

Module	Thermocouple	Indicated Temperature Value	Known Temperature Value
A	EWT	100.0°C	100.0°C
		22.8°C	22.8°C
	LWT	99.8°C	100.0°C
		22.3°C	22.8°C
	Cell	100.1°C	100.0°C
		22.7°C	22.8°C
B	EWT	100.0°C	100.0°C
		22.8°C	22.8°C
	LWT	100.1°C	100.0°C
		22.7°C	22.8°C
	Cell	100.1°C	100.0°C
		22.7°C	22.8°C
C	EWT	100.0°C	100.0°C
		22.8°C	22.8
	LWT	99.8°C	100.0°C
		22.3°C	22.8°C
	Cell	100.1°C	100.0°C
		22.7°C	22.8°C

Table 2 – Thermocouple Calibration

2.2.2 Wind Speed

Wind speed for the site is measured from the BWI weather site. While wind speed is highly localized, the sensitivity of the model to changes in values is generally small.

2.2.3 Irradiance

Local irradiance measurements were conducted by a General Tools DBTU1300 Solar Power Meter. This is a battery operated, handheld diode based irradiance meter. Calibration was accomplished by checking the reading against a secondary class pyranometer at $1,011 W/m^2$ and adjusting the on-device calibration until it read the same values. As the device is handheld, it needed to be maintained in the same plane as the modules. The device has a cosine correction integrated into it.

Since the irradiance meter lacked a data recording function, a local weather station was used for irradiance records during the experiments. The ISIS station in Sterling, Virginia is 45km from the site of the experimental apparatus. This station is equipped with WMO First Class solar pyranometers for GHI and DFI[60] which have hourly achievable uncertainties of 8% for a 95% confidence interval.[61] DNI is measured at this site by an Eppley normal incidence pyrheliometer with a 2% uncertainty.[62]

Irradiance measured at the weather station is based on a G_{DNI} and $G_{Diffuse}$ measurement, which is converted into a G_{POA} measurement by calculating G_b for the collector and adding. Uncertainties are summed and squared for a value of 8.2%.

2.2.4 Mass

Mass was measured by a digital scale with a resolution of 1g and was generally only needed to determine the flow rates of the device. Three measurements were taken with some measurement of time and their collective flow rates averaged.

2.2.5 Time

Time was measured by means of a stop watch. These errors are presumed to be largely dependent upon the human reaction time of the operator of the clock. Based on measurements of the ability of the operator to stop a clock as close as possible to a predefined time (results shown in Table 3 − Operator Error in Stop Watch Signals) it is estimated that the times measured this way have a ±0.2s error.

Run	Time	Error
1	10.36	0.36
2	9.54	-0.46
3	9.93	-0.07
4	10.13	0.13
5	10.08	0.08
6	9.99	-0.01
7	10.04	0.04
8	10.26	0.26
9	10.09	0.09
10	10.18	0.18
	Standard Dev:	0.22

Table 3 − Operator Error in Stop Watch Signals

2.2.6 Voltages

Voltages were measured in two ways. Direct readings of the voltages on the circuits during data collection were taken with a Visalia SP-4000 data logger. These readings were conducted across the terminals of the power resistor. Some voltage drop is present due to the leads of the module and is not captured; however this loss has an approximately constant resistance and the calibration of the modules to their I/V/G characteristics does not include this loss, so it is safe to disregard it.

Secondly, voltages were measured at the leads for the I/V/G characterization with

a Fluke 87 III DMM. Measurement with the DMM was conducted from the terminals of the power resistor as with the voltage data logger.

2.2.7 Current

Currents were measured directly with the DMM. The position of the DMM in the power resistor circuit is not relevant to the currents measured. In the case of currents determined during operation of the data logger, the current is calculated via Ohm's law.

2.2.8 Resistance

Resistances were calculated from the voltage and current measurements. These resistances are generally too low for the DMM to determine accurately. Thus in order to determine the resistances, the voltage and current are measured for a fixed resistance. Several measurements are taken and these values are used in an average to determine the resistance for the power resistor. Since the voltage is measured across the power resistor itself and the leads used in normal operation are not interrupted before the DMM (see Figure 5 – DMM Wiring), the resistance of the DMM becomes unimportant for calculating the voltage and current during the logged portion of operation. An exception to this means of measurement is for the logged portion of Module B's operation, where the DMM was used to directly measure the resistance.

When resistance has not been measured directly, the resistance is calculated as a fixed number which is maintained for a number of voltage / current pairs. The resistance has an uncertainty when calculated thus of approximately ± 0.3%, with slight changes

possible depending on the level of certainty in the DMM's measurement ranges. Resistances were not temperature corrected and the assumption is made for the purpose of this work that once the operator has mechanically set the resistance of the power resistor, it remains a constant.
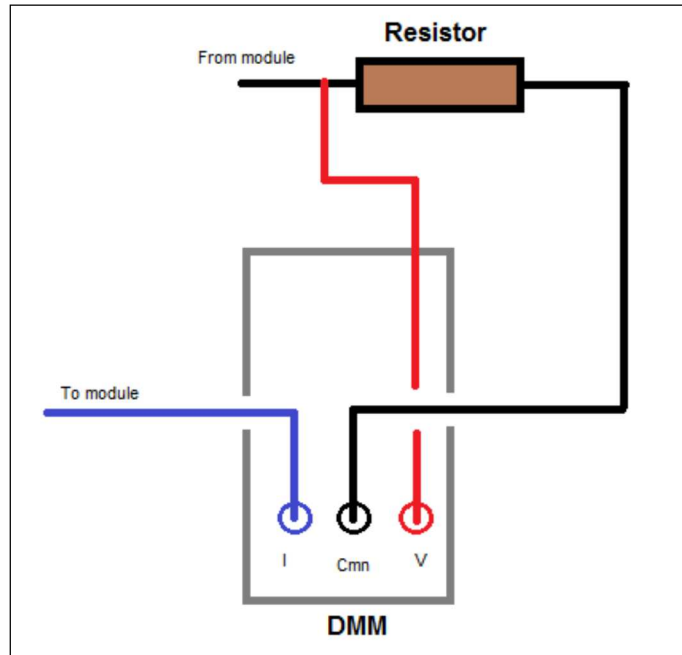
Figure 5 – DMM Wiring

Parameter Direct Measurement Ranges					
Parameter	Instrument	Accuracy	Range	Interval	Resolution
T_{Amb}	Thermometers. Liquid-in-glass or electronic.	±0.6°C	−50to +50°C[63]	Hourly	0.1°C
LWT	T-Type TC	±0.1°C	−270 to 400°C	120s	0.1°C
EWT	T-Type TC	±0.1°C	−270 to 400°C	120s	0.1°C
Cell Temperature	T-Type TC	±0.1°C	−270 to 400°C	120s	0.1°C
Module	Direct voltage	±0.15%	0 to 5VDC	10s	55mV

Parameter Direct Measurement Ranges					
Parameter	Instrument	Accuracy	Range	Interval	Resolution
Voltage – Recorder	measurement	Full Scale Output			
Wind Speed	–	±1knot up to 10 knots; ±10% above 10 knots	2 to 90 knots	Hourly	1 knot
Irradiance – Direct, Instantaneous	Silicon Photodiode	±10W/m² up to 200 W/m²; ±5% above 200 W/m²	0 to 2,000 W/m²	Instant-aneous	0.1W/m²
Irradiance – Global, Record Interval	Spectral Pyranometer	±8%	0 to 2,800 W/m²	3 min	0.1W/m²
Irradiance – Diffuse, Record Interval	Spectral Pyranometer with tracking equipment	±8%	0 to 2,800 W/m²	3 min	0.1W/m²
Irradiance – Direct, Record Interval	Spectral Pyranometer with tracking equipment	±2%	0 to 1,400 W/m²	3 min	0.1W/m²
Mass	Electronic Scale	±1g	0 to 5,000g	N/A	1g
Voltage – Direct Measurement	Digital Multimeter	±0.1%+1	0 to 1,000V	N/A	1mV
Current – Direct Measurement	Digital Multimeter	±0.2%+2	0 to 10A	N/A	1mA up to 4A, 10mA up to 10A
Resistance – Direct Measurement	Digital Multimeter	±0.2%+2	0 to 400Ω	N/A	0.1Ω

Table 4 – Summary of Directly Measured Parameters

2.3 Instrumentation – Indirect Parameters

Several parameters are calculated indirectly and then used later in the analysis. These parameters include:

1. Plane of array irradiance

2. Current

3. Mass flow rate

2.3.1 Plane of Array Irradiance

The instantaneous irradiance meter, due to budget constraints, was only good to ±5% and had no data recording capacity. Uncertainty associated with the recorded values is 8.2%.

2.3.2 Current

Current can be calculated from Ohm's law. Uncertainty in the results is:

Resistance #	Uncertainty
1	+1.1% / -1.0%
2	+1.0% / -1.0%
3	+1.0% / -1.0%
4	+1.0% / -1.0%
5	+1.6% / -1.6%

Table 5 – Resistance Errors

2.3.3 Mass Flow Rate

Mass flow rate can likewise be simply calculated. Each mass measurement was repeated three times. The time involved was fixed at 120s in order to minimize the impact of measurement errors with uncertainty results of ±0.008g/s. Water flow rates

were determined by massing the flow of water through the system for a given time and dividing. No dynamic flow measurements were done, so each set of experiments has been done with a constant flow.

2.3.4 Mass Flow Rate Drift

To estimate the drift rate of the pump for the mass flow rate over the course of several days, the mass flow rate was measured over the course of seven days. Each measurement was repeated in accordance with the dates shown below:

Measurement	Hrs. Elapsed	Flow Rate	% Shift
1	0.0 hrs	1.356 g/s	0.00%
2	19.8 hrs	1.356 g/s	-0.01%
3	43.7 hrs	1.365 g/s	0.65%
4	62.3 hrs	1.398 g/s	3.06%
5	133.8 hrs	1.395 g/s	2.86%

Table 6 – Drift Rate

The average drift rate is calculated to be 0.43%/day.

Chapter 3: Module Construction

Previous work has largely centered on the construction of PVT collectors for the purpose of maximizing the thermal harvest from the modules. Unto this end, various types of glazing and anti-reflective or emissive coatings have been applied to different constructions of the modules. However, the goal of this work was to examine the effect that application of a thermal harvesting heat exchanger to a "baseline," commercially available PV module might have if the module were deliberately insulated.

The rationale behind this "strap-on" heat exchanger extends from the learning curve that has taken place in commercial photovoltaics over the past decades and a desire to develop a technology that, if adopted, will produce the least disruption possible to the manufacturing process of the modules.

Unto that end, the modules were built to be as like unto the existing commercial modules as budget and assembling skills would allow.

3.1 Materials and Assembly

The PV portion of the collector (the representation of a standard solar module) was constructed from Gintech Class B poly-silicon cells measuring 156mm x 156mm, with aluminum tabbing wires. Five of the cells were connected in series in each of the modules. No blocking diodes were installed. Framing for the modules was constructed of aluminum L-brackets measuring 1/8" thick and with legs of 1 1/2" each. These were

cut at 45º bevels and had additional steel elbow brackets screwed into their corners to form rectangular frames.
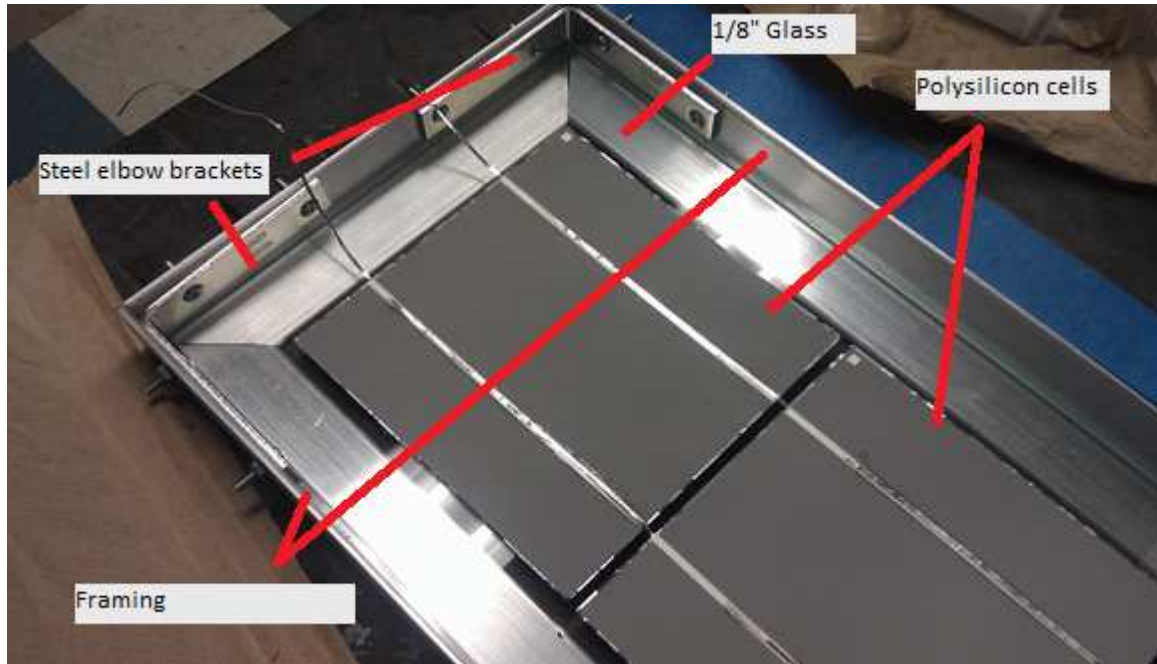
Figure 6 – Portion of typical PV Section of Module

Sylgard 184 was used as an encapsulant. The modules were faced with 1/8" low-iron tempered glass. No anti-reflective coatings were used. A portion of this assembly (sans the encapsulation) can be seen in Figure 6.

Figure 7 – Typical PV Cell

Following the module, the thermal collector was assembled of a large aluminum plate with 0.0625" I.D., 0.125" O.D. copper tubing epoxied onto the plates with Arctic Aluminum AATA epoxy. The plates were roughened before the epoxy was applied in order to gain an appropriate bonding matrix. Unroughened surfaces were found to lose attachment.
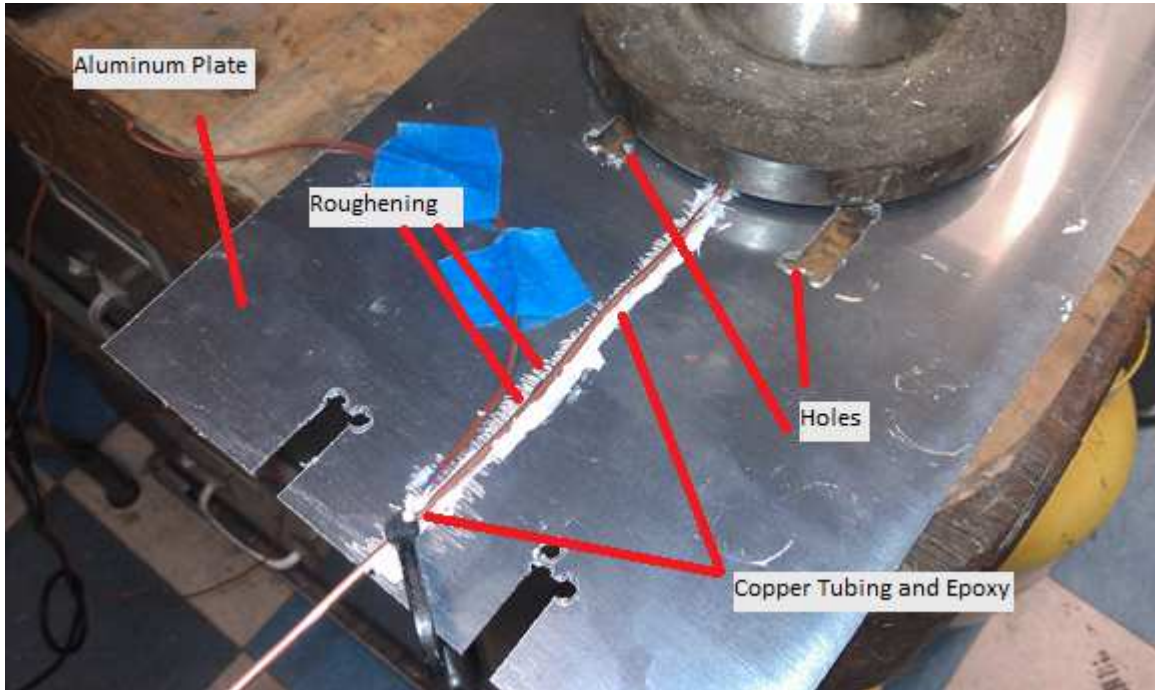
Figure 7 – Typical Collector Plate

The aluminum plate had several holes cut into it in order to accommodate the solder joints in the PV modules. The roughening, holes, and epoxy can all be seen in Figure 7. After this, the rear of the cells was coated with 0.025mm double-sided Kapton which was applied to prevent the conductive rear sides of the cells from shorting to each other via the aluminum plate. A sample string of cells after Kapton application can be seen in Figure 8 (the cells themselves are obscured below the tape.) Following this application of the Kapton, the collectors were adhered to their cells and the modules were encapsulated.
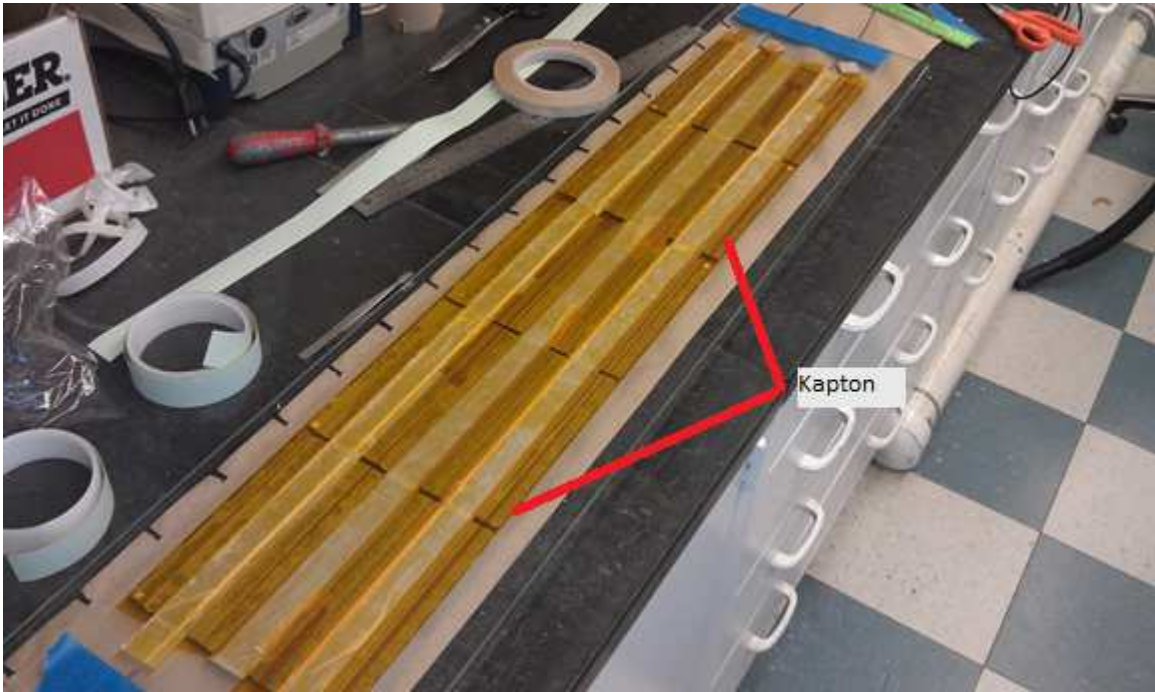
Figure 8 – Cells after Kapton Application

Water was delivered to the collectors by a variable speed metering pump which pumped coolant from a central tank to the cells.

Thermal insulation was added to all faces of the collectors except the glass face. Insulation was expanded cell polyisocyanurate with bonded aluminum foil facers on each side. The insulation was applied in two layers so that it had a total R-Value of 18.8°F·ft²·hr/Btu. The insulation was assembled with adhesive tapes to prevent any fasteners creating a thermal bridge.

A schematic of the components and their locations can be seen in Figure 9.

The electrical system is a simple conductor from the PV cells with a vari-resistor providing the load for the cells. Racking was wooden as this was simplest to construct to match the custom geometry of the cells.
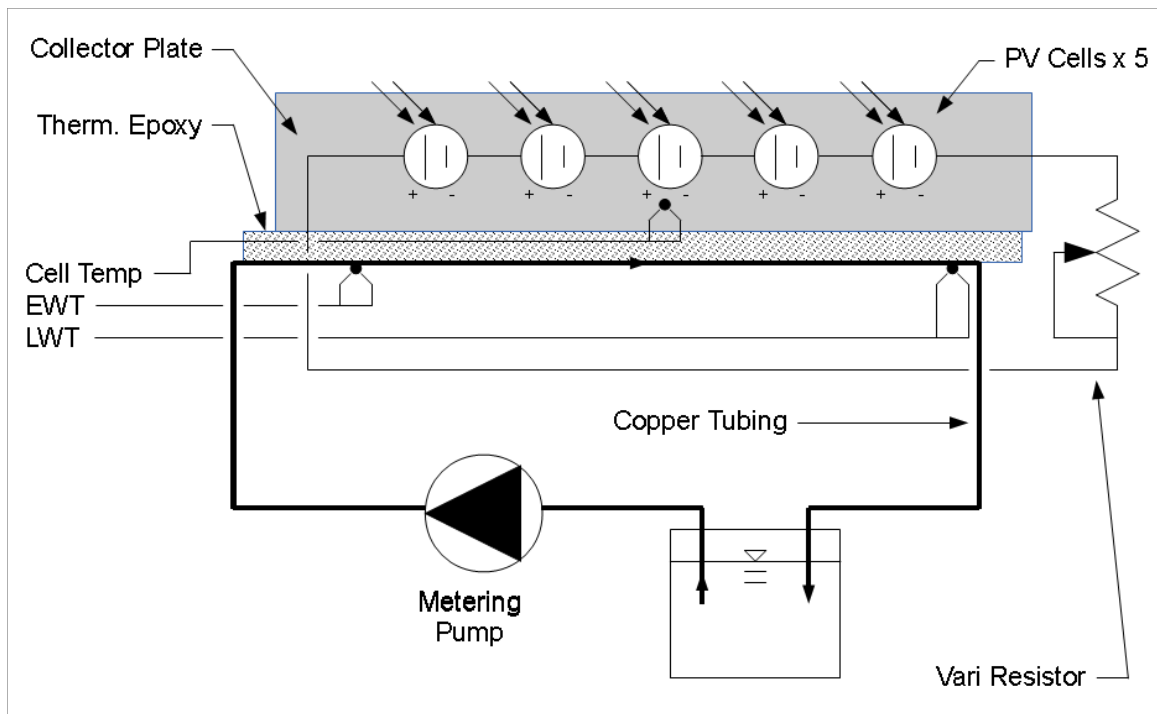
Figure 9 – Schematic of PVT Collectors

3.2 Tubing Layout
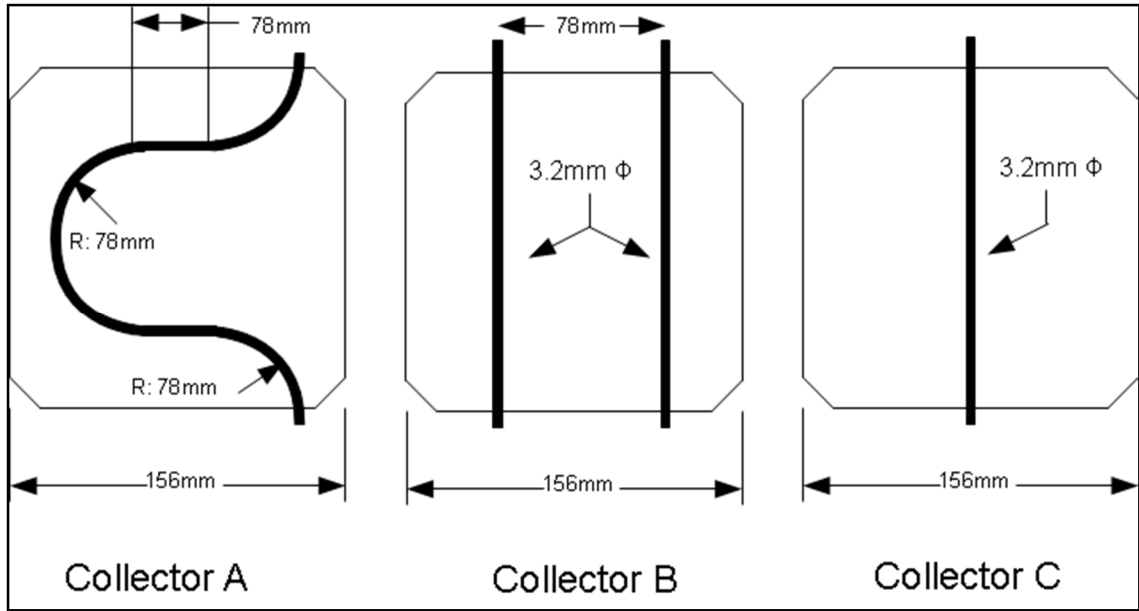
Figure 10 – Collector Tubing Layouts

Geometry of the tubing was varied between each set of collectors. The difference in layouts with their respective geometries is shown above. The modules are described as:

Module / Collector	Verbal Description	Total Tubing Length (m)
A	Serpentine	2.01
B	Double Tube	1.56
C	Single Tube	0.78

Table 7 – Tubing Lengths by Collector

There is no designed difference between the modules except for this tubing configuration variable.

Chapter 4: Experimental Operation

4.1 Data Collection Narrative Summary

Data was collected during daylight and nighttime hours according to the schedules shown in Appendix C - Module Operation Times:. Data collected were subsequently processed according to the equations shown in Technical Background of Hardware Used in this Work − 2.1 Principles of Operation, in order to calculate the parameters for each record shown therein.

4.2 Data Analysis: Energy Balance Model Construction

4.2.1 Data Reduction − Filter 1

Following importation of the data, the records are passed through two filters (Filter 1 and Filter 2) which reduced the data.

Filter 1 is made up of four screens on the data records. These screens follow:

A. If the LWT record was greater than 100ºC

B. If the recorded cell temperature was greater than 100ºC

C. If the difference between the cell temperature and the Mean Water Temperature

(MWT)* was greater than 20ºC

D. If the measured G_{POA} was less than 10W/m² †

The rationale for these checks follows:

A. To capture any errors in the data logging equipment,

B. The same rationale as A,

C. To remove extreme values which may not be representative of the whole of the collected data,

D. To avoid both night time and low irradiance measurement periods during which the energy harvest would be negligible and the data, if introduced, would be noisy.

4.2.2 Calculation of Thermal Energies

Once the data has passed the initial screen of Filter 1, the process of performing calculations according to 2-10 was undertaken. To begin, the values of q''_{sun} versus $q''_{reflect}$ needed to be calculated. Obviously $q''_{sun} - q''_{reflect} = G_{POA}$.

$q''_{reflect}$'s calculation requires knowledge of the angles of the sun at a given hour on the

---

* For this work, MWT = *Average(LWT, EWT)*. For a discussion of the lateral shift in water temperatures, see the Water Temperatures and a Two Dimensional Finite Difference Method (FDM) Model.

† For purposes of Thermal Efficiency of Collectors, G_{POA} can be ignored when T_{cell} to MWT calculations are performed.

modules in order to calculate the IAM_b. The calculations of this angle and the associated angles of incidence between the module and the sun are explained in Appendix A – Calculation of the Angle of Incidence and Associated Module Angles

The calculation of AOI yields IAM_b and enables $q''_{reflect}$ to be calculated. Next $q''_{sky,rad}$ was calculated via 2-17. The area of the modules used is $0.21m^2$ and the emissivity is assumed to be that of the silicon, approximately 0.9. [64] T_{Sky} is calculated via:

$$T_{sky} = \varepsilon_{atm}^{\frac{1}{4}} T_{Amb}$$

4-1 [65]

where the emissivity of the atmosphere is interpolated from values given in the literature.

$q''_{sky,conv}$ and $q''_{back,conv}$ each require calculations of the Nusselt number for their respective surfaces. Since the Rayleigh number which the definition of the Nusselt number depends upon is temperature dependent, these numbers must be arrived via an iterative process.

To begin this process, T_{glass} is first assumed to be the average of T_{Lam} and T_{Amb}. Then:

$$Ra = L_c^3 \frac{g T_{Amb}^{-1}}{\nu \alpha} \left(T_{glass} - T_{Amb} \right)$$

4-3

and Nu_{Lc} may be calculated for that value of Ra_{Lc} by 2-18. Subsequently, a coefficient of cooling for the glass may be calculated via:

$$h_{glass} = \frac{Nu_{Lc,glass}\, k_{Air}}{L_c}$$

4-4

and a new value of T~glass~ may be determined by:

$$T_{glass,new} = T_{glass,old} + Dampener(T_{glass,result} - T_{glass,old})$$

4-5

where:

$$T_{glass,result} = \frac{\dfrac{\delta_{glass} k_{glass}}{A_{col}} T_{Lam} + h_{glass} T_{Amb}}{\dfrac{\delta_{glass} k_{glass}}{A_{col}} + h_{glass}}$$

4-6

and Dampener is a tuned input to cause the solution to converge. It was found that a value of 0.5 worked well for the front surface and that convergence generally happened in fewer than ten iterations.

This process was then repeated for the rear of the collector, with the appropriate changes in the thickness and conductivity from the glass to the insulation, and the use of *2-19* in order to calculate the Nu~Lc~.

q~elec~ is simply calculated for any given record by multiplying the recorded V and the calculated I.

These items thus calculated, q~OUT,H2O,M1~ is determined via 2-21. (This is not the final value that the model will produce for q~OUT,H2O~, hence the M1 distinction.)

4.2.3 Data Reduction – Filter 2

With these steps completed, Filter 2 is constructed. This filter examines each

record which has passed Filter 1's screens and provides additional reduction based on the results of the subsequent calculations. The screens and their rationales follow:

E. The Nusselt numbers for the front and back of the module had to converge for any given record's calculation.

F. The average of the entering and leaving water temperature had to be greater than the measured cell temperature

G. If filters 1 and 2 were met, the record needed to be preceded and followed by two records for which items 1 and 2 were met (i.e. be in a block of at least five good records.)

The rationale for these screens follow:

E. In order for the temperatures for the front and back of the modules to be calculated, the Nu for the front and rear of the modules must converge.

F. Since the purpose of the calculations is to determine the behavior of the modules and the heat exchange in the mode where the HTF is being heated and not cooled, those values which show cooling are rejected. This is determined by checking that the EWT is less than the LWT and that the MWT is greater than T_{Lam}.

G. It is desired that the records used exist in a "block" of good, representative values and not be an intermittent record which happens to pass Screens E and F. In Table 8, examples of records, which would and would not pass are shown. Records passing Screen G have green backgrounds, records which do not pass Screen G have red backgrounds, and records for which not enough information is given (n –

48

3, n – 2, n + 2, and n + 3) are left without a colored background.

Record	Example 1	Example 2	Example 3	Example 4
n – 3	Fails Prior Screens	Passes Prior Screens	Fails Prior Screens	Passes Prior Screens
n – 2	Fails Prior Screens	Passes Prior Screens	Passes Prior Screens	Passes Prior Screens
n – 1	Fails Prior Screens	Passes Prior Screens	Passes Prior Screens	Passes Prior Screens
n	Passes Prior Screens	Passes Prior Screens	Passes Prior Screens	Passes Prior Screens
n + 1	Fails Prior Screens	Fails Prior Screens	Passes Prior Screens	Passes Prior Screens
n + 2	Fails Prior Screens	Fails Prior Screens	Passes Prior Screens	Passes Prior Screens
n + 3	Fails Prior Screens	Fails Prior Screens	Fails Prior Screens	Passes Prior Screens
n Passes Screen G?	No	No	Yes	Yes

Table 8 – Rejection Example

4.2.4 Filter Reduction Rates

These filters have rejection rates as shown:

Filter / Screen	Module A - Serpentine		Module B – Double Tube		Module C – Single Tube	
	Number of Rejections	Rejection Rate	Number of Rejections	Rejection Rate	Number of Rejections	Rejection Rate
Filter 1 / Screen A	0	0%	0	0%	11,826	47%
Filter 1 / Screen B	0	0%	0	0%	0	0%
Filter 1 / Screen C	19	0%	65	2%	162	1%
Filter 1 / Screen D	2,299	32%	985	34%	5,037	20%
Filter 2 / Screen E	1,714	24%	1,311	45%	2,653	11%
Filter 2 / Screen F	582	8%	417	14%	1,445	6%

	Module A - Serpentine		Module B – Double Tube		Module C – Single Tube	
Filter / Screen	Number of Rejections	Rejection Rate	Number of Rejections	Rejection Rate	Number of Rejections	Rejection Rate
Filter 2 / Screen G	134	2%	50	2%	69	0%
Unreduced Records	2,421	34%	76	3%	3,712	15%
Total Records	7,169	100%	2,904	100%	24,904	100%

Table 9 – Reduction Rates[*]

4.2.5 Thermal Resistance Calculation

Once these records have passed their screens they are passed into the calculation of R_{Th}. This is calculated by substituting the heat measured by 2-21, the measured EWT, and the measured LWT into 2-9 and solving for h_{Conv}. h_{Conv} can subsequently be considered the thermal resistance R_{Th} via:

$$R_{Th}q_{H2O,OUT} = (T_{Cell} - MWT) = \frac{q_{H2O,OUT}}{h_{Conv}}$$

4-7

(It is important to recall that the vital ΔT's in this work are a ΔT between the LWT and the EWT and between T_{Cell} and the MWT and that these ΔT's are not interchangeable.)

---

[*]   Many of Module B's readings were rejected as the first set of records did not accord with good engineering sense. The entire experiment for Module B was repeated with a slower recording rate and so the record count is skewed to show more data rejection. The Module C Filter 1 large reject rate is due a faulty thermocouple connection that had to be corrected.

R_{Th}'s value is sought by summing the measurements of $q_{OUT,H2O}$, assuming a value of R_{Th} and calculating a $q_{OUT,H2O}$ for each T_{Cell} / MWT pair via 4-7. The R_{Th} value is then changed until the sum of the measured $q_{OUT,H2O}$ for the operating period matches the sum of the calculated $q_{OUT,H2O}$. These R_{Th} values will thus by definition create $q_{OUT,H2O}$ totals which match the measured values to the calculated values in aggregate[*]. These thermal resistance values follow:

Module	R_{Th}
A – Serpentine	$0.018 m^2 K/W$
B – Double Tube	$0.011 m^2 K/W$
C – Single Tube	$0.040 m^2 K/W$

Table 10 – Thermal Resistances

4.2.6 MWT Use in R_{Th}

During construction of the collectors, the thermocouples installed into them were intended to allow measurement between a sensor installed to monitor the water temperature directly behind the cell temperature sensor and the LWT and EWT. In practice, the ΔT between the cell sensor and the water temperature thermocouple was

---

[*]   The EBM produces records for each time interval in the measurements. That is to say that for each Δt, the EBM makes a set predicted harvest. This is completed regardless of the size of the Δt (whether on the order of seconds, minutes, or hours) and without contemplation of the amount of noise injected into the model. In practice, since TMY values are commonly measured in hourly increments from either satellite or ground observations at the sites in question, for gross predictive purposes some increase in the time resolution's duration is entirely acceptable if it improves the data fit.

commonly small enough (on the order of 0.1°C) that measurement error became a dominating factor. However, use of thermocouples attached to points above the LWT and EWT measurement points was not feasible at this juncture, as the collectors had been encapsulated and could not be disassembled.

MWT was assumed as a replacement to this instrumentation issue because it was possible to calculate from the measured data. This results in an overstated ΔT as can be seen in Figure 11, but FDM simulations (explained in Water Temperatures and a Two Dimensional Finite Difference Method (FDM) Model) show the values to be relatively constant.
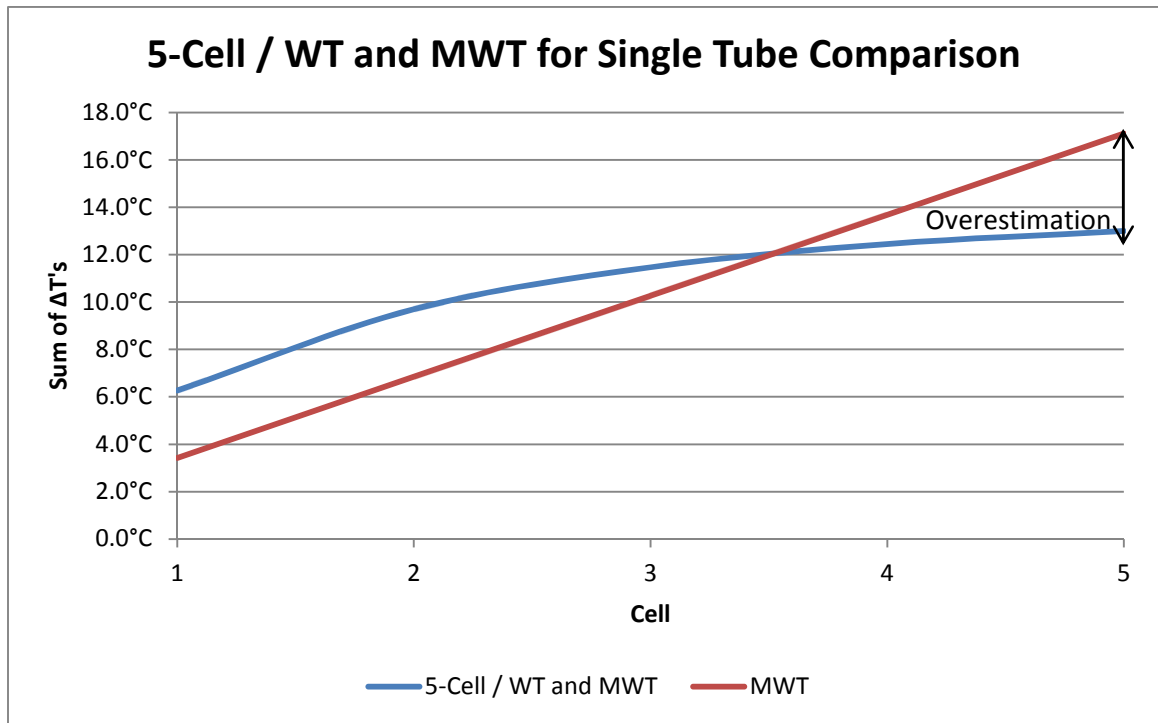
Figure 11 – Overestimation from MWT to 5 Cell / WT

The overestimate can be compared by showing the difference between the cell

and water temperature for each of the five cells, relative to the MWT. This was done and results for different irradiances with associated ΔT's are shown in Figure 20. Corrective factors applied later in the text help reduce the over estimation of thermal input to the array which would otherwise be present. An important fact for the linear thermal resistance approach shown later is that the overestimations are fairly constant.
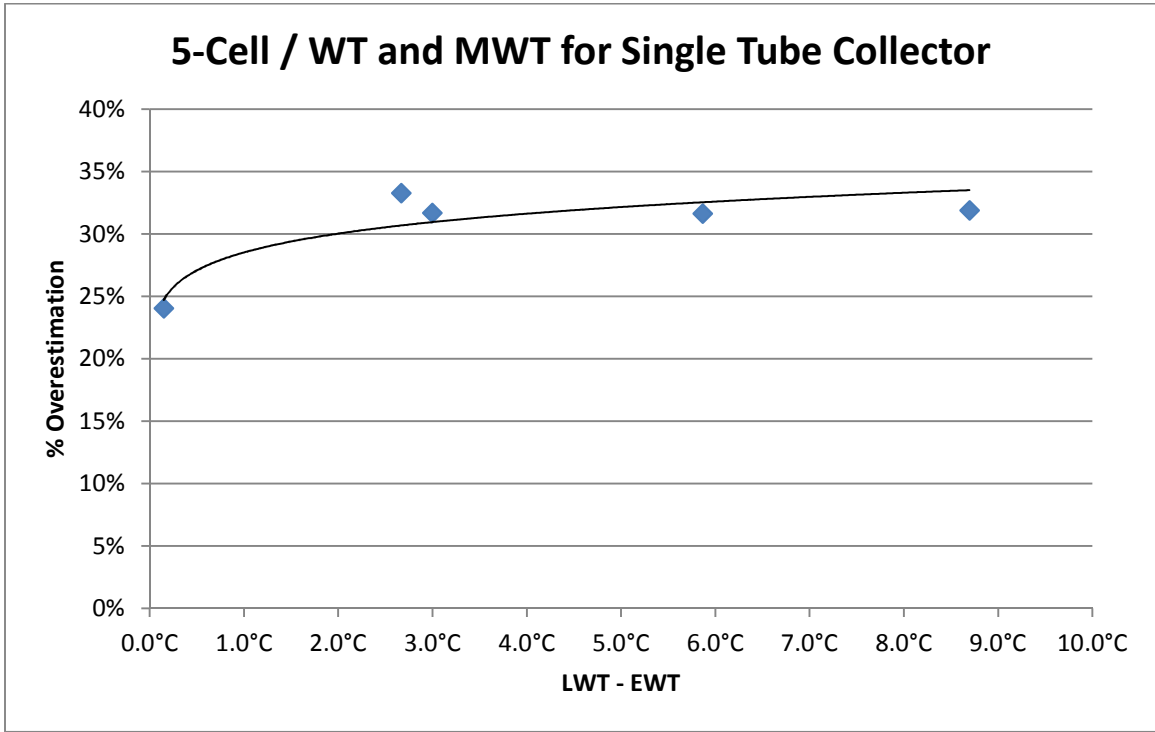
Figure 12 – Overestimated ΔT
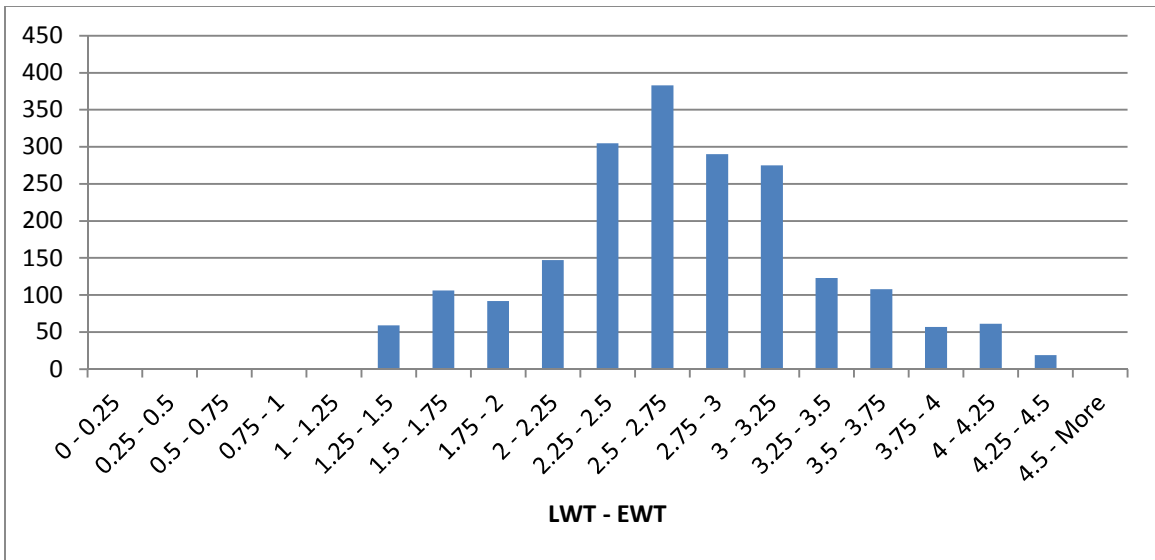
Figure 13 – Histogram of LWT – EWT for Serpentine Module A

54
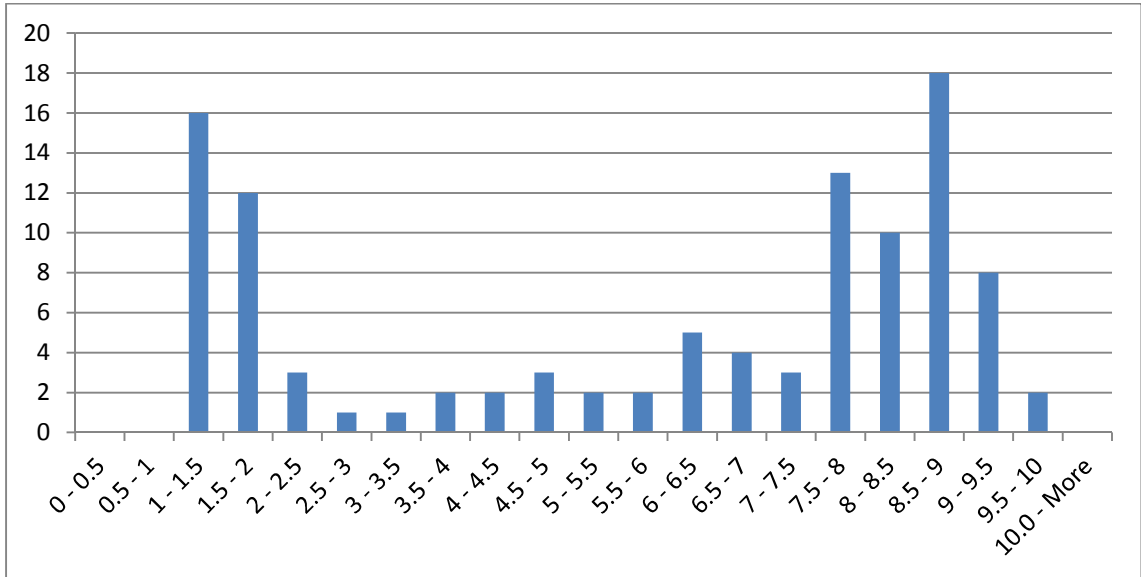
Figure 14 – Histogram of LWT – EWT for Double Tube Module B
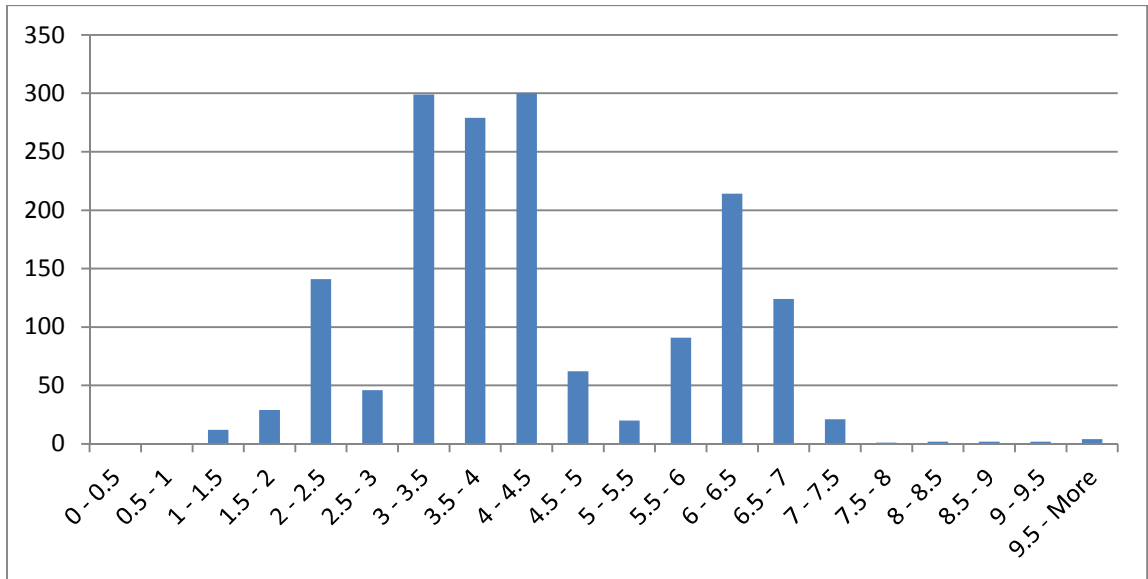
Figure 15 – Histogram of LWT – EWT for Double Tube Module C

4.2.7 LWT / T_{Cell} Correlation

For purposes of calculating the water temperatures, a linear fit of the LWT relative to the T_{Cell} was calculated according to:

$$LWT = m_{LWT/T\_Cell} * T_{Cell} + b_{LWT/T\_Cell}$$

4-8

The parameters resulting from this fit are listed in Table 11 and plots are shown in Figure 16, Figure 17, and Figure 18. The Pearson Coefficients are near unity and as can be seen in the plots, these points fit a linear match very well. It should be self-evident that these intercepts are intimately related to the mass flow present at the collectors (see Thermal Efficiency of Collectors for further discussion.)

Module	Slope m_{LWT/T_Cell}	Intercept b_{LWT/T_Cell}	Pearson Coefficient
A – Serpentine	0.968	10.7	0.993
B – Double Tube	1.15	-42.3	0.992
C – Single Tube	0.929	21.8	0.992

Table 11 – Linear T_{Cell} Parameters
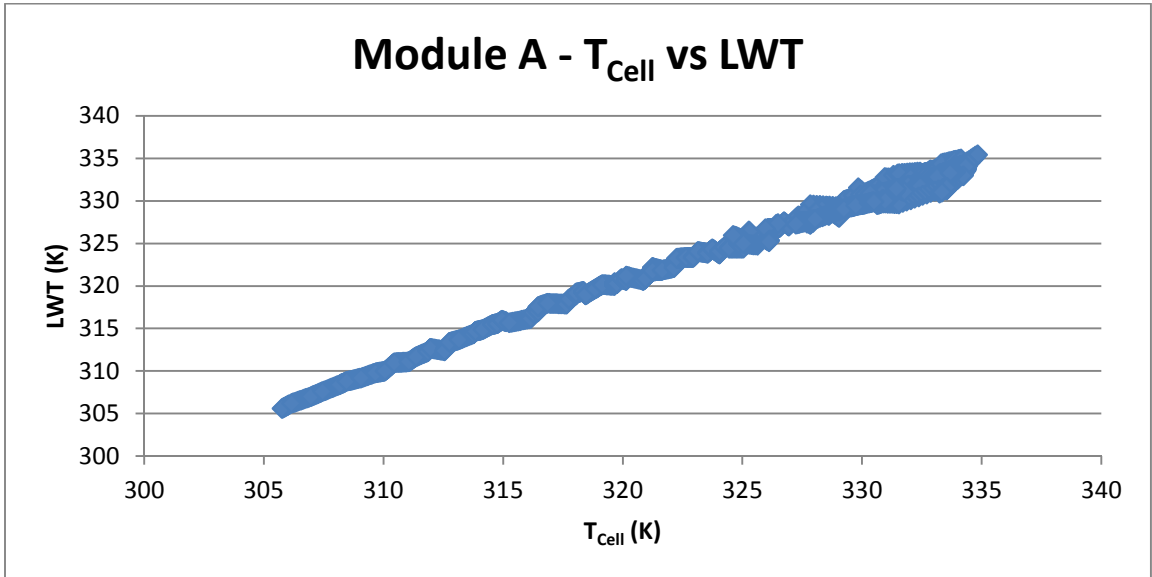
Figure 16 – Module A T_{Cell} vs. LWT
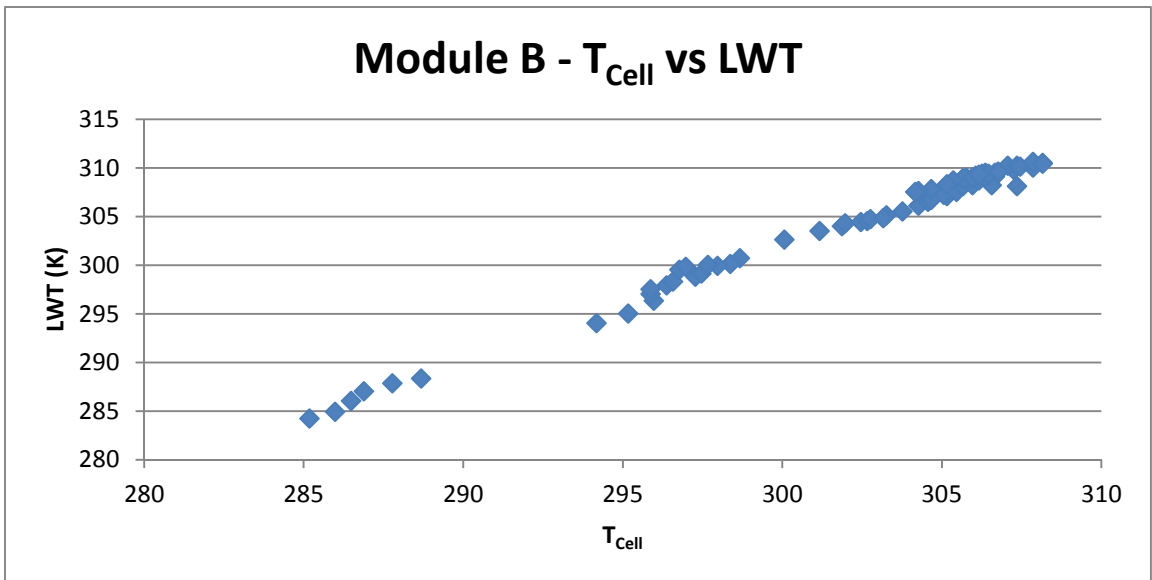
Figure 17 – Module B T_{Cell} vs. LWT
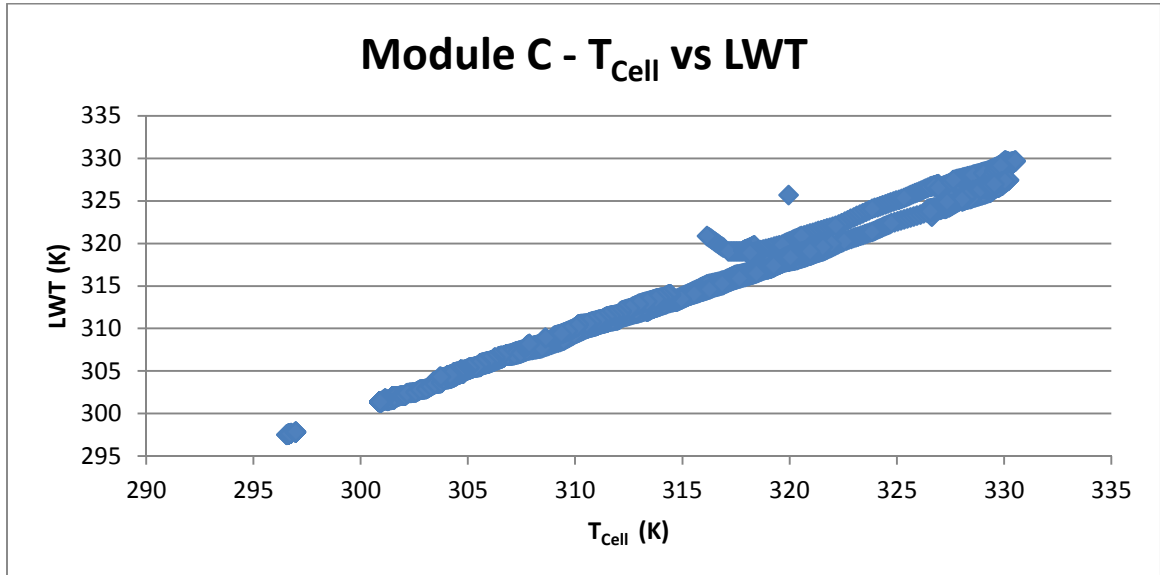
Figure 18 – Module C T_Cell vs. LWT

4.3 Discussion of Use of Non-Local Data

The weather station data used was measured at Dulles International Airport. Some additional uncertainty was introduced into the measurements of the irradiance. In order to estimate an outer bound of this uncertainty, historical irradiance data for two decades (1991 to 2010) was examined from the National Solar Research Database for Dulles and Baltimore Washington International (BWI) airport. The global horizontal irradiances for these years were compared to each other and a distribution of their hourly records' differences was calculated. This difference is intended to serve as an outer bound of the differences between the Dulles data used and the data at the measurement site, since the measurement site is approximately on a line between Baltimore Washington and Dulles.

The differences in hour-by-hour data are summarized below:

Average Absolute Difference	36W/m²
Standard Deviation of Absolute Difference	76W/m²
Average Absolute Difference as a Percent of the Average of the Two Measurements	14%
Average Standard Deviation of the Difference as a Percent of the Average of the Two Measurements	27%

Table 12 – Hour By Hour Data Difference Summary

Obviously the sizeable individual record uncertainty contributes to the hourly variance of the model.

To determine the impact to the measurements as a whole, a Monte Carlo simulation was run, assigning random measurement errors to each module's filtered irradiance records based upon the distribution of differences between the BWI and Dulles records. These simulations were normalized to reflect the fact that the calculation of R_{Th} would have normalized the results and the 95% confidence intervals of the sum of the irradiance records was calculated. These results follow:

Module	95% Confidence Interval for Duration of Measurements
A – Serpentine	±1.94%
B – Double Tube	±9.92%
C – Single Tube	±2.16%

Table 13 – Confidence Intervals of Irradiance Measurements over Operation

Module B shows a much higher uncertainty because of the lower count of records (under 200) relative to Modules A and C. With a higher number of records, Module B would have a lower irradiance uncertainty.

Chapter 5: Energy Balance Model

5.1 Initial Fit of EBM

Since the R_{Th} value is set such that the modeled value of $q_{OUT,H2O}$ must match the measured value of a $q_{OUT,H2O}$ when using measured values of EWT, LWT, and T_{Cell}; there is no way to evaluate the fit of the EBM without modeling the relevant parameters of the operation of the module from the data which would be available to the end user on the basis of a TMY file. Accordingly, the G_{POA}, T_{Amb}, DPt, WS, and $\dot{m}_{H_2O}$ recorded for the entire measurement period are fed into a copy of the EBM and the $q_{H2O,OUT}$ recalculated based upon these measurements. This copy models T_{Cell} according to the method outlined in *Appendix B - Modeling TCell from Available Climatic Data*. By using the R_{Th} values calculated above, the energy available for harvest can be subsequently modeled.

Examination of the EBM to the measured harvest values shows a poor fit as a "baseline" EBM when evaluated on an hourly basis. A bar chart for each of the modules can be seen in Figure 19 – Module A Production by Hour based on Baseline EBM, Figure 20 – Module B Production by Hour based on Baseline EBM, and Figure 21 – Module C Production by Hour based on Baseline EBM for the relevant hours which shows the $q_{H2O,OUT}$ measured as a function of the hour of the day plotted alongside $q_{H2O,OUT}$ as it is modeled with a baseline EBM.
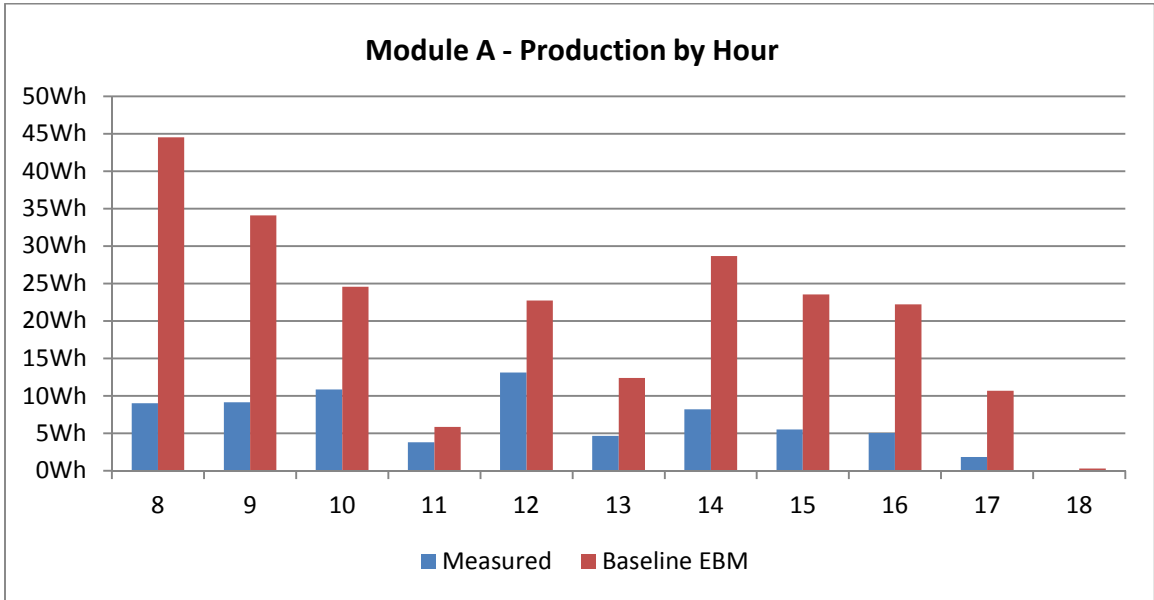
Figure 19 – Module A Production by Hour based on Baseline EBM
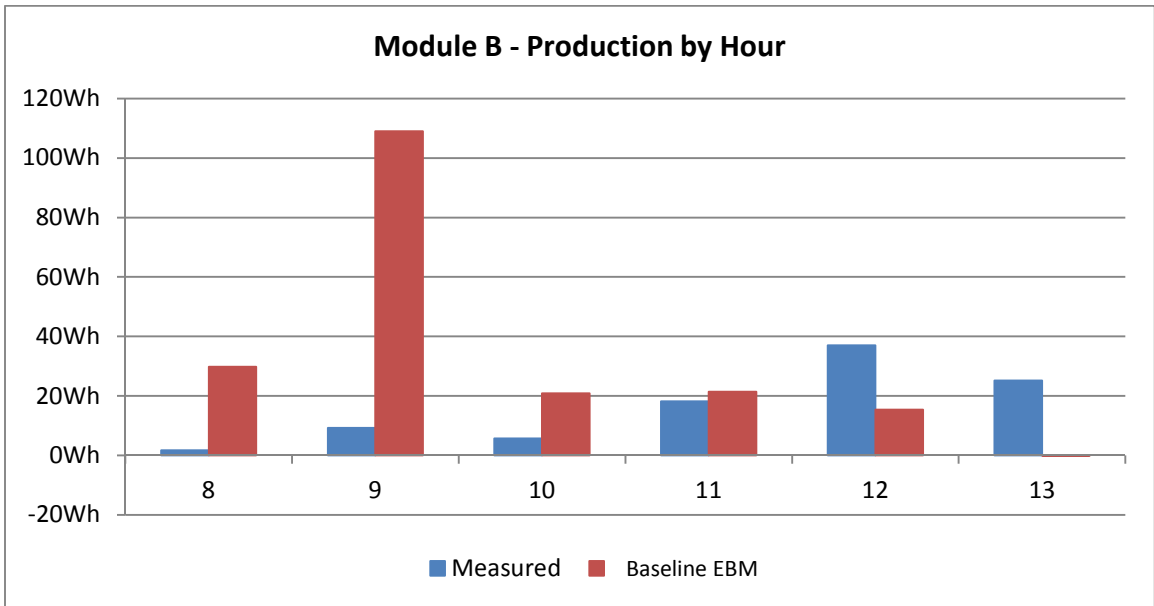
Figure 20 – Module B Production by Hour based on Baseline EBM
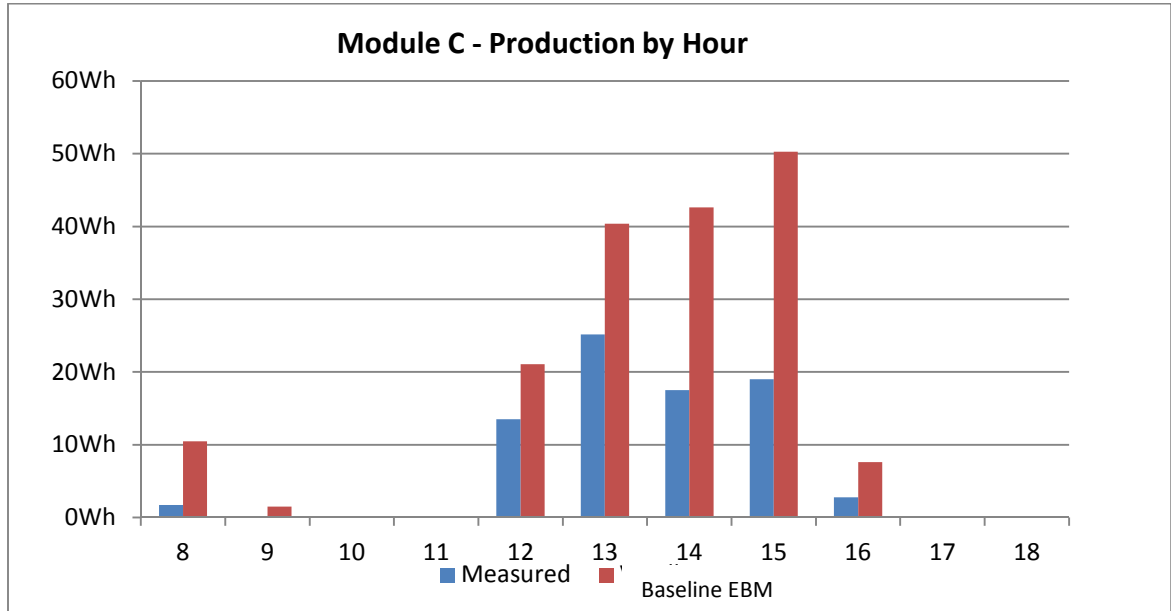
Figure 21 – Module C Production by Hour based on Baseline EBM

5.2 Corrective Parameters for the Energy Balance Model

Since the baseline EBM does not accurately represent the measured values, a set of linear corrections is introduced to the model. These corrections applied to the error in the modeled $q_{H2O,OUT}$. This is given a parameter symbol Ξ_G and calculated thus:

$$\Xi_G = \dot{m}c_p(LWT - EWT) - q_{OUT,H_2O,M1}$$

5-1

Several parameters were considered for correlation against Ξ_G in this correction with the final parameter selected being G_{POA}. As can be seen in Table 14, though certain temperatures show a higher Pearson coefficient for individual modules on the first error, G_{POA} shows the average highest value across all Module A and B. Module C shows a lower coefficient which may be due to the smaller range of G_{POA} available on this

module. However, using the G_{POA} parameter for Module C does not reduce the next

correction's coefficient as, as shown in Table 15.

Parameter	Module A	Module B	Module C
G_{POA}	0.813	0.949	0.0806
T_{Amb}	0.393	0.731	0.036
T_{Cell}	0.834	0.820	0.453
EWT	0.826	0.824	0.458
LWT	0.853	0.838	0.492

Table 14 – Pearson Coefficients Against Ξ_G

Parameter	Module C
G_{POA}	0.000
T_{Amb}	0.093
T_{Cell}	0.654
EWT	0.658
LWT	0.727

Table 15 – Pearson Coefficients After LPC1

5.2.1 Linear Parameter Correction 1

This data supported the use of the G_{POA} values to perform a linear parameter correction

(herein called "Linear Parameter Correction 1" or "LPC1".)

This parameter is linearly matched against G_{POA} and coefficients are established to

map the estimate of Ξ_G, called ξ_G, against G_{POA}. These values are shown below in Table

16. Plots for each of the modules G_{POA} against Ξ_G are included in Figure 22 – Module A

Corrections for G_{POA}, Figure 23 – Module B Corrections for G_{POA}, and Figure 24 –

Module C Corrections for G_{POA}.

Module	Slope ($m_{G\xi}$) (Wh/[W/m^2])	Intercept ($b_{G\xi}$) (Wh)
A	-0.34	111
B	-0.31	107
C	-0.08	10.5

Table 16 – Linear Parameter Correlation Slope / Intercept
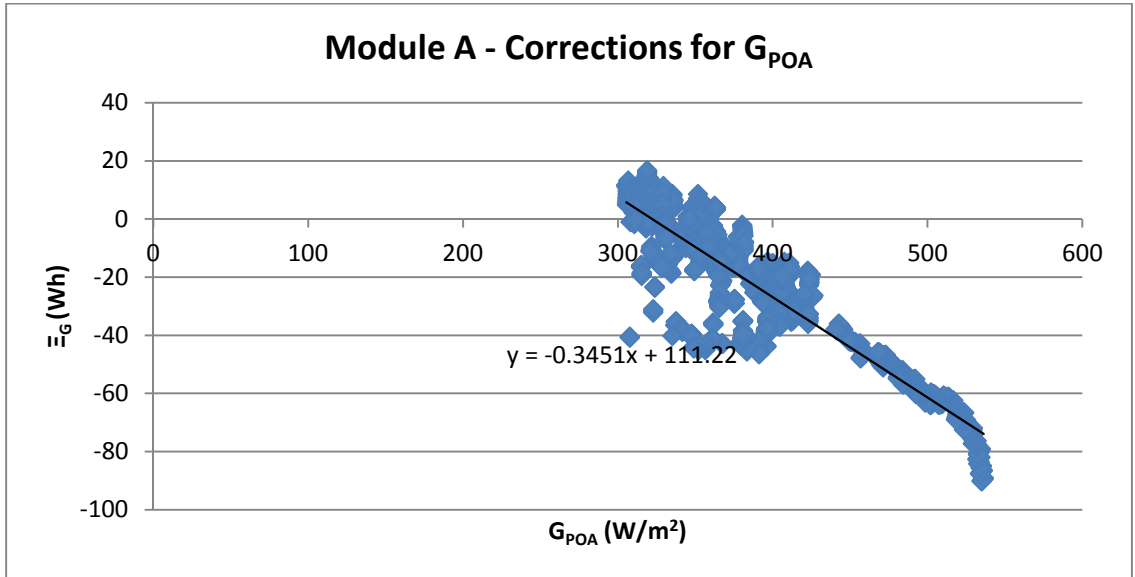
Figure 22 – Module A Corrections for G$_{POA}$
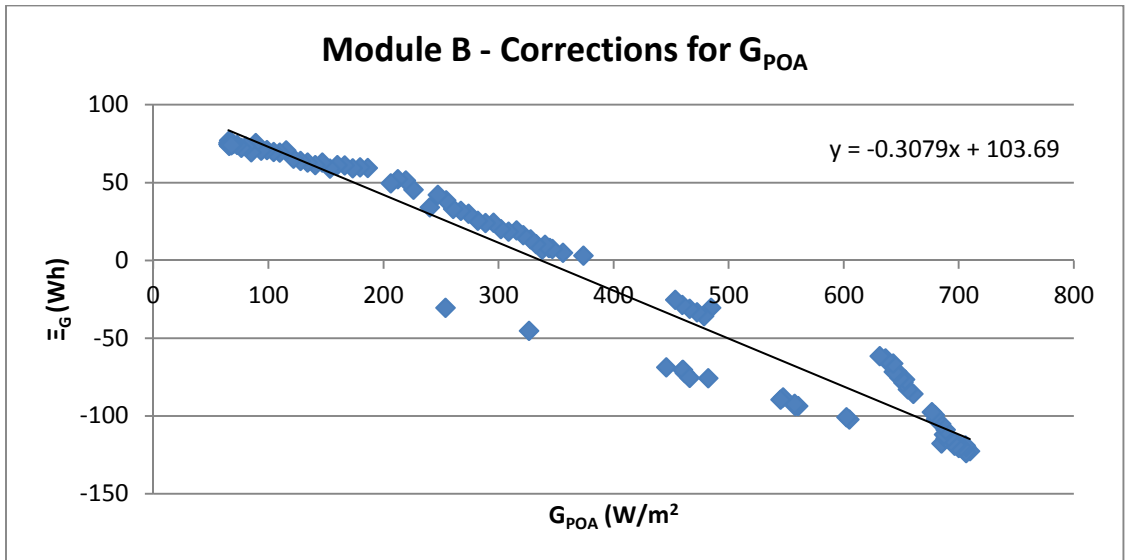
Figure 23 – Module B Corrections for G$_{POA}$
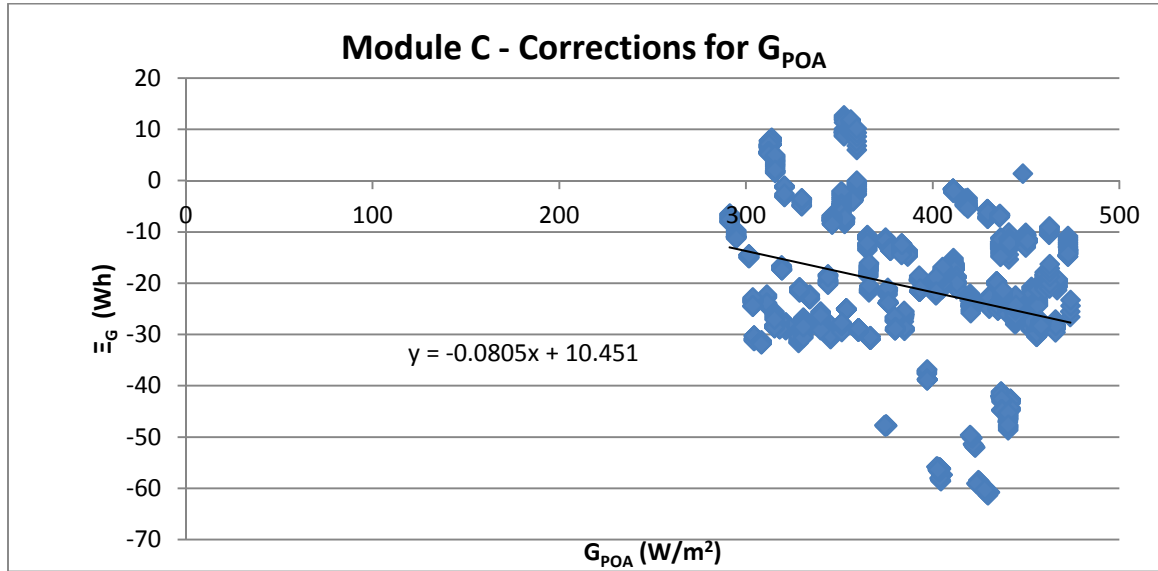
Figure 24 – Module C Corrections for G$_{POA}$

Observing the plots between ξ_G and G$_{POA}$, shows a consistent tendency for the negative error in the baseline EBM to increase as the G$_{POA}$ increases.

Module A and B show a linear error. Since the baseline EBM harvest calculation relies heavily on several calculations which are tied to G$_{POA}$ (q$_{sun}$, q$_{elec}$, q$_{reflect}$), this parameter's measurement drives error in the model. By defining a value, Ξ_T, a second error can be calculated between ξ_G and Ξ_G:

$$\Xi_T = \Xi_G - \xi_G$$

5-2 – Definition of Ξ_T

This represents the difference between the linear parameters in 4-8 and the measured values. This parameter will be used later on. It is possible to calculate the values of the difference between the linear fit and the measured values as shown Figure 25 – Illustration of Ξ_T.

67
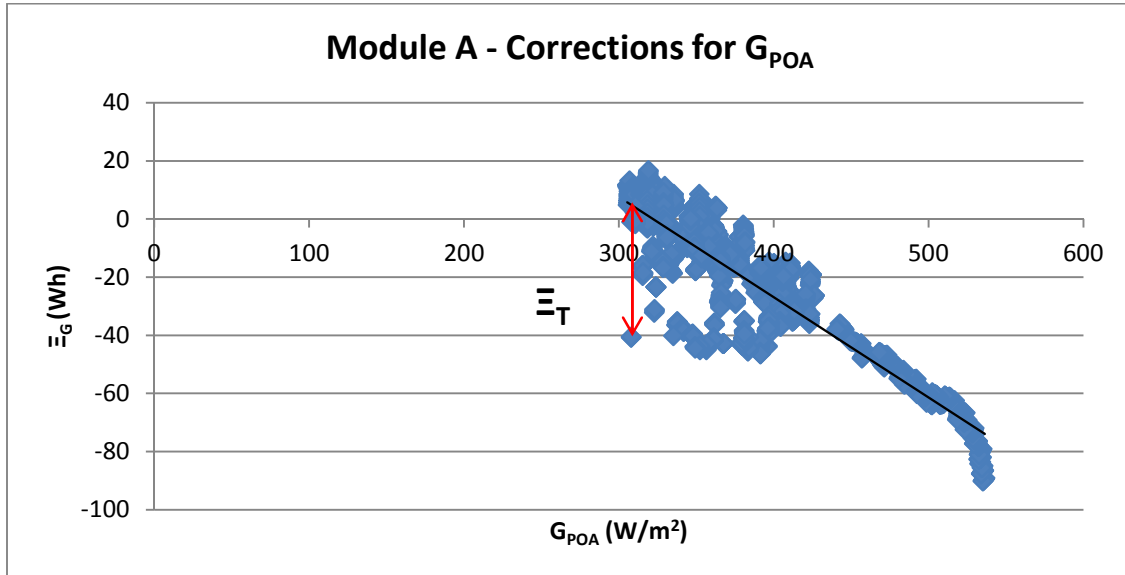
Figure 25 – Illustration of Ξ_T

Hourly production bar graphs follow in Figure 26 – Module A with LPC1, Figure 27 – Module B with LPC1, Figure 28 – Module C with LPC1. It is evident from the scales of the bar graphs that the EBM withLPC1 fits much more closely than the baseline EBM, but that there remains some additional noise, which could be removed.

Figure 26 – Module A with LPC1

Figure 27 – Module B with LPC1

69
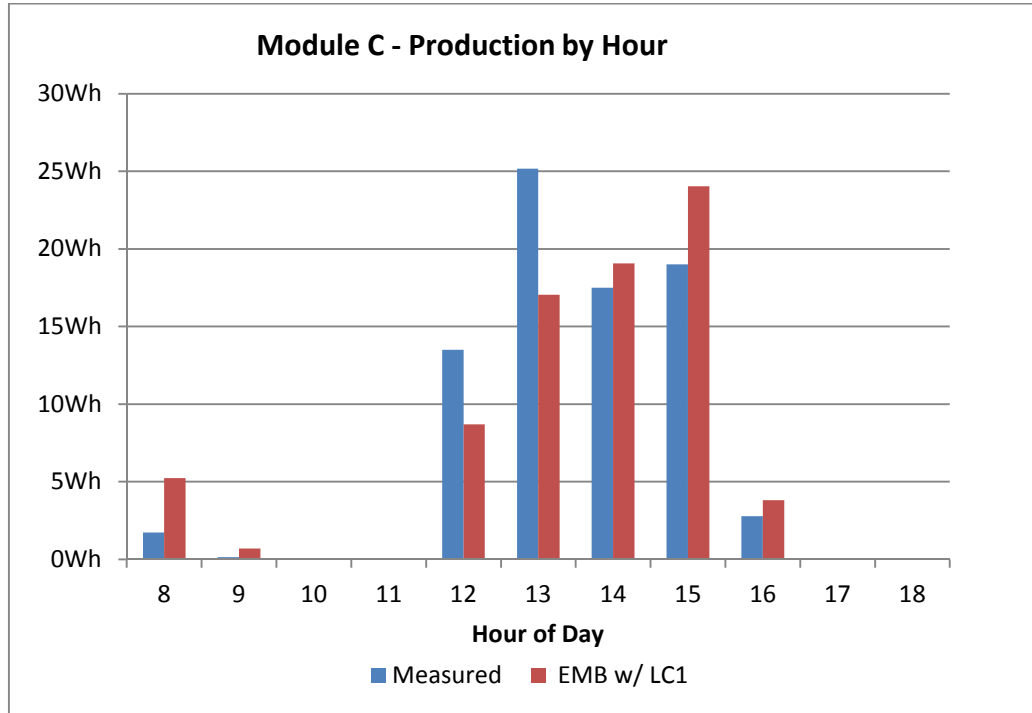
Figure 28 – Module C with LPC1

5.2.2 Linear Parameter Correction 2

In order to decrease the noise, the second parameter is introduced which then needs to have a data parameters selected for so that a linear fit can be calculated. This parameter Ξ_T is defined in 5-2.

Parameter selection must be repeated, so a new set of Pearson coefficients are calculated against Ξ_T as shown in Table 17.

Parameter	Module A	Module B	Module C
T_{Amb}	0.000	0.373	0.0925
T_{Cell}	0.344	0.364	0.654
EWT	0.308	0.354	0.658
LWT	0.349	0.348	0.728

Table 17 – Pearson Coefficients Against Ξ_T

Because the EWT and LWT values will not generally be directly known when

approaching a climatic model with no additional input, the slightly stronger Pearson coefficient for LWT as opposed to T_{Cell} is not judged to be sufficient to merit the application of LWT instead of the more easily calculated T_{Cell}. However the weak relation between T_{Amb} and Ξ_T on Modules A and C, incentivizes the use of T_{Cell} instead of T_{Amb}.

With this parameter pairing selected, the process undertaken for Ξ_G and G_{POA} is now repeated for Ξ_T and T_{Cell} with a resulting estimate, ξ_T:

$$\xi_T = T_{Cell} m_{T\xi} + b_{T\xi}$$

5-3

The values of the linear parameters are then contained in Table 18:

Module	Slope ($m_{T\xi}$)	Intercept ($b_{T\xi}$)
A	0.82	-265
B	0.93	-276
C	1.52	-487

Table 18 – Parameters for ξ_T

Plots for the parameters follow.
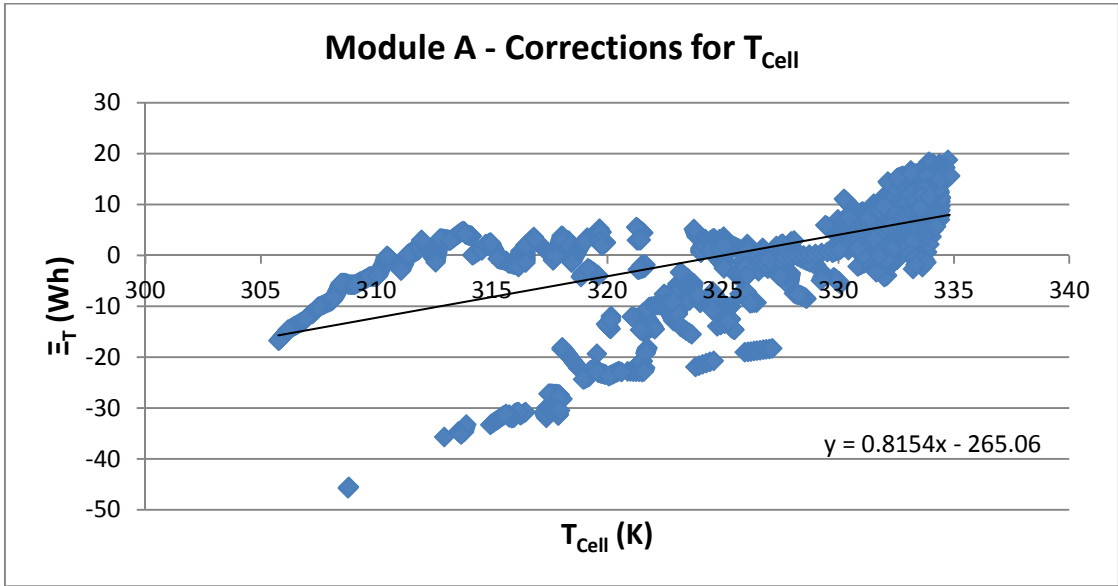
Figure 29 – Module A Parameters for T_{Cell}
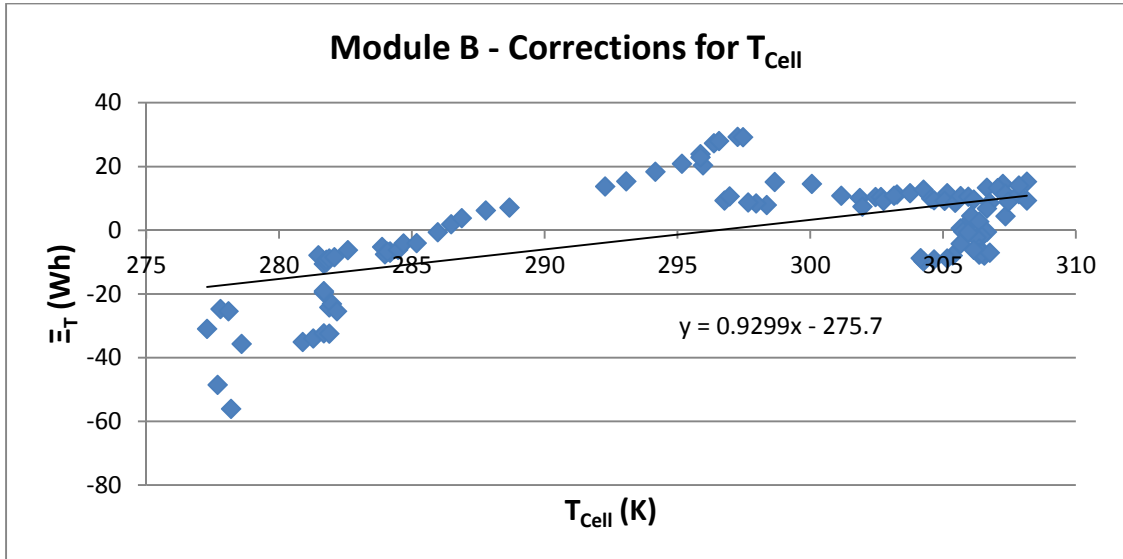
Figure 30 – Module B Parameters for T_{Cell}
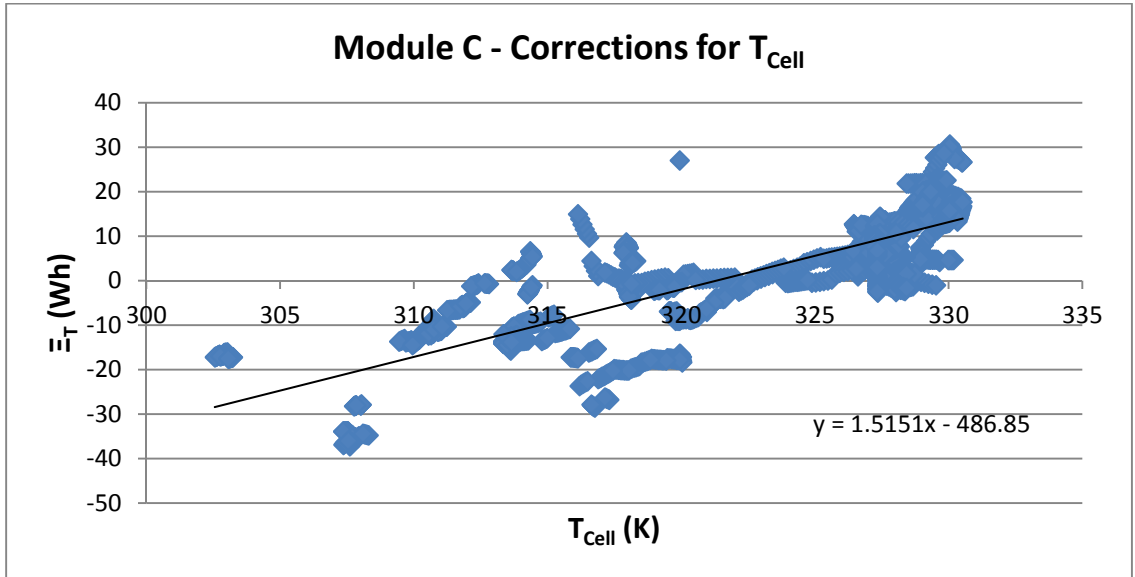
Figure 31 − Module C Corrections for T_Cell

It ~~will~~ was ~~be~~ observed that the Module A's plot is not completely linear in nature, but ~~it~~ instead shows a trend of higher error for lower TCell values under certain conditions. These conditions ~~are~~ were met best in the later part of the afternoon. Later corrections will take this into account. Presently, the Ξ_T correction is applied. This correction is hereafter called "Linear Parameter Correction 2" or "LPC2." Plots of the hourly production once the LPC2 were applied follow:
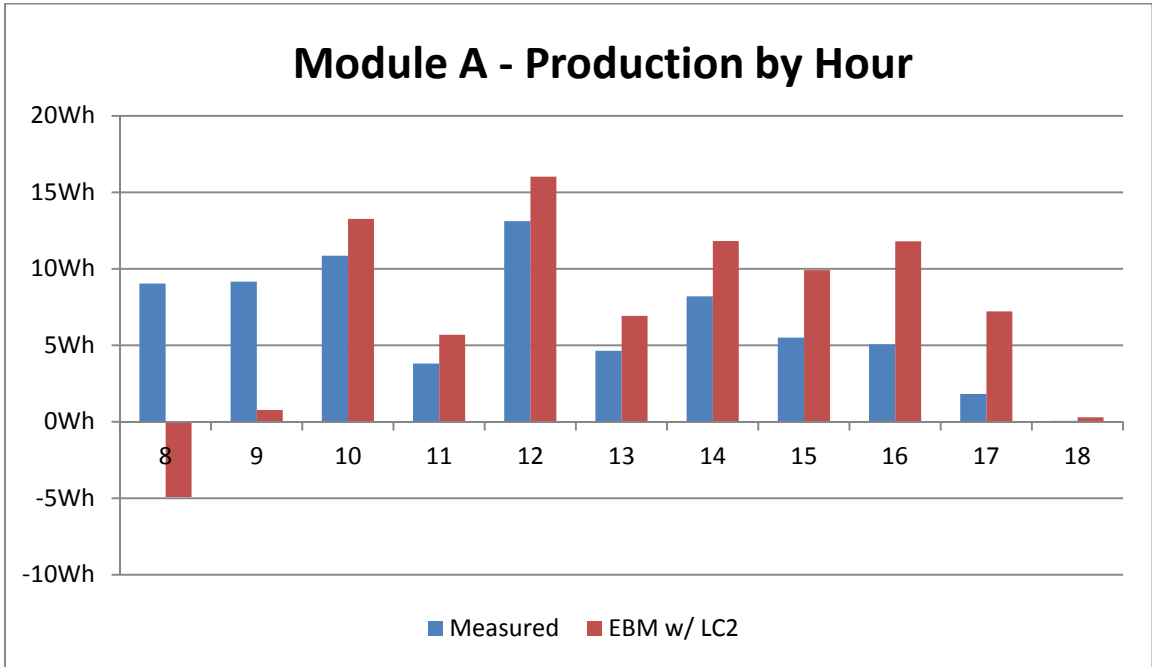
Figure 32 – Module A with LPC2
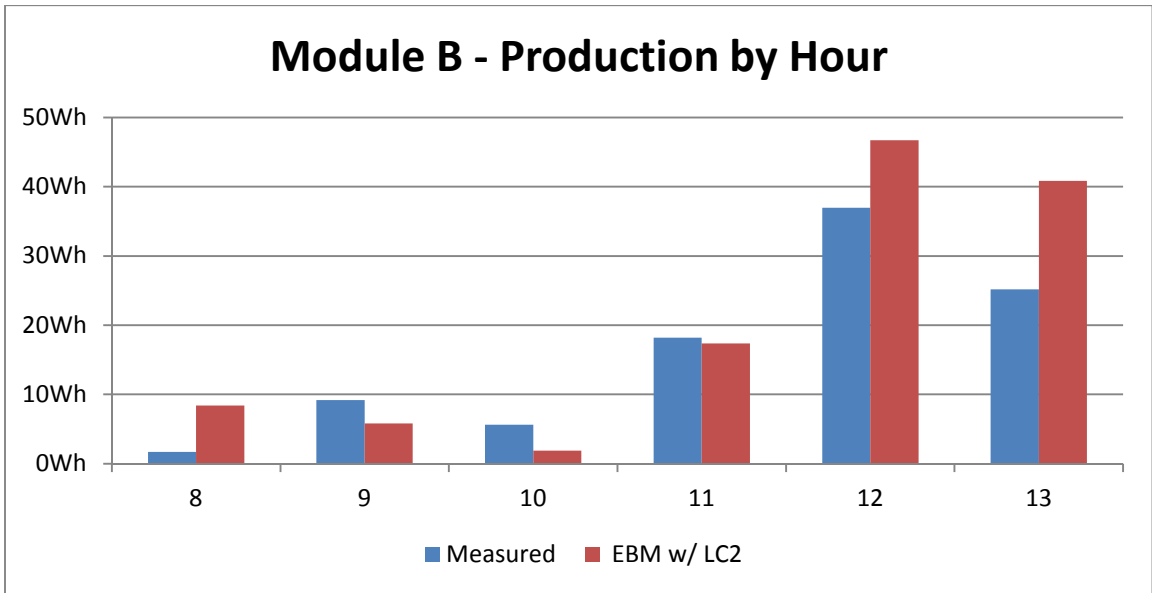
Figure 33 – Module B with LPC2

74
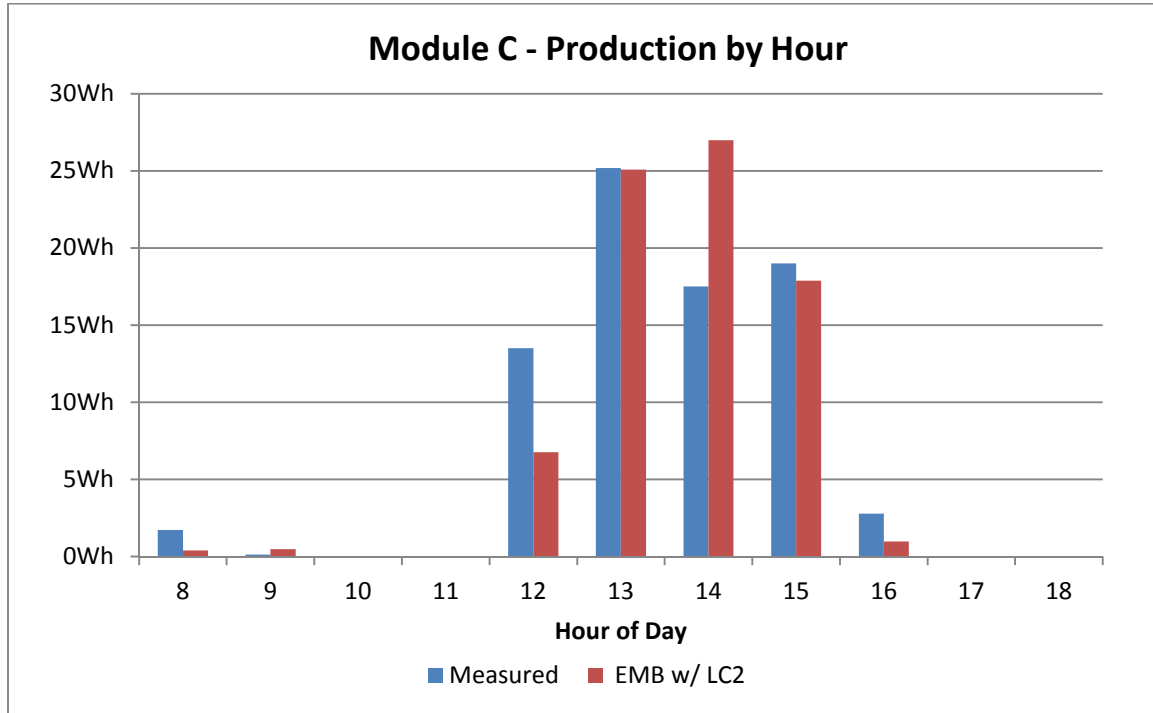
Figure 34 – Module C with LPC2

5.2.3 Time Parameter

As a final step, a third parameter Ξ_{TIME} is calculated and the same linear fitting process is undertaken. In this case, the times are decimal representations of the solar hours (e.g. solar noon is 12.00 and 13:45 is represented as 13.75.)[*] This parameter and its corresponding estimate ξ_{TIME} are calculated against t_{DECI} according to:

_____

[*] It is expected that this time parameter may need to be converted to a parameter based on the AOI for a completely accurate set of corrections, however the recording times do not follow a complete annual cycle and are thus precluded from confirming or refuting this. For sake of future work, the operation times of the modules during their recording is included in Appendix C - Module Operation Times.

$$\xi_{TIME} = t_{DECI} m_{Time\xi} + b_{Time\xi}$$

$$5\text{-}4$$

These parameters follow for each module in Table 19.

Module	Slope ($m_{Time\xi}$)	Intercept ($b_{Time\xi}$)
A	-3.50	42.3
B	-3.46	31.4
C	-1.07	15.4

Table 19 – Parameters for Ξ_{TIME}

This final correction sets the average error in the measurements to negligible amounts.

Plots of the hourly values of predictions against their measured counterparts follow in Figure 35, Figure 36 – Module B with Time Parameter, and Figure 37.
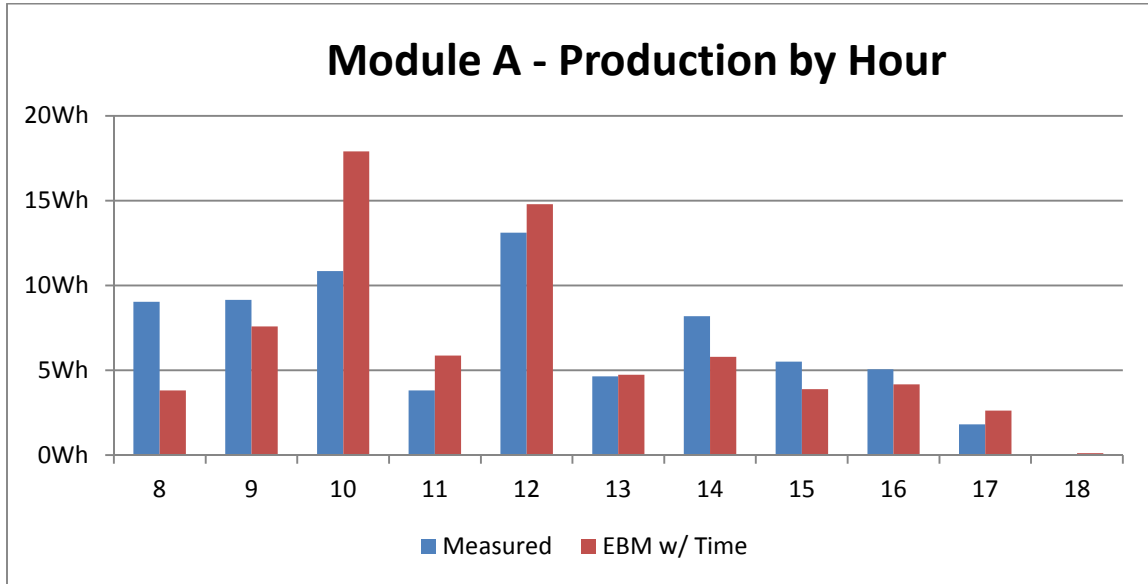
Figure 35 – Module A with Time Parameter
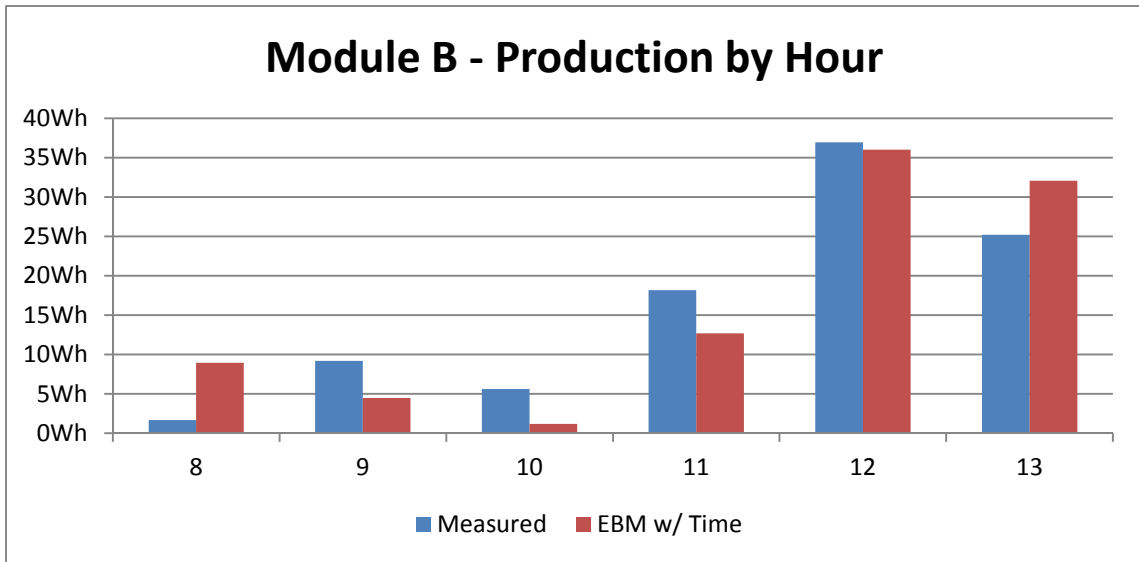
Figure 36 – Module B with Time Parameter
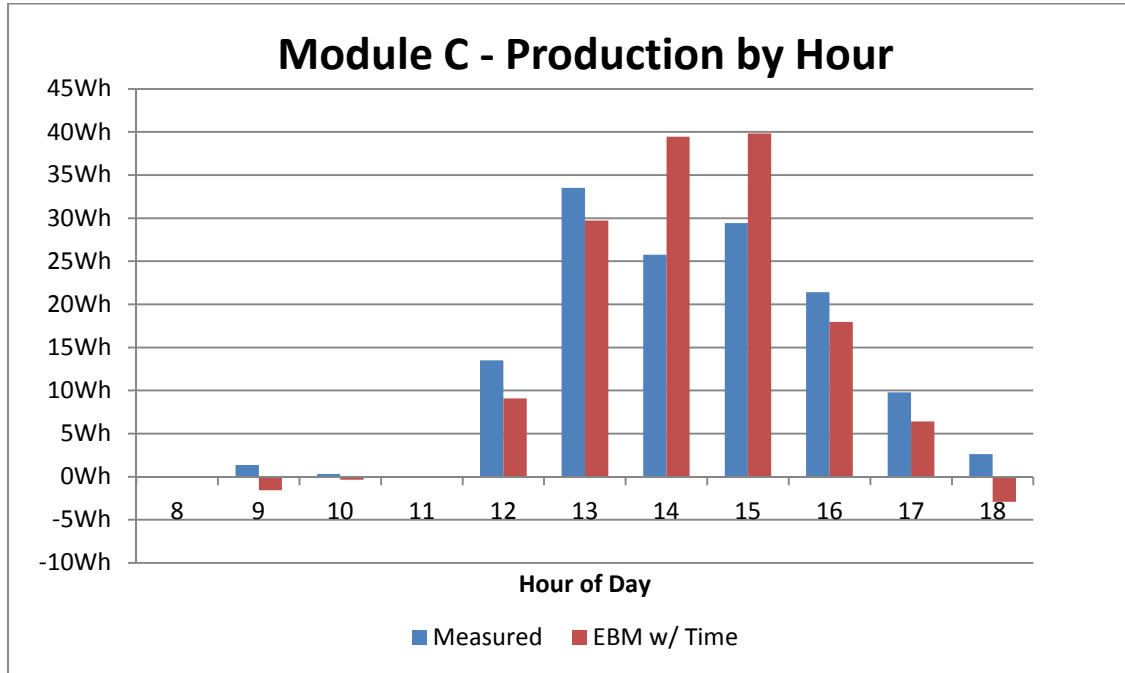
Figure 37 – Module C with Time Parameter

At this stage of the data fitting process, the evaluation of a fit becomes more difficult to accomplish by looking at the hourly production matches. In Table 20, Table 21, and Table 22 the correlation coefficients, standard deviations of the error, and the average of the error across the records for each of modules can be seen. The correlation clearly increases and the average error decreases for all modules as the corrections are applied.

Module A – Deviations of Prediction from Measurements				
	Baseline	LPC1	LPC2	Time
St. Dev:	13.21	13.7	11.9	6.87
Average:	-28.1	-2.31	-1.34	0.000
Max:	-2.68	26.4	22.5	11.5
Min:	-59.0	-33.6	-27.5	-19.4
Corr:	0.393	0.014	0.015	0.440

Table 20 – Parameterization Results for Module A

78

Module B – Deviations of Prediction from Measurements				
	Baseline	LPC1	LPC2	Time
St. Dev:	61.4	19.1	14.0	12.7
Average:	-28.2	-11.3	-7.17	0.000
Max:	45.5	18.8	20.3	24.1
Min:	-121.6	-57.6	-40.1	-43.9
Corr:	-0.866	0.658	0.821	0.740

Table 21 – Parameterization Results for Module B

Module C – Deviations of Prediction from Measurements				
	Baseline	LPC1	LPC2	Time
St. Dev:	7.65	7.46	9.25	9.08
Average:	-20.5	0.275	0.275	0.000
Max:	9.43	38.8	261	263
Min:	-41.4	-17.8	-18.7	-18.8
Corr:	0.290	0.169	0.566	0.590

Table 22 – Parameterization Results for Module C

5.3 Cumulative Error Reduction in EBM

For sake of understanding how the errors between the baseline, the LPC1, LPC2, and time corrected levels of the EBM reduce, histograms of the Ξ^* are shown in the next several figures.

---

* Ξ for any portion of the parameter application.
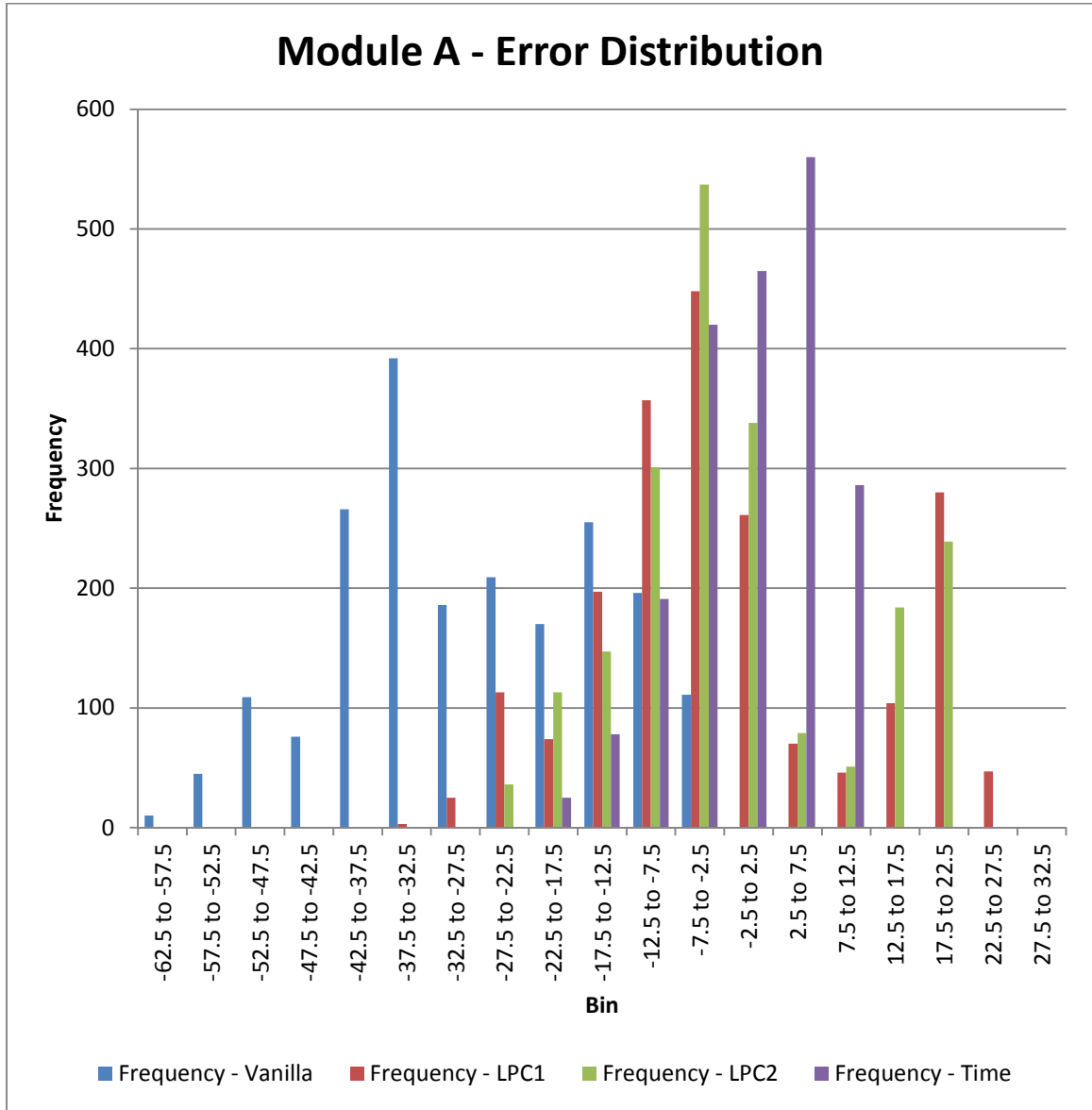
Figure 38 – Module A EBM Ξ Frequency

As can be seen in the histograms, the error decreases substantially on the application of LPC1, followed by slow compaction of the shape of the distribution through the next two corrections.
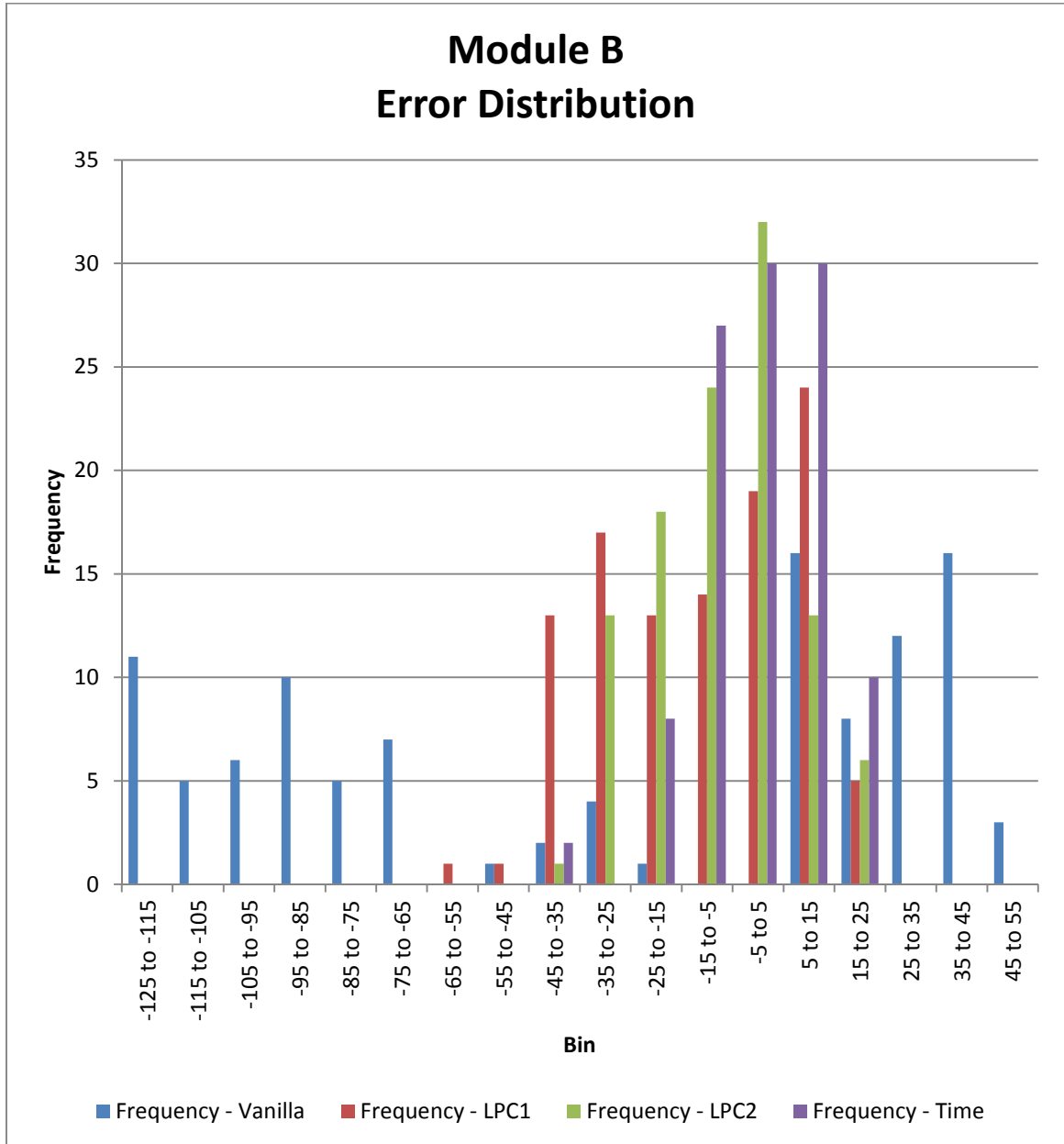
Figure 39 – Module B EBM Ξ Frequency

In Module B's histograms as in Module A's, the LPC1 corrects for initial errors in the calculation and subsequent corrections tighten the calculation.
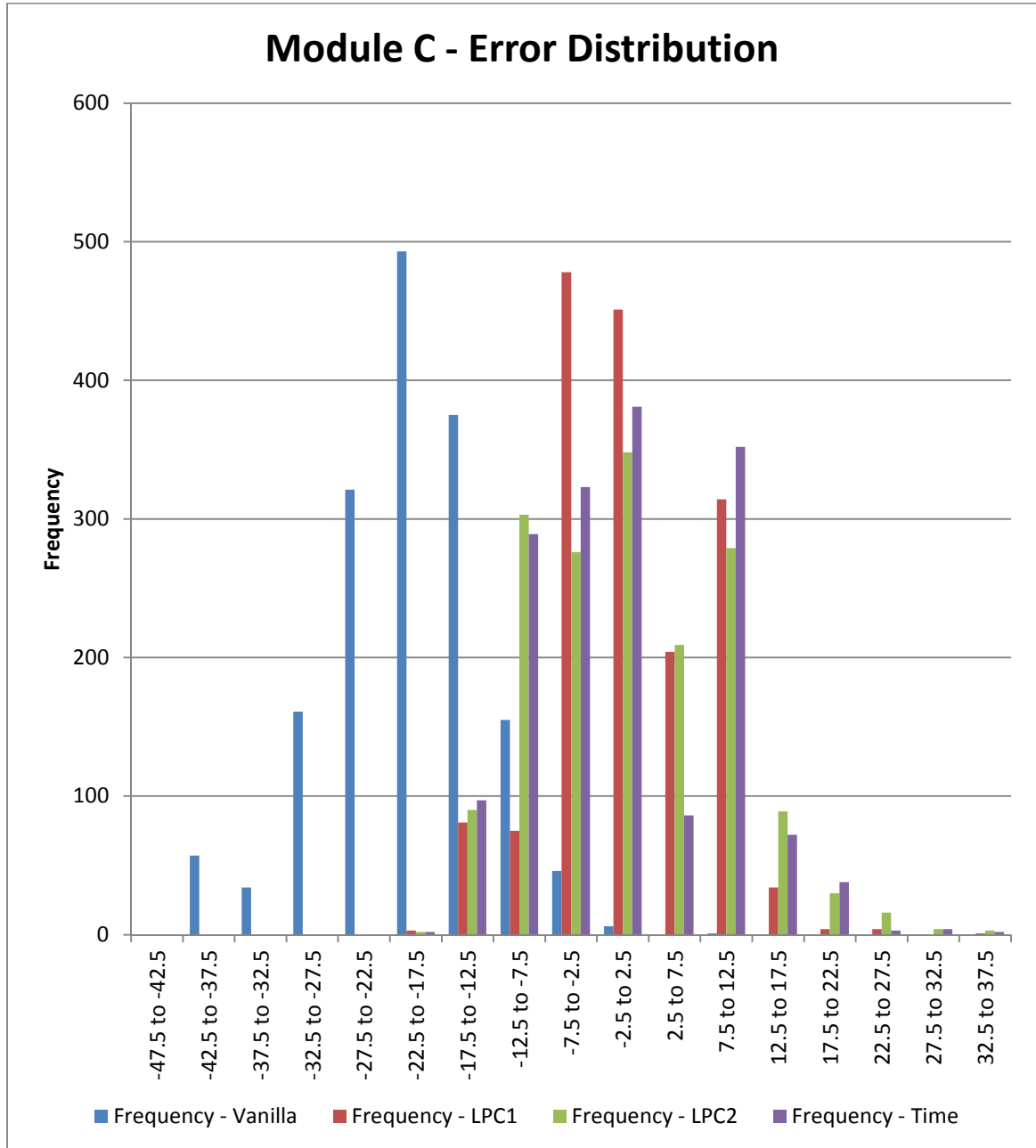
Figure 40 – Module C EBM Ξ Frequency

In Module C, as opposed to Module A and Module B, the data spread out further slightly as LPC2 and the Time Correction are applied to the EBM. However, the

correlation coefficients increase and the net error decreases as the corrections are applied.

A summary of the values is shown in Table 23 – Summary of Deviations between Measured and Calculated Values. As the Module A and C LPC1 and LPC2 are applied, the difference between measured and calculated values quickly drops to within the margin of error. As Module B has the final Time Adjustment applied, the difference drops within the margin of error as well.   For all three modules, the error is substantially reduced as the LPC's are applied. Given that the point counts between Module A and C and Module B are orders of magnitude different on account of the re-recording required for Module B, it is expected that longer measurements on Module B should result in lessened error in the calculation as the LPC1 and LPC2 are applied.

Mod	Modeled Results, "Baseline" Thermal Model	% Dev From Meas - urment	Tcell and GPOA parameter - ization: no time adjust	% Dev	With time adjust correctio n	% Dev	Data Pts
A	230Wh	-111% (+1% /-1%)	79Wh	11% (+12% / -10%)	71Wh	0% (+11% /-9%)	2025
B	197Wh	104% (+13% / -12%)	123Wh	26% (+8% / -7%)	97Wh	0% (+6% /-6%)	107
C	98Wh	23% (+8% / -7%)	79Wh	-2% (+7% / -6%)	80Wh	0% (+7% / -6%)	1649

Table 23 – Summary of Deviations between Measured and Calculated Values

Chapter 6: Water Temperatures and a Two Dimensional Finite Difference Method (FDM) Model

6.1 Discretization and FDM Description

As part of the process of understanding the collectors' thermal resistances, a finite difference model of the collectors was employed using the methods Zondag et al developed[66]. The collectors are discretized as shown in Figure 41.
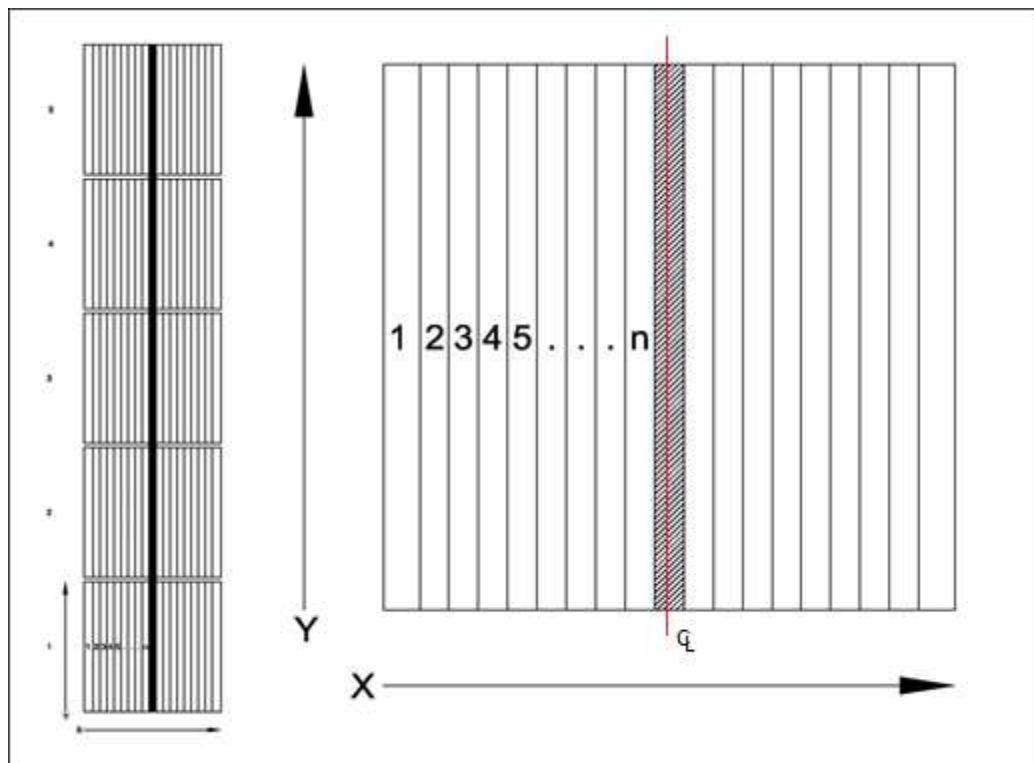
Figure 41 – Discretization of Collectors

The cells are considered individually in the *y*-direction and split into 25 sections such that $n = 25$. It is evident that across the centerline the temperature distributions are mirrored. For the Single Tube Collector A, this diagram explains exactly how the discrete elements are formed. For the Serpentine Collector A, these elements are extended such that their average length corresponds to the length of tubing available to the rear face of the cells on the collector, while their width is reduced so that the total area per strip remains constant. For the Double Tube Collector B, these sections have their width reduced so that each cell is split into two symmetrical sets of two mirrored elements (that is to say, each set of elements *n* represents a quarter of the total cell.)

After this discretization, an energy balance is applied to the cells, glass, and the collector plate:

$$q_{cell,glass}'' - q_{glass,rad}'' - q_{sky,conv}'' + k_{glass}\delta_{glass}\frac{\partial^2 T_{glass}}{\partial x^2} = 0$$

6-1 – Energy Balance of the Glass

$$(\tau - \tau_\alpha \eta_{el})G_{POA} - q_{sky,rad}'' - q_{cell,glass}'' - q_{cell,plate}'' + k_{Si}\delta_{cell}\frac{\partial^2 T_{cell}}{\partial x^2} = 0$$

6-2 – Energy Balance of the Solar Cell

$$q_{cell,plate}'' - q_{back,conv}'' + \delta_{plate}k_{Aluminum}\frac{\partial^2 T_{Aluminum}}{\partial x^2} = 0$$

6-3 – Energy Balance of the Aluminum Plate at Rear of Solar Collector

For the final cell in the x-direction on the plate, 6-3 has a negative $(T_{abs} -$

$EWT_{Cell})k_{H2O}\pi\frac{Nu}{D}$ added to it, where Nu = 3.66 for laminar flow. Furthermore, at this final cell, symmetry dictates the second derivatives with respect to x must be zero.

For the purposes of the FDM, the following are the definitions of the above terms:

$$q''_{cell,glass} = k_{EVA}/\delta_{EVA}(T_{cell} - T_{glass})$$

6-4

$$q''_{glass,rad} = F_{Sky}\sigma\epsilon_{glass}(T^4_{glass} - T^4_{sky})$$

6-5

$$q''_{sky,conv} = (2.8 + 3 * WS)\frac{k_{Air}}{L_c}(T_{glass} - T_{Amb})$$

6-6

$$q''_{glass,rad} = F_{Sky}\sigma\epsilon_{p-Si}(T^4_{cell} - T^4_{sky})$$

6-7

$$q''_{cell,plate} = \frac{k_{Kapton}}{\delta_{Kapton}}(T_{cell} - T_{plate})$$

6-8

$$q''_{back,conv} = \frac{1.13(RePr)^{\frac{1}{2}}}{k_{Air}L_c}(T_{Plate} - T_{Amb})$$

6-9

6.2 FDM Model Results

6.2.1 First Cell Temperature Variations

By using these equations and discretizing the cells as outlined above, a finite difference model can be developed that converges quickly. These models were run for each of the three collectors with an assumed wind speed of 1.5m/s, EWT for the collector held at 10°C, a T_{Amb} of 25°C, mass flow of 0.8g/s, and G_{POA} values varying between 1,000W/m^2 and 200W/m^2.

A plot of the temperatures for each of the lateral conductions is shown below at 800W/m^2 for the first cell to see the water for cooling.
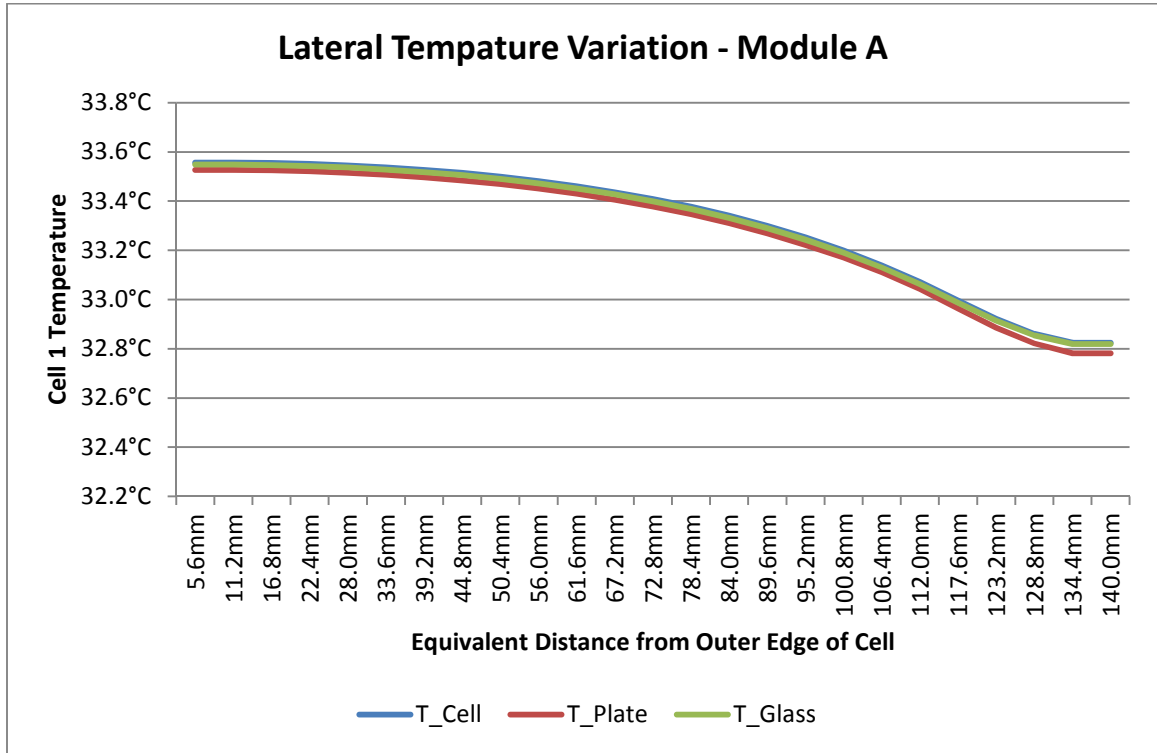
Figure 42 – Lateral Temperature Variation in Cell 1 of Module B at 800W/m²
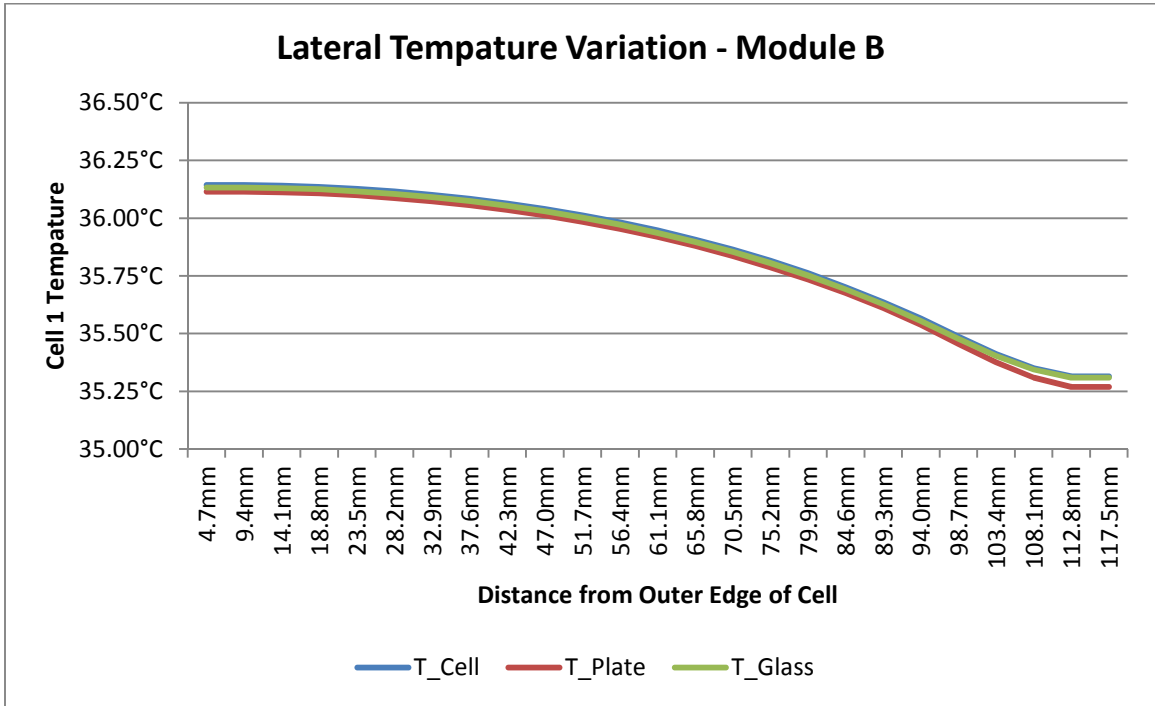
Figure 43 – Lateral Temperature Variation in Cell 1 of Module B at 800W/m²
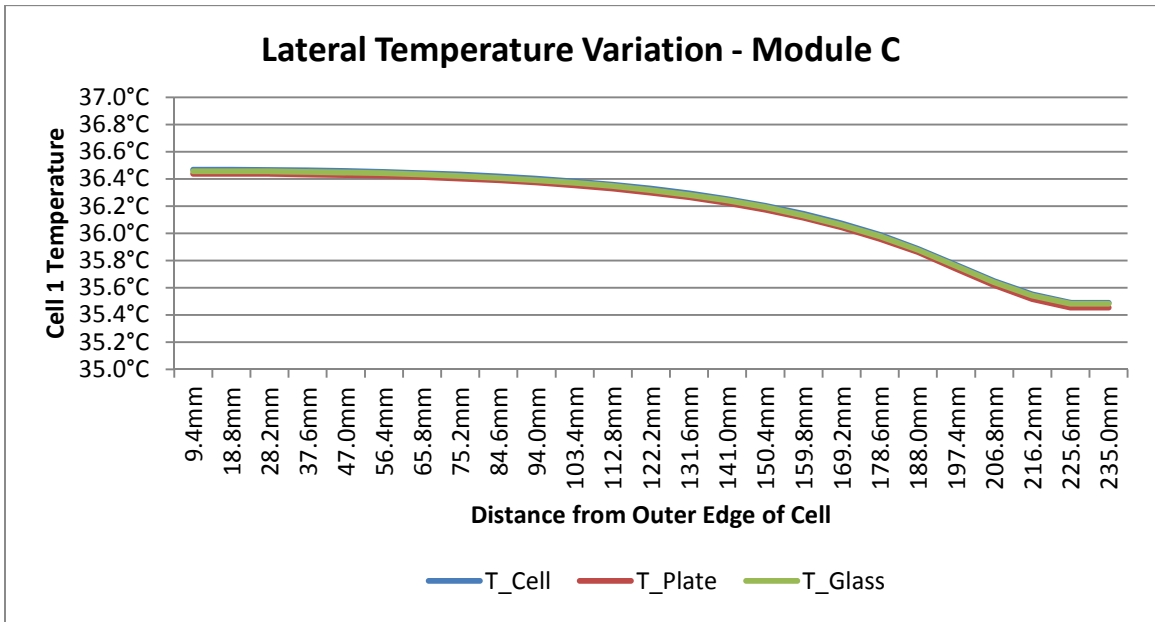
Figure 44 – Lateral Temperature Variation in Cell 1 of Module C at 800W/m²

6.2.2 FDM Results Discussion

In general, the models show that the modules experience a relatively close temperature swing from the outer edge of the cells to the tube between the layers. The largest temperature differences between the layers are seen in the $1,000W/m^2$ calculations. These differences are shown in Table 24 – Max FDM Differences.

Module	Max Difference
A – Serpentine	0.045°C
B – Double	0.048°C
C - Single	0.028°C

Table 24 – Max FDM Differences

Based on these relatively small differences between the layers for any given lateral section, it's reasonable to focus on the cell temperatures for qualitative analysis. Each module's respective cell temperatures are shown below for the $800W/m^2$ case. Full results for the water temperature and cell temperatures for 200, 400, 600, 800, and $1000W/m^2$ are tabulated in the appendices.
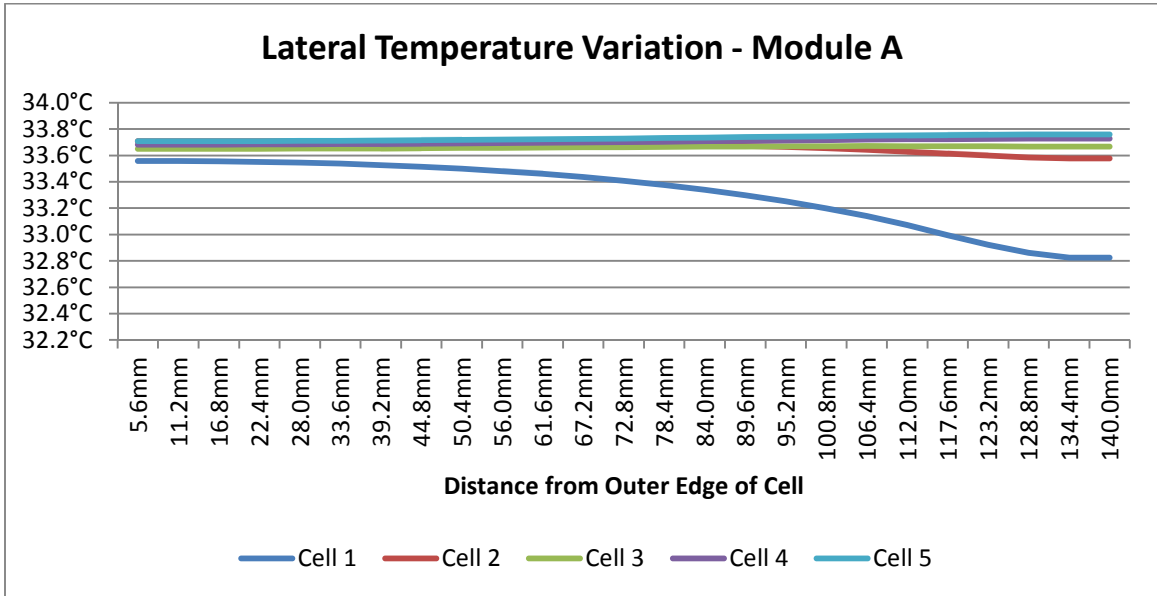
Figure 45 – Lateral Temperature Variation of Cell Temperature in Module A at 800W/m²
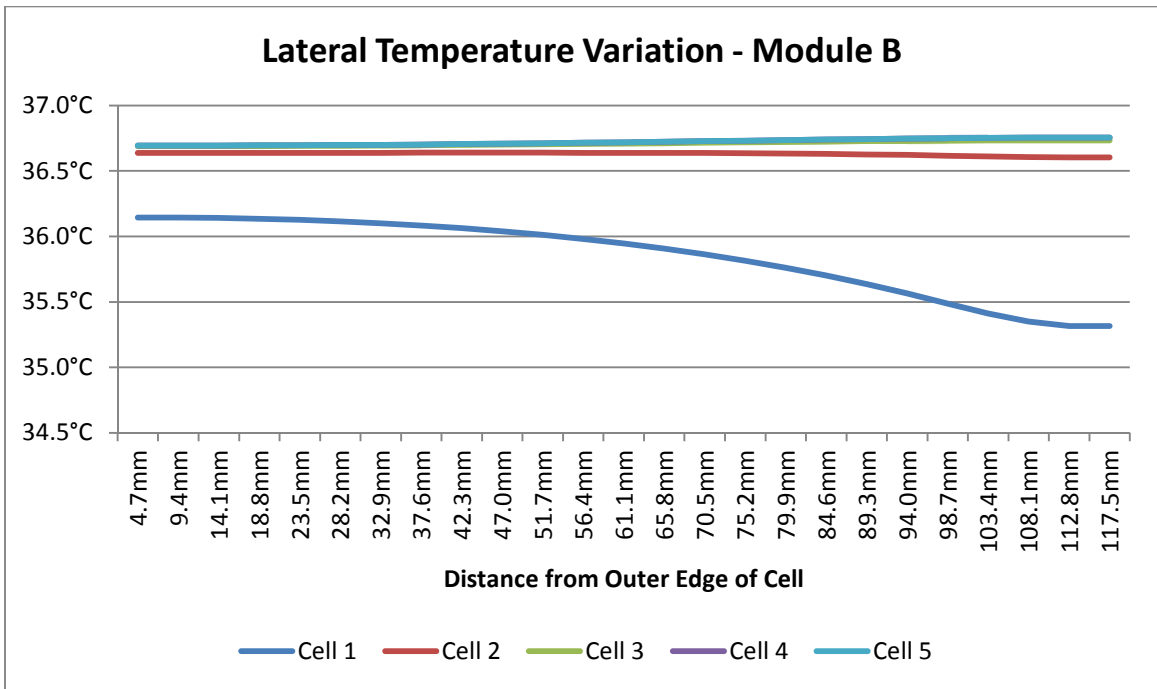
Figure 46 – Lateral Temperature Variation of Cell Temperature in Module B at 800W/m²
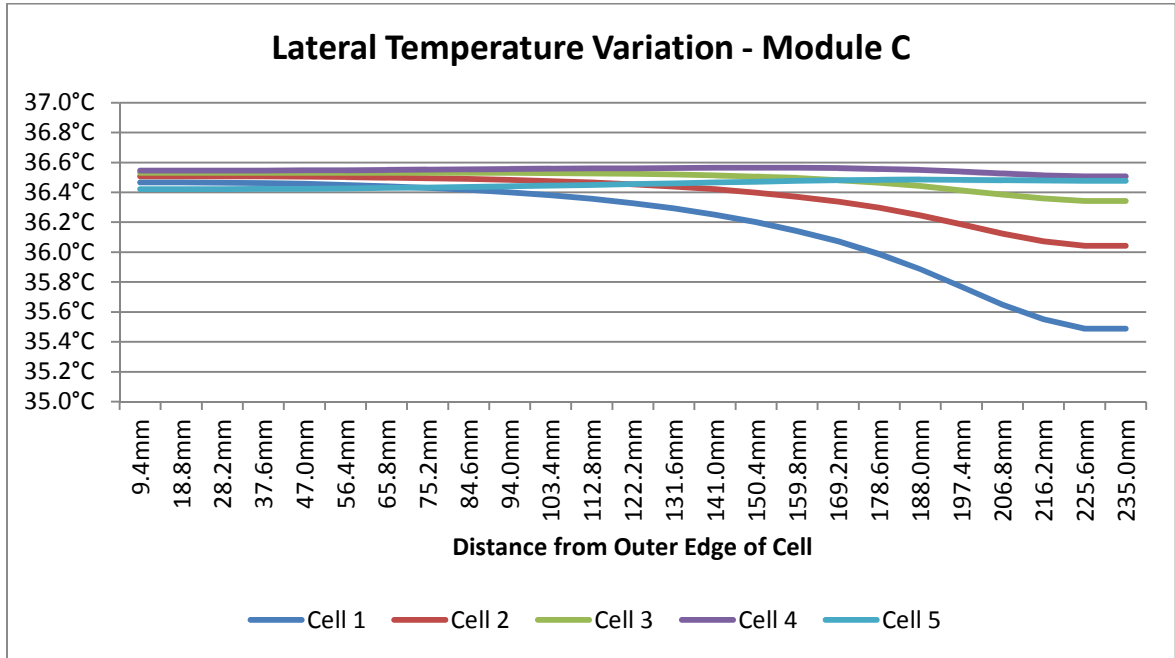
Figure 47 – Lateral Temperature Variation of Cell Temperature in Module C at 800W/m²

Generally, we can see that as the cells proceed towards the rear of the collector, the temperature swing from the edge to the copper tubing is reduced. This is because the cooling water heats up and accepts less of the heat from the collector, as can be seen below in Table 25.

Module	Cell	Water Temp
A	1	10.0°C
	2	28.2°C
	3	32.5°C
	4	33.4°C
	5	33.6°C
B	1	10.0°C
	2	34.0°C
	3	36.4°C
	4	36.7°C
	5	36.7°C
C	1	10.0°C

Module	Cell	Water Temp
	2	22.1°C
	3	28.7°C
	4	32.3°C
	5	34.3°C

Table 25 – Water Temperatures

It should be noted that Module B shows a substantially greater temperature gain. Further observation shows that, for these irradiance conditions, the Serpentine and Single Tube collectors have about the same thermal results. This result is not consistent and at low irradiances or high irradiances, the model shows a stronger heat recovery from the Sserpentine collector. The signal is also not especially strong and the mid-level irradiance difference may be a result of modeling error.

The bulk of the difference however, stems from the fact that the serpentine collector (Module A) reaches equilibrium faster and that the collectors are long enough to allow the single tube collector (Module C) to catch up. Meanwhile, Module B rapidly outruns either of the other two.
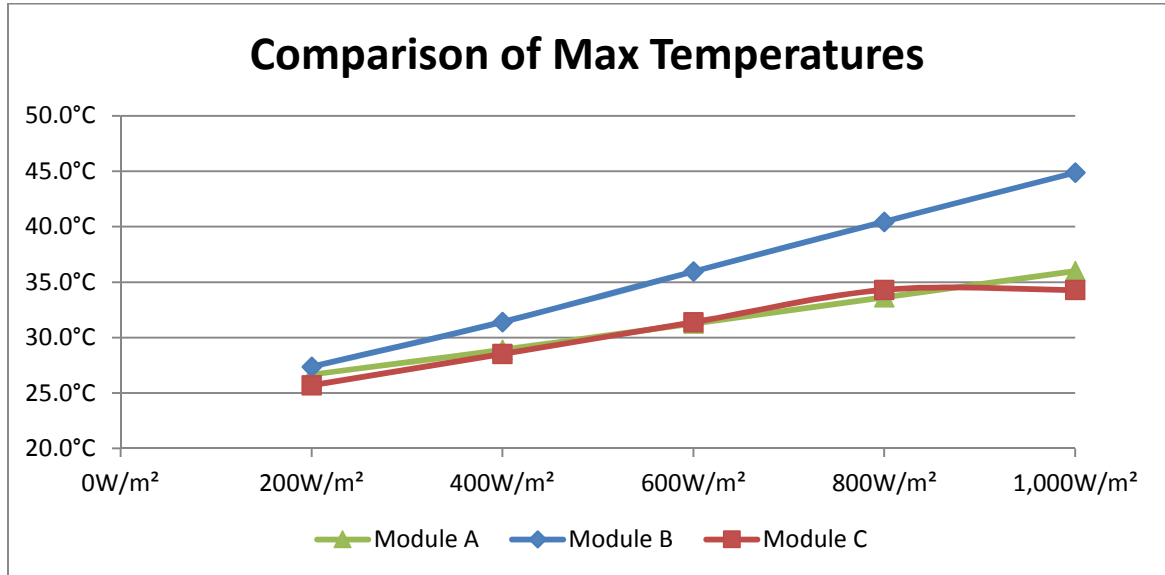
Figure 48 – Comparison of Cell 5 Water Temperatures

6.2.3 Immediate Conclusions from FDM

There are three significant takeaways from this temperature comparison. First, Module A and B's tubing arrangement may be efficient enough to justify not routing the tubing in long series down the absorber, but rather collecting all the individual cells back into a common manifold.

Second, Module A and B show a decidedly faster isothermal response, reducing the dT/dx quickly. This is important because of the thermal stresses associated with the difference in temperature laterally and the relative weakness of the micrometer thick poly-crystalline silicon that makes up the PV cells.

Third, Module B performs best of the three module designs. It has the highest surface contact and the lowest fin aspect ratio, both of which allow the water to cool the cells faster than the other designs.

Chapter 7: Thermal Efficiency of Collectors

7.1 Definitions

Thermal efficiency of a thermal collector is calculated by:

$$\eta_{TH} = \frac{Q_{Harvest}}{Q_{POA}} = \frac{c_p \dot{m}(LWT - EWT)}{G_{POA} A_{col}}$$

7-1

This efficiency is constrained by both the mass flow rate, plane of array irradiance and the leaving water temperature. The multiplicity of these variables means that for a given set of climatic conditions, there is no set thermal efficiency. This effectively prevents a closed form solution of the optimal mass flow for a given irradiance, which comes into play when the organic Rankin cycle is applied to analyze the data in Electrical Generation Model from the Heat Recovered from Collectors.

The thermal efficiencies of the PVT collectors were calculated, with a maximum observed efficiency of 54%. Plots of the efficiency can be seen in Figure 49, Figure 50, Figure 51, Figure 52, Figure 53, and Figure 54. This work approaches these efficiencies as being linearly dependent upon the temperature difference LWT – EWT as this is clearly supported by the data.

It should be understood that the efficiency can be driven to some limit by

pumping as much water as possible through the PVT heat exchanger as the calculation has no accounting for the pumping losses.[*] To remedy this, pressure drops must be modeled.

7.2 Pressure Drops in Collectors

Pressure drops relative to the mass flow in the collector were measured with a manometer and the means outlined herein for mass flow rate calculation. The mass flow shows the expected quadratic relationship to the pressure drop, according to:

$$\Delta P_{Pump} = \frac{1}{2} f_{collector} \rho_{H_2O} v^2$$

7-2

which for a given collector, with an incompressible fluid remaining approximately at the same temperature, reduces to:

$$\Delta P_{Pump} = C_{Pressure} \rho_{H_2O} v^2$$

7-3

The dimensionless pressure loss constants ($C_{Pressure}$) resulting from tests conducted, along with the maximum flow rate attained during the tests, shows below:

---

[*] The limit will establish itself as the energy losses from the collector via radiation and electrical generation become the only components of loss in the EBM which are relevant. In order for this to happen, the temperature differentials between the cells and all of their surroundings must be negligible as the HTF has effectively cooled the cell to ambient conditions.

Module	Pressure Loss Constant	Max Flow Rate (g/s)
A – Serpentine	9.00×10^{10}	0.27 ($\pm$ 0.01g/s)
B – Double Tube	6.98×10^{9}	1.38 ($\pm$ 0.01g/s)
C – Single Tube	6.02×10^{10}	0.37 ($\pm$ 0.01g/s)

Table 26 – Pressure Loss Constants

Based on these data, the pressure drop is modeled and the losses associated from the

pump incorporated into the efficiency calculation:

$$q_{Harvest}\eta_{ORC}\eta_{GEN} - q_{Pump}\left(\frac{1}{\eta_{Pump}}\right) = q_{Net}$$

7-4

Where $q_{Harvest}$ and q_{Pump} can be defined as:

$$q_{Harvest} = Min\left[Area * G_{POA}\eta_{Th,Max}, \dot{m}c_p(LWT - EWT)\right]$$

7-5

$$q_{Pump} = \Delta P_{Pump}\frac{\dot{m}}{\rho}$$

7-6

$\eta_{Th,Max}$ is considered to be 60% since the maximum observed value was 54%. As

mentioned previously, this is in accord with values achieved in the literature[67]

7.3 Thermal Efficiencies vs Temperatures
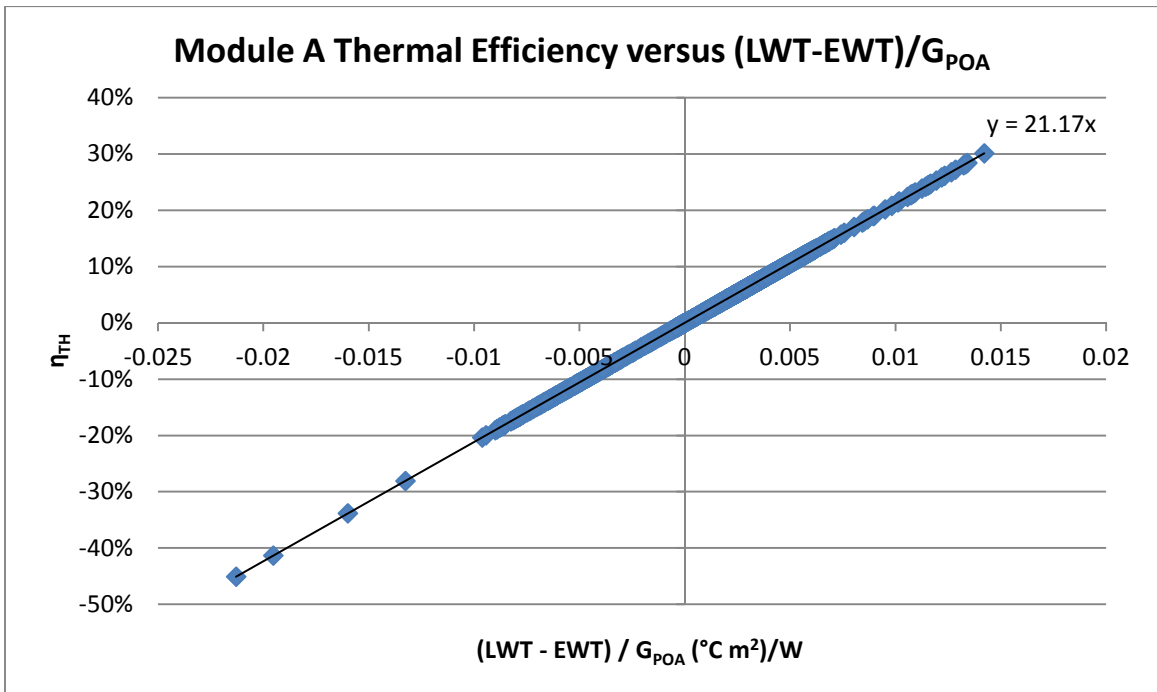
Figure 49 – Module A Thermal Efficiency vs. (LWT-EWT)/G$_{POA}$
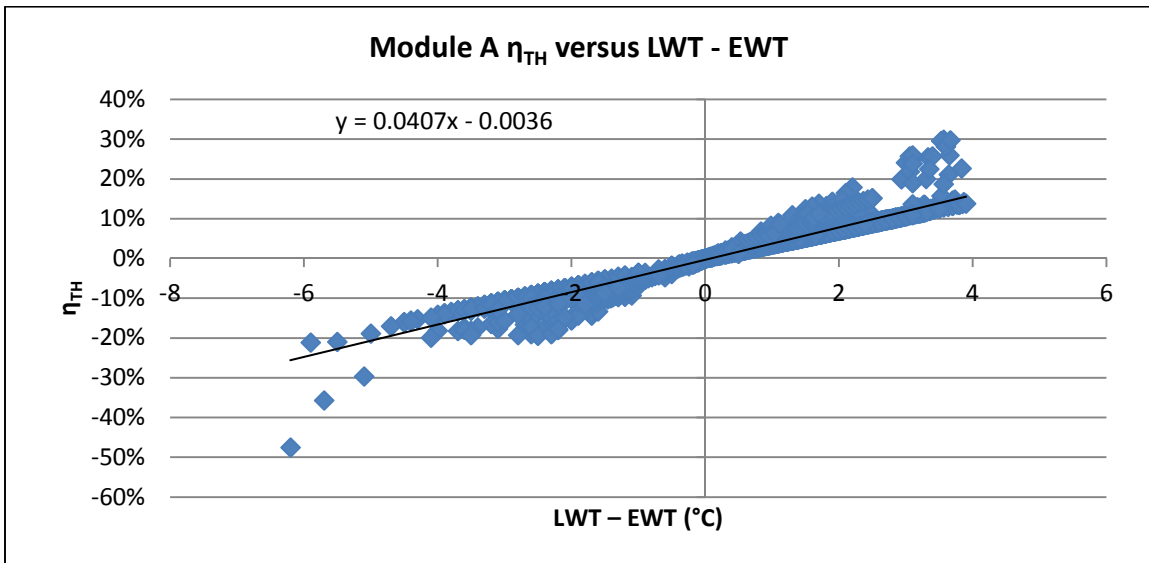
Figure 50 – Module A Thermal Efficiency vs. LWT-EWT
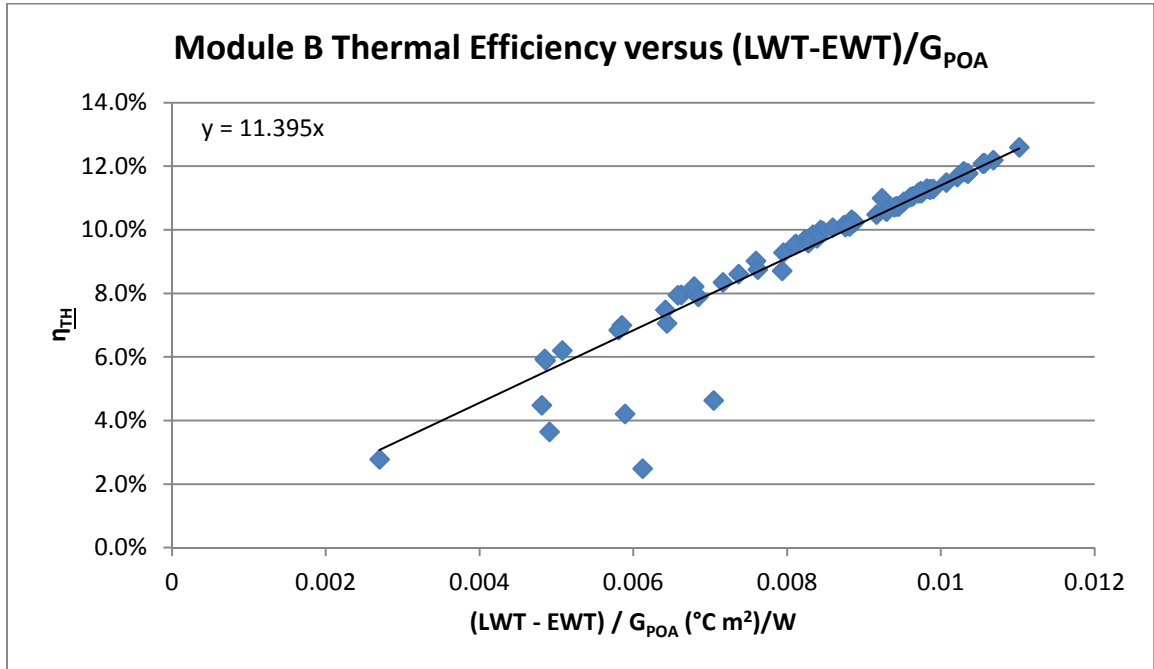
Figure 51 – Module B Thermal Efficiency vs. (LWT-EWT)/G$_{POA}$
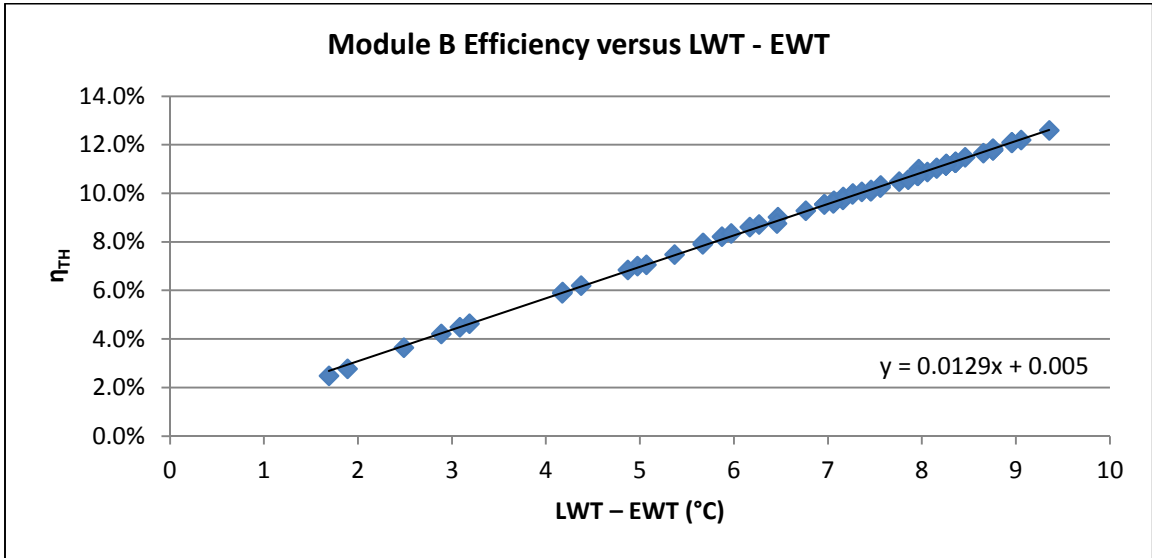
Figure 52 – Module B Thermal Efficiency vs. LWT-EWT
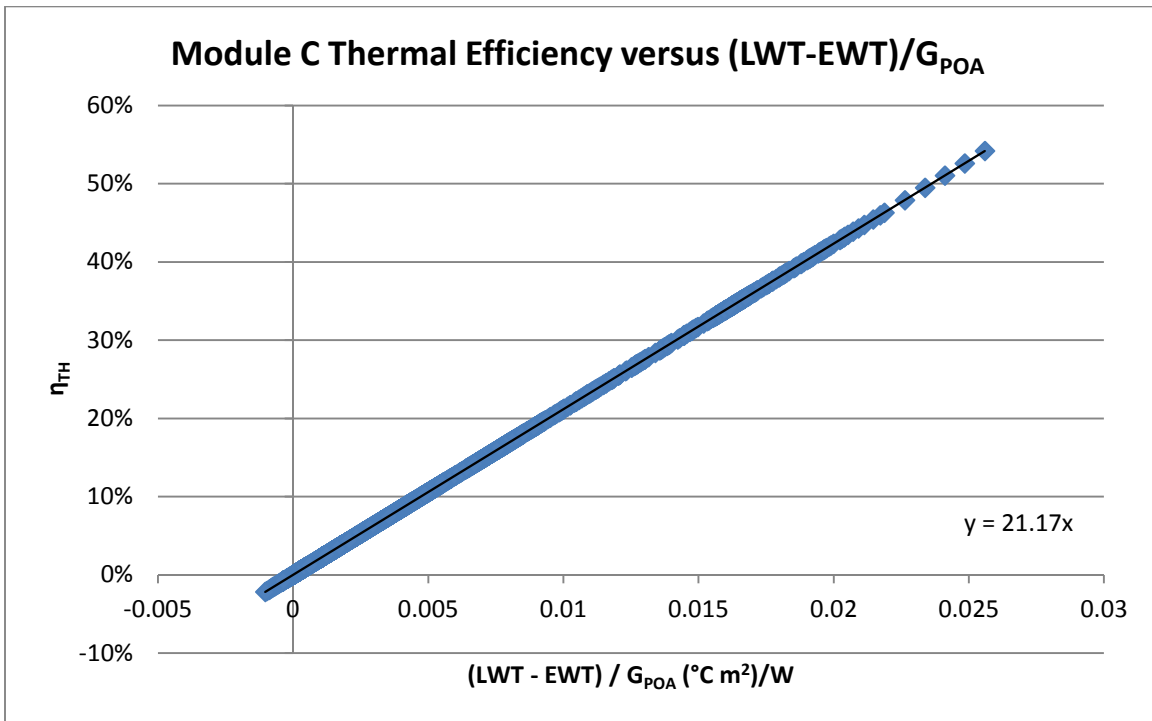
Figure 53 – Module C Thermal Efficiency vs. (LWT-EWT)/G$_{POA}$
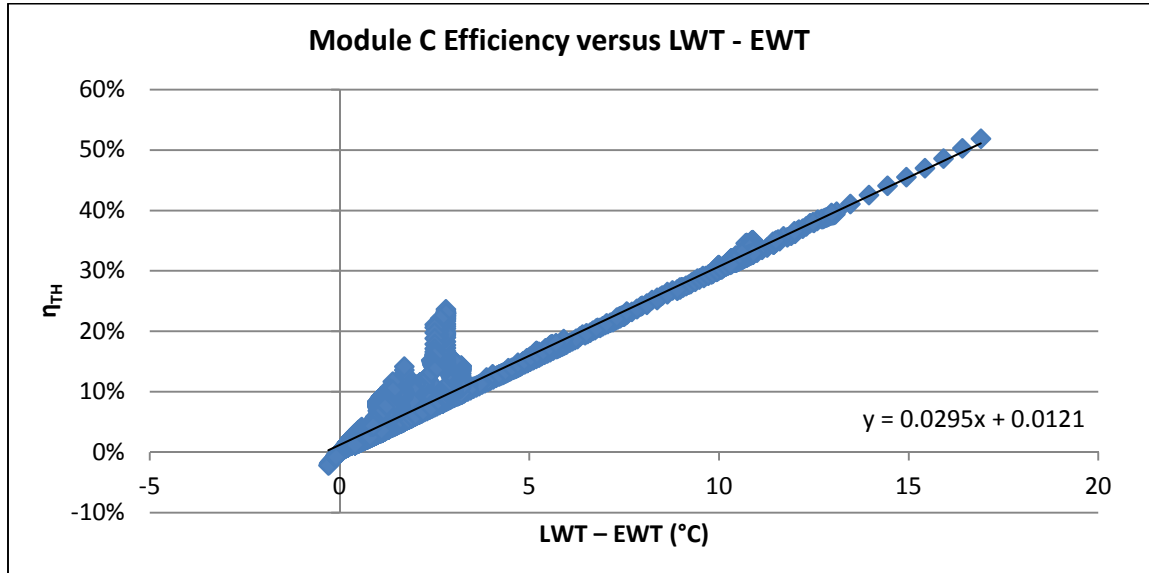
Figure 54 – Module C Thermal Efficiency vs. LWT-EWT

7.4 Mass Flow Optimization with Thermal Efficiency

These equations coupled with the information in Appendix B - Modeling T_{Cell} from Available Climatic Data produce the capacity to find a locally optimal mass flow rate for a given G_{POA} and $T_{Amb} - EWT$.[*] Examples of this follow for G_{POA} values of 800W/m^2 at different ΔT's with a maximum mass flow rate of 5.0 g/s, [m^2 of module]. The internal diameter of the tubing was 1.6mm" and the properties of the HTF (water) were maintained at 25°C and 1atm and tubing lengths are recorded in Table 7 – Tubing

---

[*] T_{Amb} - EWT is used as an approximation for the difference between T_{Amb} and the WB. In the ORC application envisioned in this work, the cooling available to the loop for rejection of waste heat will be provided by a cooling tower so that the EWT and the WB will, while not correlating exactly, be closely related.

Lengths by Collector. Given these parameters, the plots in Figure 56, Figure 57, and Figure 58 can be created. These plots show maximums in the region of 2.0g/s, [m^2 of module] to 3.5g/s, [m^2 of module] depending on the geometry and ΔT's involved.

7.4.1 Simplifying Assumptions

For the purposes of these plots, the product $\eta_{ORC}*\eta_{GEN}$ is assumed to be 10%. As will be seen Electrical Generation Model from the Heat Recovered from Collectors, this is not unreasonably high for summer conditions. η_{Pump} is assumed to be 80% which is achievable for centrifugal pumps under the correct conditions[68]. This is a simplifying assumption as η_{Pump} will in fact vary as $\dot{m}_{H_2O}$ requirements (and with them pressure losses) change.

7.4.2 Discussion of Mass Flow vs. Thermal Efficiency Results

Examining the figures, one notices several items:

1. Peaks appear in each of the projections of recovered electricity as the mass flow increases. The severity of the peak varies by module:

   a. Module A shows a very steep peak followed by a drastic drop.

   b. Module C shows a decidedly less steep drop (largely due to the lessened tubing length.)

   c. Module B shows the least steep drop. In all cases it is observable that the mass flow peaks increase as the ΔT increases, but harvested energy

decreases at the same time.

This peak is due to the limit imposed of 60% on η_{TH}. Once increasing the mass flow can no longer increase η_{TH}, the harvest of electricity shows a bend as additional mass pressed into the collectors produces only pressure losses. This peak may not be quite as sudden in practice, but it is expected to exist in approximately the same area. The pumping power required for Module A is about thirteen times higher than for Module B and about 50% higher than C owing to its substantive tubing length (see Figure 55.) This additional pumping power creates problems applying a Module A design as opposed to a Module B or C design in a PVT driven ORC.

2. As the parameter $T_{Amb} - EWT$ increases, the required mass flow to reach the limit decreases. This is a result of the fact that the HTF will receive all available energy with progressively lower mass flows as the HTF is further cooled before it enters the PVT heat exchanger This has the effect of encouraging installations in drier climates where the WB and T_{Amb} are typically separated by larger ΔT's than in the wetter areas.

3. Finally, the double tube collector's knee is the shallowest of the three collectors. This indicates that it would likely be the easiest to maintain in a near-optimal state with a mass flow controller. It is evident from these figures that in order for a PVT driven ORC to reach its full potential (or perhaps even work) the collectors need to have a mass flow controller as

part of their HTF loop.
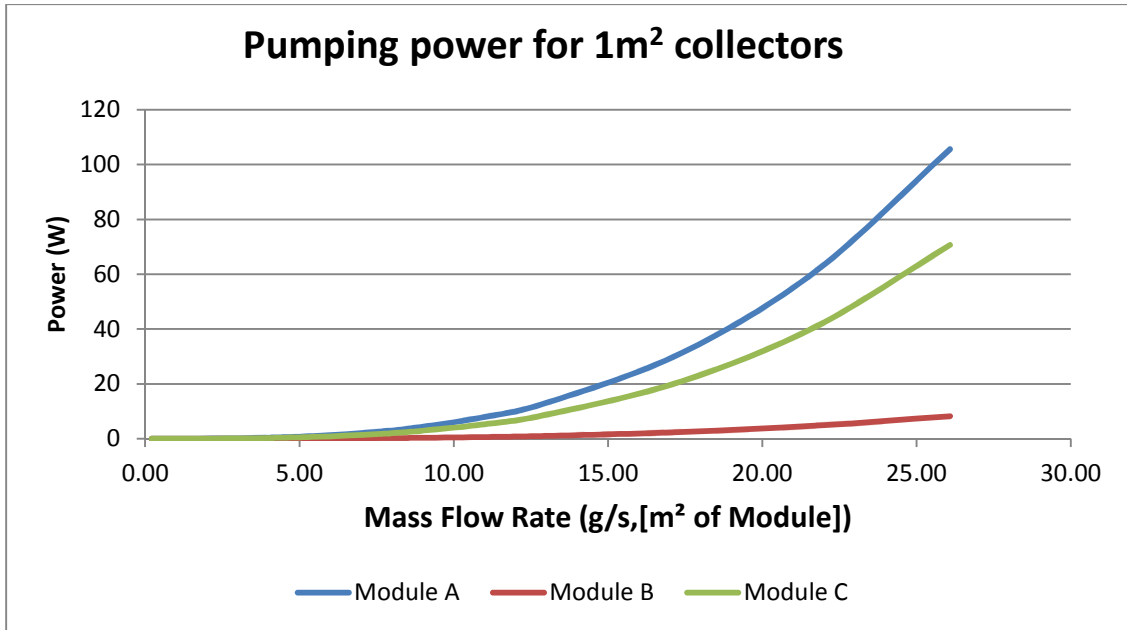
Figure 55 – Calculated Pumping Losses for All Modules
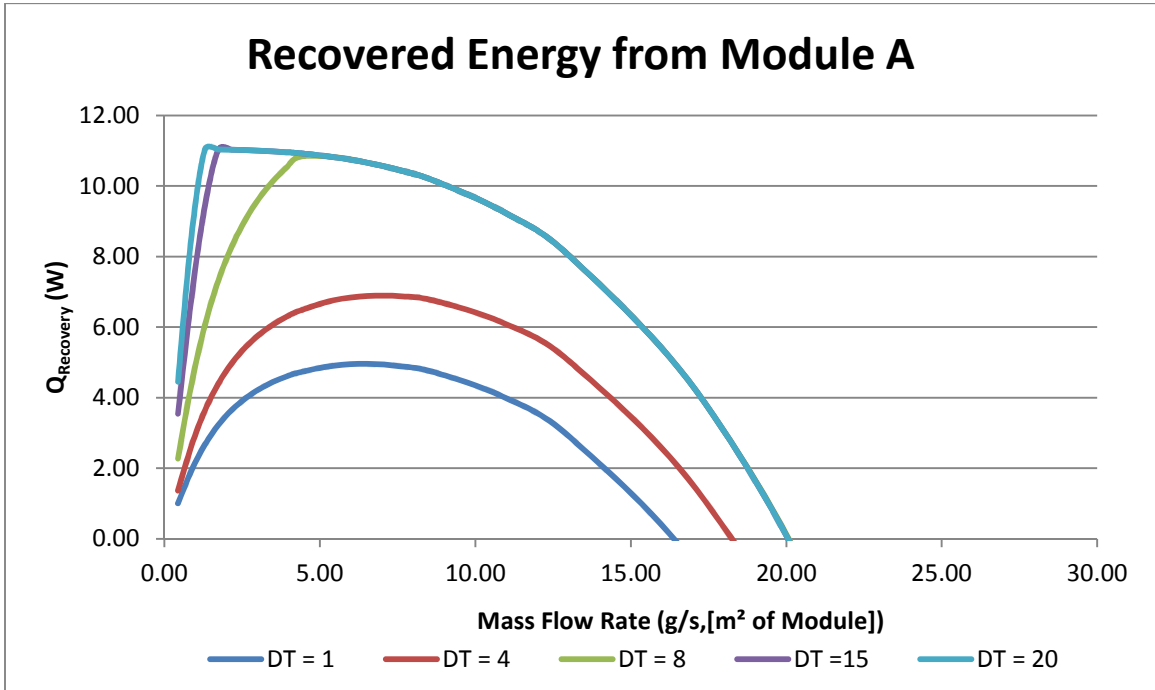
Figure 56 – Module A – Net Energy Harvest For Stipulated Weather Data
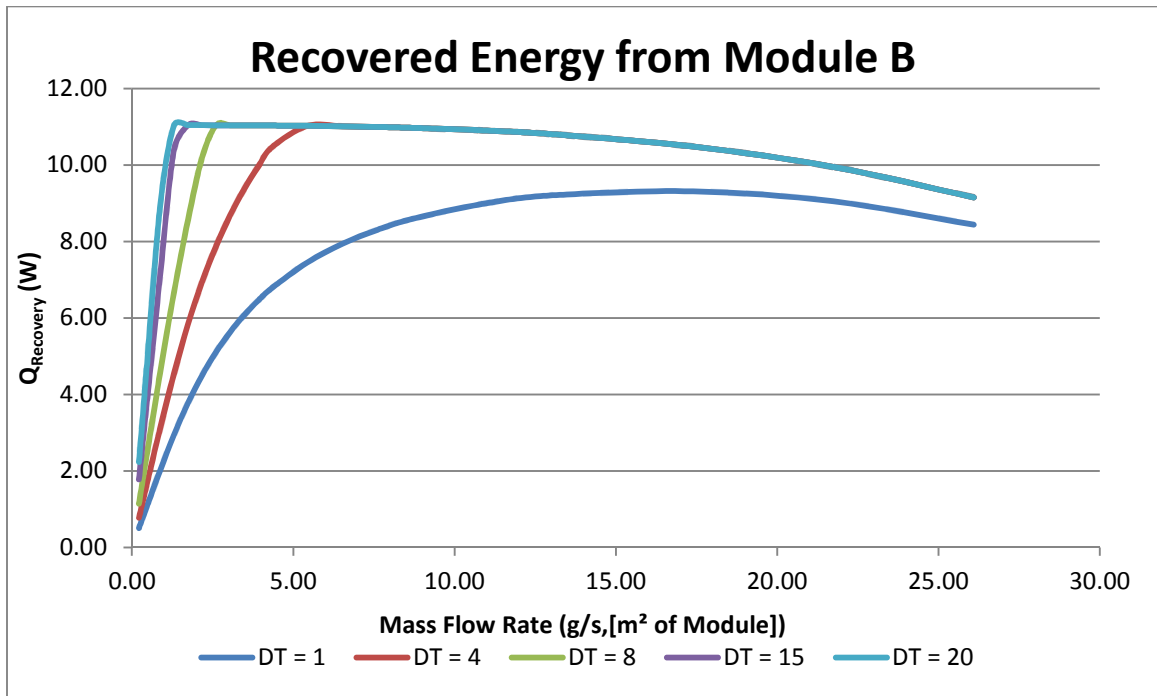
Figure 57 – Module B – Net Energy Harvest For Stipulated Weather Data
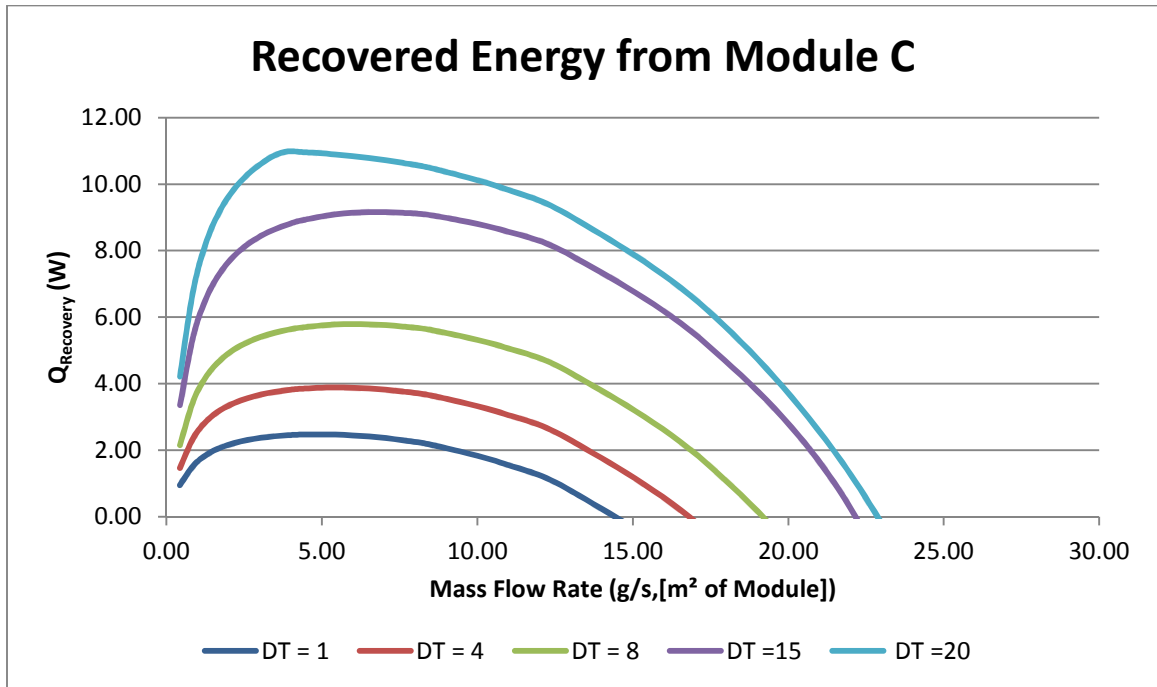
Figure 58 – Module C – Net Energy Harvest For Stipulated Weather Data

Chapter 8: Electrical Generation Model from the Heat Recovered from Collectors

For the purpose of determining if these collectors could be used to generate the higher quality energy in view as part of the justification of these systems, an organic Rankin ~~e~~Cycle (ORC) was modeled for the month of June in three US cities. These were Phoenix, Arizona, Las Vegas, Nevada, and Baltimore, Maryland. Modeling was performed using the National Renewable Laboratory (NREL) published Typical Meteorological Year 2 (TMY2) files. It is assumed that the reader is familiar with the nature of these files.

8.1 ORC System Description

The ORC was modeled with topology as shown in Figure 59. The sun provides energy to the PVT collectors. The PV electrical output is captured and converted by means of an inverter. The recovered heat is transferred into a water circulation loop and then pumped subsequently to a propane loop. It is assumed that any viable ORC working fluid will be subject to additional environmental and operational worker qualification restrictions, so the model assumes it is limited to as small an area as possible. The propane is heated by the water loop (sensibly heated from Point 2 to 3, then latent to

Point 4 and superheated to 5*), passes though a variable geometry turbine which is coupled to an alternator (passing from Point 5 to Point 6), cooled in a closed circuit cooling tower (Point 6 to Point 1), and then pumped back to high pressure (Point 1 to Point 2) to be heated again. No economizers are present in this topology.

For sake of simplicity, the following assumptions were made with respect to the ORC:

1. The working fluid is assumed to be propane.

2. The power is extracted from the PV Array with a 1°C ΔT between the water and the propane at the entrance. Other parameters for the two-flow heat exchanger are not considered.

3. The total heat passed to the propane loop is modeled according to Item 2, the technique outlined in 5.2 Corrective Parameters for the Energy Balance Model, and the cell temperatures are modeled according to Appendix B − Modeling T_{Cell} from Available Climatic Data.

4. Cooling tower efficiency is maximized at 75%. Lower efficiencies are possible, but higher efficiencies are not permitted. The efficiency η_{CT} is defined as:

$$\frac{EWT_{CT} - LWT_{CT}}{EWT_{CT} - WB} = \eta_{CT}[69]$$

8-1

---

* The reader is directed to Figure 60 – T/S Diagram for Point Labeling for a phase diagram of the ORC.

5. The variable geometry turbine is configured to accept pressures across the operating ranges provided to it by this arrangement (200kPa to 2MPa) with an isentropic efficiency of 80%[70].

6. Once the turbine captures energy, the alternator, step-up transformers, resistive losses, etc. have an efficiency of 95%, which is not unreasonable for generation on the order of 500MVA[71].

7. Controls limit losses caused by the system such that if the ORC were to capture energy from the load rather than supply it, the ORC will be disconnected and stopped. Furthermore, no losses are modeled for start-up / stop of the turbines or other equipment.

8. The T_{Cell} / LWT can be modeled according to the previous section: 4.2.7 LWT / T_{Cell} Correlation.

The following assumptions are made with respect to the electrical capture from the PV array:

1. The PV cells have an operating efficiency of 15% with no correction for G_{POA} levels with respect to their design efficiencies. Temperatures of the cells are included in the efficiency of the cells according to:

$$\eta_{Elec} = \eta_{Elec,0}\left(1 + \beta(T_{cell} - 25°C)\right)$$

8-2

2. The inverters have efficiencies of 98%[72].

3. The remainder of the BoS of the system produces a constant efficiency

of 97% (i.e. a 3% total loss: $Loss_{BoS.}$)[*]

These result in the following definition of η_{PV} and η_{PVT}:

$$\eta_{PV} = \eta_{Elec}\eta_{Inverter}(1 - Loss_{BoS})$$

8-3

$$\eta_{PVT} = \eta_{TH}\eta_{ORC}\eta_{GEN}$$

8-4

---

[*] In practice, this is a design parameter for the engineer designing the system. By increasing the size of the feeder wires or changing their lengths, these values can range widely. Further, the losses will not be constant under operation. This assumption made here is for simplification.
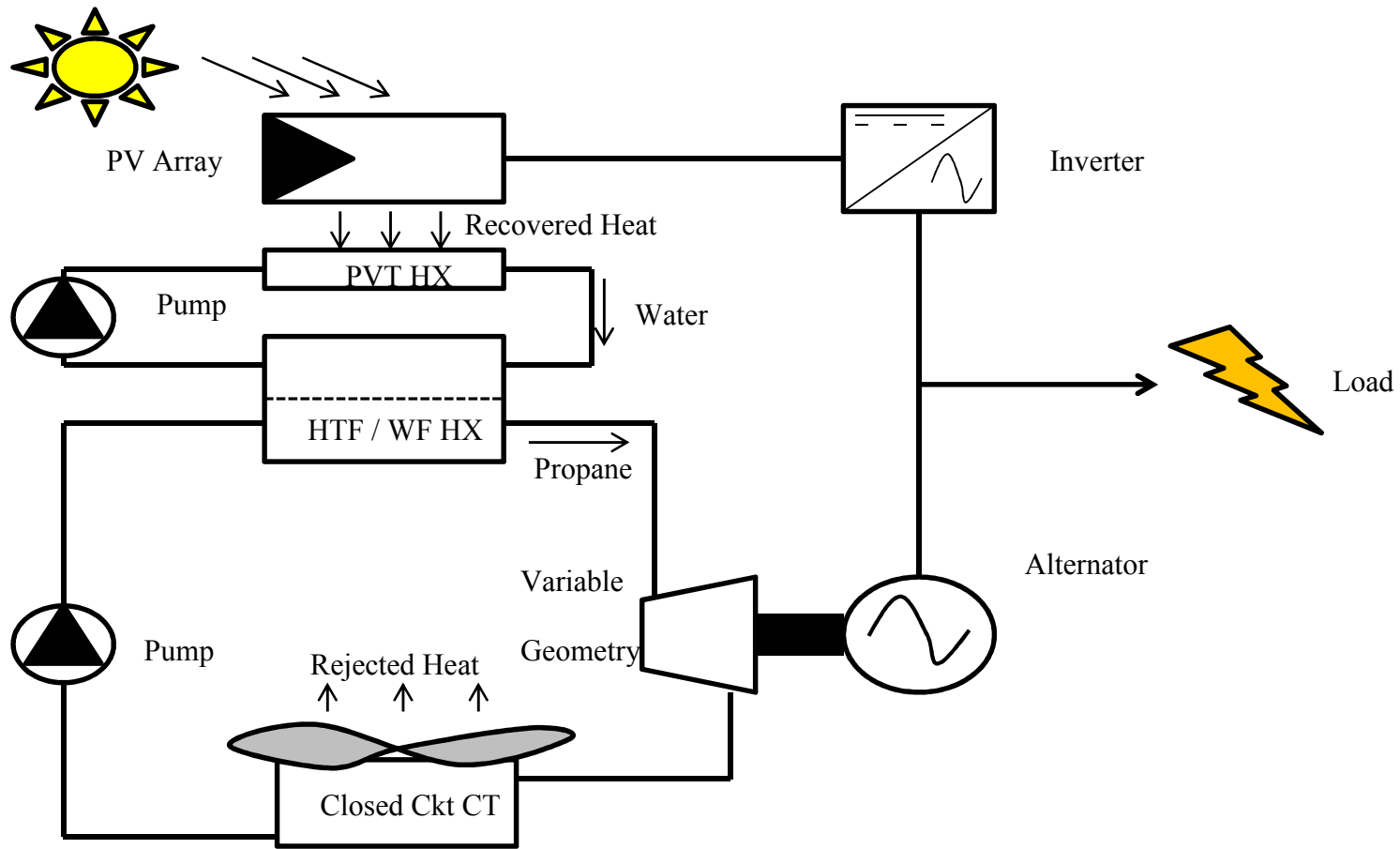
Figure 59 – ORC Topology

8.2 Simplifying Assumptions

While the cycle explained previously is well understood, it is too complex to model without simplification. Accordingly, the following assumptions were made with respect to the ORC:

1. The working fluid is assumed to be propane.

2. The power is extracted from the PV Array with a 1°C ΔT between the water and the propane at the entrance. Other parameters for the two-flow heat exchanger are not considered.

3. The total heat passed to the propane loop is modeled according to Item 2, the section Corrective Fitting of the Energy Balance Model, and the cell temperatures are modeled according to Appendix B - Modeling TCell from Available Climatic Data.

4. Cooling tower efficiency is maximized at 75%. Lower efficiencies are possible, but higher efficiencies are not permitted. The efficiency η_{CT} is defined as:

$$\frac{EWT_{CT} - LWT_{CT}}{EWT_{CT} - WB} = \eta_{CT}[73]$$

8-5

5. The variable geometry turbine is configured to accept pressures across the operating ranges provided to it by this arrangement (200kPa to 2MPa) with an isentropic efficiency of 80%[74].

6. Once the energy has been captured by the turbine, the alternator, step-up transformers, resistive losses, etc… have an efficiency of 95%, which is not unreasonable for generation on the order of 500MVA[75].

7. Controls limit losses caused by the system such that if the ORC were to capture energy from the load rather than supply it, the ORC will be disconnected and stopped. Furthermore, no losses are modeled for start-up / stop of the turbines or other equipment.

8. The T_{Cell} / LWT can be modeled according to the previous section: LWT / T_{Cell} Correlation.

The following assumptions are made with respect to the electrical capture from the PV array:

1. The PV cells have an operating efficiency of 15% with no correction for G_{POA} levels with respect to their design efficiencies. Temperatures of the cells are included in the efficiency of the cells according to:

$$\eta_{Elec} = \eta_{Elec,0}\big(1 + \beta(T_{cell} - 25°C)\big)$$

8-6

2. The inverters have efficiencies of 98%[76].

3. The remainder of the BoS of the system produces a constant efficiency

of 97% (i.e. a 3% total loss: Loss_{BoS}.)[*]

These result in the following definition of η_{PV} and η_{PVT}:

$$\eta_{PV} = \eta_{Elec}\eta_{Inverter}(1 - Loss_{BoS})$$

8-7

$$\eta_{PVT} = \eta_{TH}\eta_{ORC}\eta_{GEN}$$

8-8

These assumptions are then fed into a set of calculations for the ORC's output. See Figure 60 – T/S Diagram for Point Labeling to see the labeling for the points in this work.

---

[*] In practice, this is a design parameter for the engineer designing the system. By increasing the size of the feeder wires or changing their lengths, these values can range widely. Further, the losses will not be constant under operation. This assumption made here is for simplification.

8.3 ORC Annual Operation Calculations

8.3.1 Calculation Process

The process herein generally follows the flowchart seen in Figure 60.

The calculation starts by setting the temperature for Point 1 to be 1°C greater than the WB for that TMY record's hour (hereafter in this section called TMYhr.)
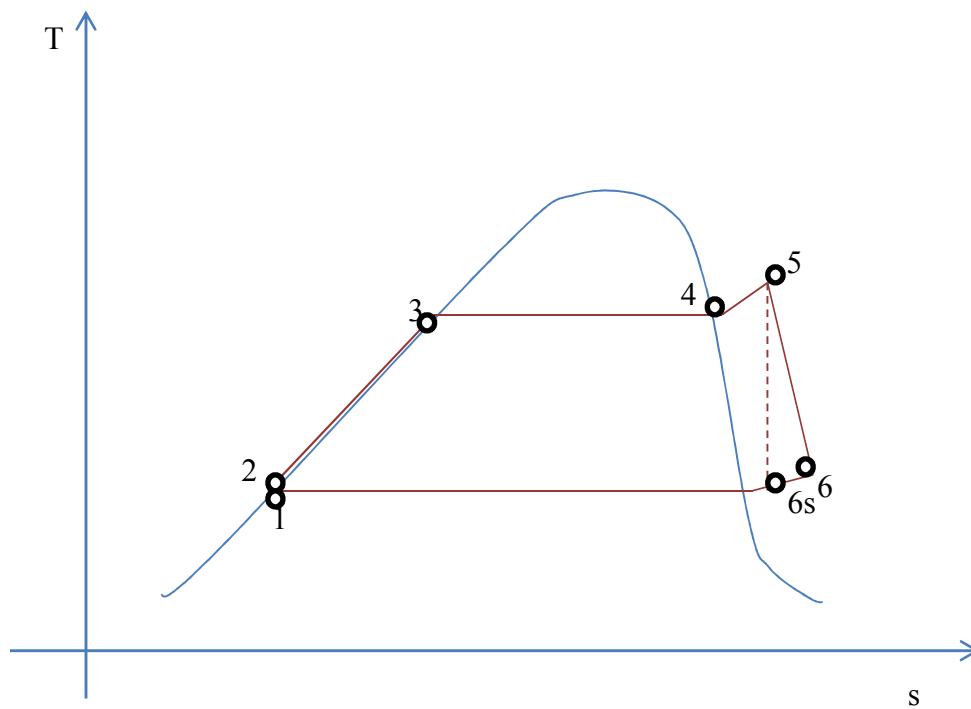
Figure 60 – T/S Diagram for Point Labeling
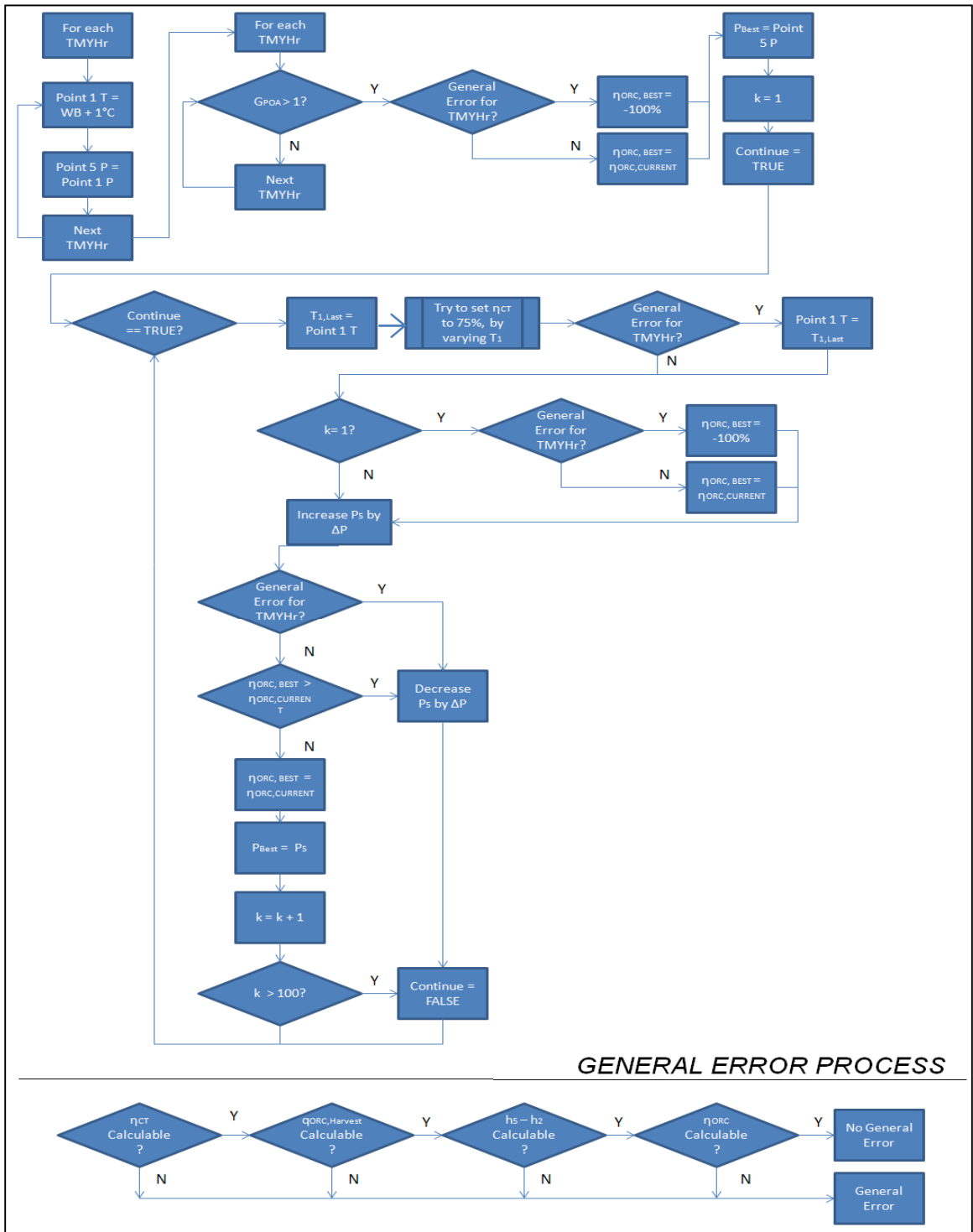
Figure 61 – ORC Configuration Process

From there, the calculation sets $P_5 = P_1$, thereby effectively setting the area under the dome to zero and removing any work that the model suggests the system will perform. After this removal of work, the algorithm processes through the TMY file, examining only the TMYhrs during which the sun is up (i.e. G_{POA} is greater than zero.)

(It should be understood that since the TMY2 files' irradiance data is indicative of energy received at the weather station's recording equipment over the course of an hour[77], the values indicated at a sunrise / sunset hour are not completely accurate as an expected "peaking output." However, the irradiance at these hours is generally low and so the difference between the energy and power is generally unimportant.)

For those TMYhrs which pass the G_{POA} test, the hour is checked for "General Error," which is a Boolean that trips under certain circumstances. These circumstances are:

1. If the η_{CT} cannot be calculated according to 7-2,

2. If the $q_{Harvest,ORC}$ cannot be calculated according to:

$$q_{Harvest,ORC} = h_5 - h_6$$

8-9

3. If the q_{Input} cannot be calculated according to:

$$q_{Input} = h_5 - h_2$$

8-10

4. If the η_{ORC} cannot be calculated according to:

$$\eta_{ORC} = \frac{h_5 - h_6}{h_5 - h_2}$$

8-11

If any of these four "cannots" are true, the General Error will be true.

116

If the General Error is true, the algorithm sets the $\eta_{ORC, BEST}$ to -100%. If it is not true, it sets the $\eta_{ORC, BEST}$ to whatever the current value of η_{ORC} is for that TMYhr.

The process then increases the pressure at P_5 by some ΔP. This ΔP is set at 10kPa. A Boolean is set to TRUE and a counter is set up (called *m*).

At this point, a loop is started. The loop will exit when the Boolean is set to FALSE. T_1 is stored in a variable and then varied to set η_{CT} to 75%. If *m* = 1 and if the General Error is true, the algorithm sets the $\eta_{ORC, BEST}$ to -100%. If it is not true, it sets the $\eta_{ORC, BEST}$ to whatever the current value of η_{ORC} is for that TMYhr. P_5 is increased by ΔP and if the η_{ORC} increases and a General Error is not triggered, then P_5 is maintained and the η_{ORC} is maintained. Else, the pressure is moved back and the next TMY value is set. If m passes 100, the Boolean is FALSE.

8.3.2 Calculation Results and Discussion

This algorithm results in some accurate values, but rejects with a higher rate than would be expected. Because this work focuses on the performance of the PVT modules and not the ORC cycles, example values are given below.

117

City	Module	Example Prod. Date / Time	Cell η	ηORC	ηTH	PV η	PVT η	η$_{Total, Elec}$[*]	PVT Boost
BWI, MD	A	12/9 12:00	15.8%	5.0%	41.0%	15.0%	2.0%	17.1%	8.2%
	B	2/11 13:00	15.5%	6.0%	42.8%	14.8%	2.5%	17.4%	12.3%
	C	1/17 12:00	14.5%	5.7%	27%	13.8%	1.5%	15.3%	5.5%
LAS, NV	A	5/12 12:00	12.5%	13.4%	29.3%	11.9%	3.9%	15.8%	26.4%
	B	6/6 12:00	13.1%	14.5%	49.8%	12.4%	7.2%	19.6%	49.6%
	C	12/27 12:00	11.9%	13.7%	19.1%	11.1%	2.6%	13.7%	15.1%
PHX, AZ	A	6/23 12:00	12.5%	13.7%	34.9%	11.9%	4.8%	16.7%	33.6%
	B	6/19 12:00	13.3%	14.7%	47.5%	12.6%	6.9%	19.5%	31.8%
	C	1/22 12:00	12.4%	16.1%	28.9%	11.8%	4.6%	16.4%	32.2%

Figure 62 – Organic Rankin Cycle Results

These values show that for arid, desert climates, the boost across different times of year is very large. In the more humid areas like the mid-Atlantic, the boost is lessened, although still substantial.

8.4 ORC Hourly Sensitivity Analysis

A further analysis was performed to determine the impact of slight changes to the assumed parameters. The slight changes were:

---

[*]. This represents the total efficiency of the power plant at the given hour.

1. Cooling Tower Efficiencies of 70% and 80% instead of 75%.

2. Isentropic Turbine Efficiency of 75% and 85% instead of 80%,

3. PV Array ΔT of 0.5°C and 1.5°C instead of 1.0°C.

These modifications were modeled in the Las Vegas site using the model described previously in this work. This results in slight changes to the ORC efficiency shown previously. These changes can be seen below.
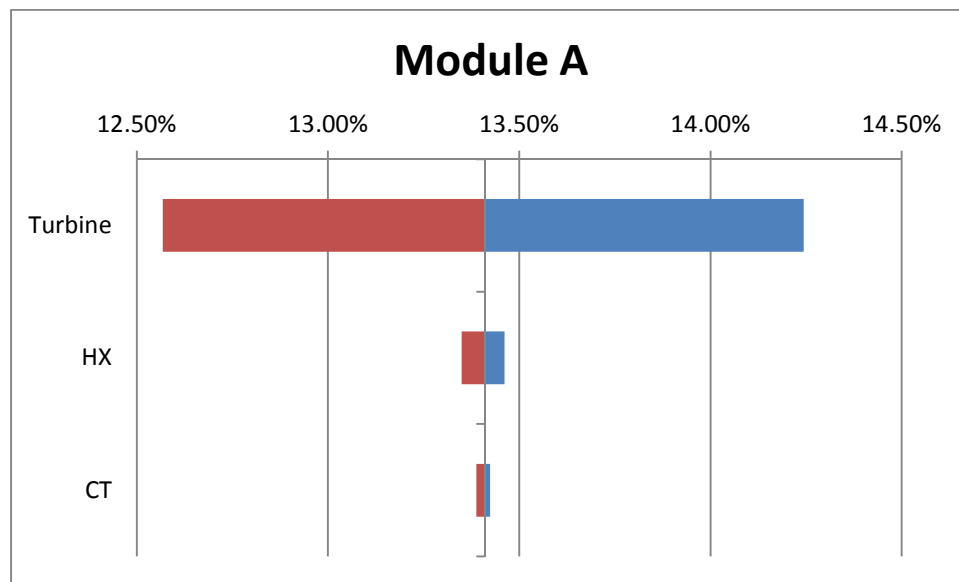
Figure 63 – Module A Sensitivity
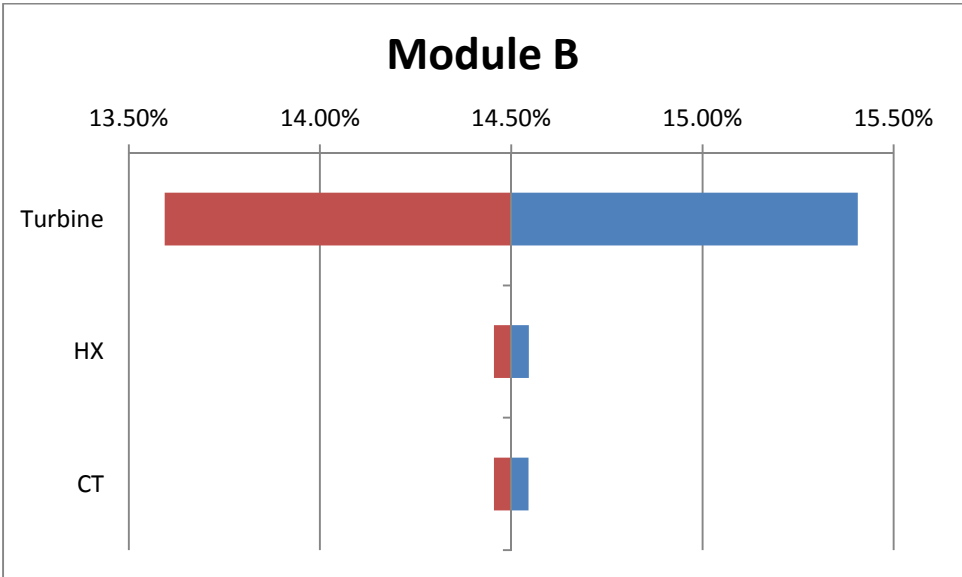
Figure 64 – Module B Sensitivity
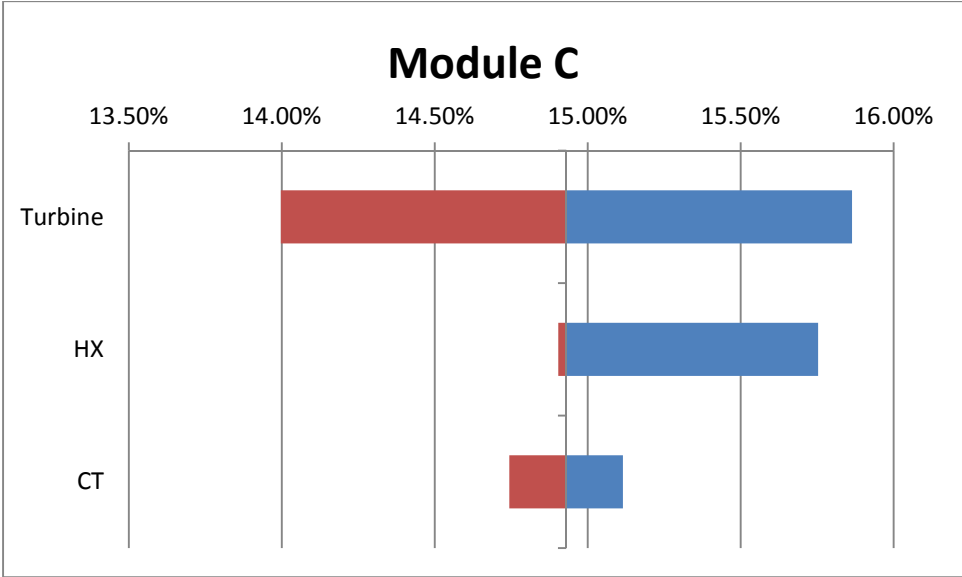
Figure 65 – Module C Sensitivity

It can be seen that the majority of the sensitivity is tied to the turbine efficiencies, with the heat exchanger providing less sensitivity. The cooling tower efficiency is a decidedly less sensitive variable.

120

Chapter 9: Framework for Economic Analysis

While this work's scope does not include a detailed examination of the economics of these systems, the following items should be included in any economic analysis of the systems envisioned herein:

1. Plant operations costs:

As a PVT system increases the moving parts, operations costs for the system will increase relative to a PV system of the same area.

2. Material Costs

The commodity prices current at the time of this work for the two metals used in construction of the PVT heat exchangers appear in Table 27. It will be noted that copper has a price over 400% greater than aluminum. This price disparity led the collector plate design to be with thermally inferior aluminum rather than copper.

Current Material Price (Jan '14)	
Aluminum	Copper
$1.76/kg	$7.43/kg

Table 27 – Metal Raw Material Prices [78] [79]

The mass of each material needed for each collector is described in Table 28 – Raw

Material Masses. The aluminum required is consistent across the different geometries with the change being present in copper as the length of tubing per unit area increases.[*]

Bulk Material per m² of Module HX		
Module	Aluminum (kg)	Copper (kg)
A	4.25	0.88
B	4.25	0.68
C	4.25	0.34

Table 28 – Raw Material Masses

From these two tables costs of the raw material for the heat exchanger designs can be estimated as seen in Table 29 – Raw Material Prices.

Raw Material Price per m² of Module			
Module	Aluminum (kg)	Copper (kg)	Total
A	$7.50	$6.51	$14.01
B	$7.50	$5.07	$12.57
C	$7.50	$2.53	$10.03

Table 29 – Raw Material Prices

These price differentials are not significant for a square meter of module given that module prices for 2012 were on the order of $1/W^{80}, meaning that a 15% efficient

---

[*] It bears mentioning that if additional geometries with more tubing were to be considered in order to reduce pumping losses and improve thermal resistances, the quantity of copper tubing required would increase or consideration would need to be made to eliminating the copper entirely in favor of aluminum. As the fraction of copper goes up, it is expected there will be some break-even point in the design where either a complete switch to aluminum with its lesser thermal properties or a reduction of the number of tubes will be required.

module of 1 m^2 would cost on the order of \$150. The \$4 difference in these collector design's raw materials then, in 2014 commodity terms, is about 2.5% at the maximum of the cost of a current module. This difference is small enough that it is judged to be a non-differentiating factor between these three specific HX geometries.

Chapter 10:   Recommended Future Work

For the purposes of furthering these findings, the following actions are recommended:

1. Deploy collectors for a full year. The collectors were generally only deployed in a single season and have not been subjected to the full temperature and irradiance swings to which normal climate would subject them.

2. The mass flows selected were chosen based on empirical results that provided good measurement of temperatures. However, to realize the potential of η_{TH}, mass flow for the collectors must be controlled. A mass controller should be included in future work to gain more control of the HTF and to confirm of the mass flow rate, pumping power rates, and η_{TH} correlations for a wider range of weather conditions.

3. Future work of scale should include more accurate means of measuring the irradiance. An on-site ISO 9060 first class pyranometer is recommended.

4. Examine changes to the collector configuration for an optimum design for future work. Suggested changes to examine are:

   1. Change the material for the PVT HX to a plastic or similar non-electrically conductive material. Back sheets for existing commercial PV module designs are generally tedlar or PVC, showing that a plastic based heat

exchanger design is viable could increase acceptance of the technology.

2. Examine the impact of spot welding the tubing onto the collector plate as opposed to epoxying the tube onto the plate. While this might substantially increase the thermal resistance, it also could reduce the time to manufacture a unit if a metal-based heat exchanger were to enter production.

3. Water is used as the HTF for these PVT collectors; but it has the problem of freezing in many climates. Work needs to be done to examine switching to a water-glycol solution, using ammonia-water solutions, or eliminating the delineation between the HTF and the working fluid in the cycle entirely and using the organic compound directly.

4. Module B performed substantially better than Module C in the low-grade ΔT cycle when Module B's lower pumping losses are included. It is expected that as more channels are integrated into the collector plate, pumping losses will decrease further as the hydraulic diameter of the channels increase. For this reason, it is recommended to examine a change in the channel construction entirely via the deployment of micro channels for the heat recovery. The reader is referred to the work of Zhang et al.[81] for work already performed on micro channels in PVT collectors. Pumping losses and material costs are likely to be important factors in any work in this area.

125

Chapter 11:   Conclusions

In comparison to the relative collector geometries, Module A (serpentine) shows a propensity to increase the pumping power requirements relative to the other geometries, but with higher thermal recovery at low ΔT. While this style of tubing is common among PVT collectors in use for domestic hot water generation, it is not recommended for operations in which electricity is generated through low-grade heat recovery, as the pumping losses substantially decrease its effectiveness.

Module B (double tube) has lower thermal resistance and pumping power requirements than A or C. Furthermore, in the pumping losses examination, its thermal harvest flattens as mass flow increases without such a sharp knee.   This should substantially improve its controllability in a real world application.   The relative costs are low enough that it is expected to perform the best economically.

Module C (single tube) shows a much higher thermal resistance than Module A or B. Its moderately better material requirements are not expected to overcome the pumping efficiency difference when it is bested.

Meanwhile in the broader space of electricity generation and thermal harvest projections, this work shows that using a simple energy balance model, it is possible to determine within uncertainty margins of 30% the heat which can be recovered from the collectors given only climatic data and the configuration of the collector taken from a

library of known geometries. It is further possible to reduce the error in the model by parameterization against known climatic values and calculated module values for G_{POA} and T_{cell} so that daily sums of hourly predicted values fall within +11%/-9%.

With these predictive capacities by the use of simulations of commonly understood low temperature heat recovery cycles, efficiency boosts of up to 49% are available. These improvements are not free from a capital installation cost standpoint; however, they are significant, provide additional grid stabilization capacity, and could reduce economic risks to system owners by reducing curtailment risks.

Appendix A – Calculation of the Angle of Incidence and Associated Module Angles

The AOI can be calculated by the following:

$$AOI = arcsin\left(-\widehat{m_x}\widehat{s_x} - \widehat{m_y}\widehat{s_y} - \widehat{m_z}\widehat{s_z}\right)$$

A-1

where $\vec{m}$ is defined by the vector normal to the surface of the module and $\vec{s}$ is defined by the calculation of the solar altitude and azimuth (α_{sol} and ζ_{sol}, respectively.) See Figure 66 for details. These are calculated by:

$$sin(\alpha_{sol}) = cos(\phi) cos(\delta_{sol}) cos(\eta_{Hour}) + sin(\phi)sin(\delta_{sol})$$

A-2

and:

$$cos(\zeta_{sol}) = \frac{sin(\alpha_{sol}) sin(\phi) - sin(\delta_{sol})}{cos(\alpha_{sol}) cos(\phi)}$$

A-3 [82]

where δ_{sol} is the solar declination which is defined by:

$$\delta_{sol} = \varepsilon_{axial}sin(DayAngle)$$

where ε_{axial} is the axial tilt of the earth (23.45°) and

$$DayAngle = \frac{360}{365}(DayOfYear - 80)$$

where DayOfYear is the count of the days of the year (such that January 1st of a non-leap year would be 1 and December 31st would be 365.) ϕ represents the site latitude (in this

128

work 39.15°) and η_{Hour} represents the hourly angle, calculated by:

$$\eta_{Hour} = 360\left(\frac{12 - t_{DECI}}{24}\right)$$

where t_{DECI} is the decimal representation of the solar hour (such that a solar hour of 13:15 would be 13.25 and of 21:55 would be 21.92.)

It should be noted that for values calculated at solar noon, ζ_{sol} is undefined and so an escape needs to be introduced into the calculation to set it equal to 0°. Additionally ζ_{sol} remains positive as solar noon is crossed in either direction. The reader should also note that ordinate degrees increase as they go clockwise from north while a radial coordinates increase as they proceed counterclockwise.

To transform α_{sol} and ζ_{sol} into $\vec{s}$, a component of unity is selected for the x-component of $\vec{s}$. Then the y-component[*] is $\arctan(\zeta_{sol}) \cdot sign(12 - t_{DECI})$ and the z-component can be found via:

$$\vec{s_z} = tan(\alpha_{sol}\left(\vec{s_x}^2 + \vec{s_y}^2\right)^{\frac{1}{2}}$$

Normalizing $\vec{s}$ provides $\hat{s}$.

---

[*] The *sign* function in y-component's definition returns -1 if the input is less than 0, +1 if the input is greater than 0, and 0 if the input is 0.
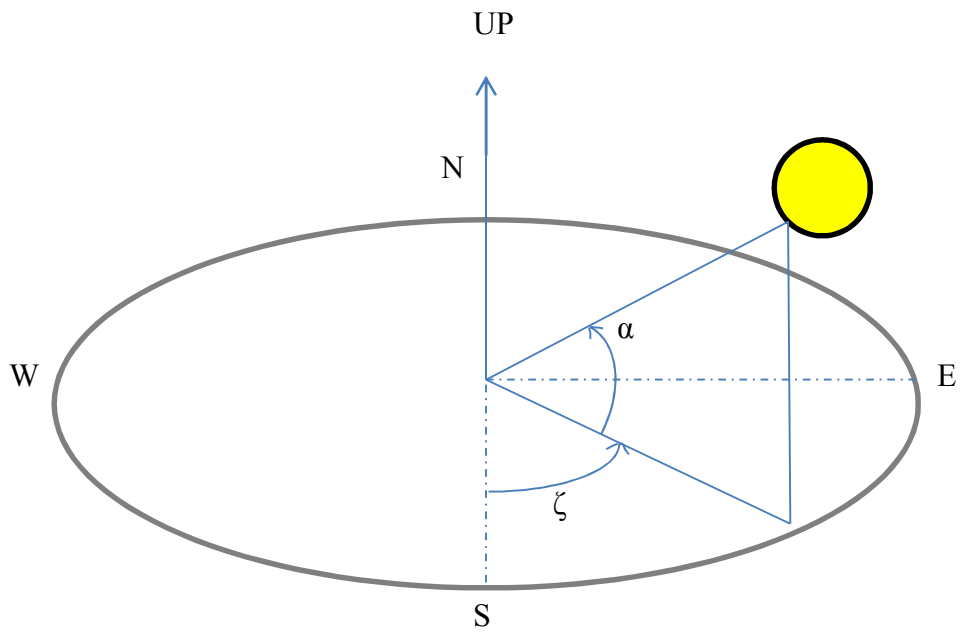
Figure 66 – Solar Position and Variables

Appendix B − Modeling T_{Cell} from Available Climatic Data

In order to calculate the laminate temperature from a given set of values, the Sandia Module Temperature Model is used with the assumption that the laminates share a common temperature. [83] This model estimates temperature as follows:

$$T_{module} = G_{POA} \, exp(a + b \times WS) + T_{amb}$$

$$B\text{-}1$$

where a and b are empirically fit parameters. A data fitting seeking to minimize the mean squared error for modeled T_{Cell} (assumed to be equivalent to T_{module}) by varying a and b against the measured values of T_{Cell} was carried out, resulting in the following values for a and b:

Module	a (unitless)	b (s/m)
A(Serpentine)	-2.43	0.163
B(Double)	-5.87	0.462
C(Single)	-2.92	0.007

Table 30 – Thermal Cell Modeling Constants

Appendix C – Module Operation Times

Start		End		Module
Date	Time	Date	Time	
7/4/13	10:41	7/6/13	15:45	A
7/6/2013	15:45	7/6/13	15:59	B
7/6/2013	15:59	7/6/13	16:25	C
7/6/2013	16:25	7/6/13	16:35	A
7/6/2013	16:35	7/6/13	17:02	B*
7/6/2013	17:02	7/6/13	17:09	A
7/6/2013	17:09	7/6/13	17:20	C
7/6/2013	17:20	7/7/13	7:30	A
7/7/2013	7:30	7/13/13	16:16	C
7/13/2013	16:16	7/18/13	20:33	B*
11/7/2013	20:15	11/9/13	17:53	B

*Module B data here is not included in the calculation of the EMB.

Glossary – List of Abbreviations and Symbols

A_{col}	Area of Collector (m^2)
AOI	Angle of Incidence
$b_{G\xi}$	Intercept of G_{POA} / $q_{OUT,H2O}$
$b_{LWT/T_{cell}}$	Intercept of LWT / T_{cell} correlation
$b_{Time\xi}$	Intercept of T_{cell} / Ξ_T correlation
$b_{T\xi}$	Intercept of T_{cell} / Ξ_G correlation
BIPVT	Building Integrated Photovoltaic Thermal
BoS	Balance of System
c_p	Specific Heat Capacity (J/kg·K)
$C_{Pressure}$	Pressure loss constant
CCGT	Combined Cycle Gas Turbine
CFD	Computational Fluid Dynamics
COP	Coefficient of Performance
DHW	Domestic Hot Water
D	Tube Diameter (mm)
DPt	Dew Point (°C or K)
DXHP	Direct Expansion Heat Pump
DXSHP	Direct Expansion Solar-Assisted Heat Pump

E_{gap}	Electron Energy Gap (eV)
$E_{gap, Ref}$	Reference Electron Energy Gap (eV)
EBM	Energy Balance Model
EWT	Entering Water Temperature (°C)
F_{earth}	View Factor of Earth from Collector
F_{sky}	View Factor of Sky from Collector
G	Acceleration due to Gravity (m/s^2)
G	Irradiance (W/m^2)
G_b	Beam Component of Irradiance (W/m^2)
$G_{Diffuse}$	Diffuse Component of Irradiance (W/m^2)
G_{DNI}	Direct Normal Irradiance (W/m^2)
G_{GHI}	Global Horizontal Irradiance (W/m^2)
G_{ground}	Ground Reflected Component of Irradiance (W/m^2)
G_{POA}	Irradiance in the Plane of Array (W/m^2)
GHG	Greenhouse Gas
h_{Conv}	Heat Transfer Coefficient (W/m^2, K)
h_{glass}	Heat Transfer Coefficient from glass surface to atmosphere (W/m^2, K)
h_i	Enthalpy in Organic Rankine Cycle Point i (kJ/kg)

HTF	Heat Transfer Fluid
HX	Heat Exchanger
I	Current (A)
I_0	Diode Saturation Current (A)
$I_{0,\ Ref}$	Reference Diode Saturation Current (A)
I_{mpp}	Max Power Point Current (A)
I_{ph}	Photocurrent (A)
I_{SC}	Short Circuit Current (A)
IAM_b	Incident Angle Modifier
k_{Air}	Thermal Conductivity of Air (W/m·K)
$k_{Aluminum}$	Thermal Conductivity of Glass (W/m·K)
k_{EVA}	Thermal Conductivity of EVA (W/m·K)
k_{glass}	Thermal Conductivity of Glass (W/m·K)
k_{Kapton}	Thermal Conductivity of Kapton (W/m·K)
k_{H2O}	Thermal Conductivity of Water (W/m·K)
k_{Si}	Thermal Conductivity of Silicon (W/m·K)
L_c	Characteristic Length (m)
LWT	Leaving Water Temperature (°C)
$\dot{m}_{H_2O}$	Mass flow of cooling water (g/s)
$\vec{m}$	Vector normal to surface of module
$m_{G\xi}$	Slope of G_{POA} / $q_{OUT,H2O}$ correlation

$m_{LWT/T_{cell}}$	Slope of LWT / T_{cell} correlation
m$_{Time\xi}$	Slope of T_{cell} / Ξ_T correlation
m$_{T\xi}$	Slope of T_{cell} / Ξ_G correlation
N$_{cells}$	Number of Cells
Nu_{L_c}	Nusselt number for characteristic length L_c
ORC	Organic Rankin Cycle
P	Power (W)
P$_i$	Pressure in Organic Rankin Cycle Point i (kPa)
PV	Photovoltaic
PVT	Photovoltaic Thermal
q$_{back, conv}$	Energy Rate convected into the air from Back (W)
q$_{electron}$	Electrical Charge of an Electron (C)
q$_{elec}$	Electrical Energy Rate from PV Cells (W)
q$_{Harvest}$	Rate of Heat Harvested From Collector (W)
q$_{Harvest, ORC}$	Rate of Heat Harvested From Collector and translated into electricity via an ORC (W)
q$_{Input}$	Rate of Heat Added to ORC via PVT Collectors (W)
q$_{NET}$	Net Power after Pumping Losses (W)

$q_{OUT,H2O}$	Energy Rate removed from Collector by HTF (W)
q_{POA}	Rate of Irradiance Incident upon the Plane of Array of the Collector (W)
q_{Pump}	Pumping power losses (W)
$q_{reflect}$	Energy Rate reflected from Collector (W)
$q_{sky, conv}$	Energy Rate convected into air from front (W)
$q_{sky, rad}$	Energy Rate radiated into Sky (W)
q_{stored}	Energy Rate of Energy Storage in Collector (W)
q_{sun}	Energy Rate from Sun (W)
$q''_{back, conv}$	Heat Flux convected into the air from Back (W/ m^2)
$q''_{cell, glass}$	Heat Flux conducted from cell to glass front (W/ m^2)
$q''_{glass, rad}$	Heat Flux radiated from glass to ambient (W/ m^2)
$q''_{reflect}$	Heat Flux reflected from Collector (W/ m^2)
$q''_{sky, conv}$	Heat Flux convected into air from front (W/ m^2)

137

$q''_{sky, rad}$	Heat Flux radiated into Sky from cell (W/ m^2)
q''_{sun}	Heat Flux from Sun (W/ m^2)
q''_{HTF}	Heat Flux into a Heat Transfer Fluid (W/m^2)
$Q_{Harvest}$	Energy Removed from Collector by HTF (J)
Q_{POA}	Energy Incident upon the Plane of Array of the Collector (J)
R^2	Pearson Coefficient
R_{series}	Series Resistance (Ω)
R_{shunt}	Shunt Resistance (Ω)
R_{Th}	Thermal Resistance (W/m^{2}K)
Ra_{L_c}	Rayleigh number for characteristic length L_c
$\vec{s}$	Solar vector extending to the Sun
S2TS	Smart and Small Thermal Systems
SDXHP	Solar Direct Expansion Heat Pump
t_{Deci}	Time of day in decimal format (hrs)
T_{Amb}	Ambient Temperature (°C or K)
T_{cell}	Cell Temperature (°C or K)
$T_{cell, Ref}$	Reference Cell Temperature (°C or K)
T_{glass}	Temperature of the Outer Surface of Glass (°C or K)

138

T_{HTF}	Heat Transfer Fluid Temperature (°C or K)
T_{Module}	Module Temperature (°C or K)
T_{Plate}	Aluminum Plate Temperature (°C or K)
T_{Sky}	Sky Temperature (°C or K)
TMY	Typical Meteorological Year
v	Velocity (m/s)
V	Voltage (V)
V_{mpp}	Maximum Power Point Voltage (V)
V_{OC}	Open Circuit Voltage (V)
V_{SC}	Short Circuit Voltage (V)
WB	Wet Bulb Temperature (°C or K)
WS	Wind Speed (m/s)
α	Thermal diffusivity (m^2/s)
α_r	Albedo of Ground
α_{sol}	Solar Altitude
β	Thermal Coefficient of Electrical Efficiency (%/K)
γ	Diode Quality Factor
δ_{cell}	Thickness of laminate (m)
δ_{glass}	Thickness of glass (m)
δ_{Kapton}	Thickness of Kapton (m)

δ_{EVA}	Thickness of EVA (m)
δ_{plate}	Thickness of aluminum plate (m)
δ_{sol}	Solar declination
Δt	Time Difference (s)
ΔP	Pressure Difference (kPa)
ΔT	Temperature Difference (°C)
ε_{atm}	Emissivity of Atmosphere
ε_{axial}	Axial Tilt of the Earth
ε_{glass}	Emissivity of Glass
$\varepsilon_{p\text{-}Si}$	Emissivity of Polysilicon
ζ_{sol}	Solar Azimuth
η_{CT}	Cooling Tower Efficiency (%)
η_{Elec}	Electrical Efficiency (%)
$\eta_{Elec, Ref}$	Reference Electrical Efficiency (%)
η_{GEN}	Generator Efficiency (%)
η_{ORC}	Organic Rankin Cycle Efficiency (%)
η_{Pump}	Pumping Efficiency (%)
η_{PV}	Contribution of PV to $\eta_{Total,Elec}$ (%)
η_{PVT}	Contribution of PVT to $\eta_{Total,Elec}$ (%)
η_{TH}	Thermal Efficiency (%)
$\eta_{TH, Max}$	Thermal Efficiency Limit (%)

η_{TOTAL}	Total Efficiency (Electrical plus Thermal) (%)
$\eta_{TOTAL, Elec}$	Total Efficiency from PV and PVT in electrical generation application (%)
θ_{Tilt}	Collector Tilt
$\mu_{I_{SC}}$	Short Circuit Temperature Coefficient (A/K)
ν	Kinematic Viscosity (m^2/s)
ρ	Density (kg/m^3)
ξ_G	Estimated Irradiance Correction Parameter (W)
ξ_T	Estimated Temperature Correction Parameter (W)
ξ_{Time}	Estimated Time Correction Parameter (W)
Ξ_G	Irradiance Correction Parameter (W)
Ξ_T	Temperature Correction Parameter (W)\
Ξ_{Time}	Time Correction Parameter (W)\
σ	Stefan Boltzmann Constant (W/m^2,K^4)
τ	Transmission of Glass
τ_α	Transmission Absorption factor
Φ	Latitude

141

Bibliography

1   "Solar market insight report 2014 Q3". SEIA, December 9, 2014. Web. December 15, 2014. <http://www.seia.org/research-resources/solar-market-insight-report-2014-q3>

2   "The mix of fuels used for electricity generation in the United States is changing". Energy Information   Administration,   November   8,   2013.   Web.   January   1,   2014. <http://www.eia.gove/todayinenergy/detail.cfm?id=13731>

3   Zhang, X., X. Zhao, S. Smith, J. Xu, and X. Yu. (2012) Review of R&D progress and practical application of the solar photovoltaic thermal (PV/T) technologies. *Renewable and Sustainable Energy Reviews* **16**, 599-617.

4   "The mix of fuels used for electricity generation in the United States is changing". Energy Information   Administration,   November   8,   2013.   Web.   January   1,   2014. <http://www.eia.gove/todayinenergy/detail.cfm?id=13731>

5   Perez, R., T. Hoff, C. Herig, J. Shah. (2003) Maximizing PV peak shaving with solar load control: validation of a web-based economic evaluation tool. Solar Energy 74, 409-415.

6   "Federal Business Energy Investment Tax Credit (ITC)". North Carolina State University, n.d. Web.   October   5,   2013. <http://www.dsireusa.org/incentives/incentive.cfm?Incentive_Code=US02F&re=1&ee=1>

7   "Most Efficient Solar from SunPower ®". SunPower Corporation, n.d. Web. October 5, 2013. <http://us.sunpowercorp.com/about/sunpower-technology/most-efficient-solar/>.

8   Kanellos,   Michael.   "SunPower   Announces   Efficiency   Record: Is   the   End   Near?". greentechmedia,   June   23,   2010.   Web.   October   5,   2013. <http://www.greentechmedia.com/articles/read/sunpower-announces-efficiency-record-is-the-end-near>.

9   "Sunmodule ® Plus SW 275 mono". SolarWorld Americas, n.d. Web. October 5, 2013. <http://www.solarworld-usa.com/~/media/www/files/datasheets/sunmodule-plus/sunmodule-solar-panel-275-mono-ds.pdf>.

10   "DOE-Funded Solar Variability Model in High Demand in Puerto Rico". U.S. Department of Energy,   October   12,   2012.   Web.   October   5,   2013. <https://solarhighpen.energy.gov/article/doe_funded_solar_variability_model_high_demand_puerto_rico>.

11   Barbose, G. N. Darghouth, S. Weaver, and R. Wiser. Tracking the Sun VI: An Historical Summary of the Installed Price of Photovoltaics in the United States from 1998 to 2012. Berkley, CA.: Lawrence Berkley National Laboratory.

12   Zhang, X., X. Zhao, S. Smith, J. Xu, and X. Yu. (2012) Review of R&D progress and practical application of the solar photovoltaic thermal (PV/T) technologies. *Renewable and Sustainable Energy Reviews* **16**, 599-617.

13   Shockley, W. and H. Queisser. (1961) Detailed Balance Limit of Efficiency of p-n Junction Solar Cells. J. Applied Physics **32**, 510-519.

14   Kumar, K and M. Rosen. (2011) A critical review of photovoltaic-thermal collectors for air-heating. Applied Energy **88**, 3603-3614.

15   Barbose, G. N. Darghouth, S. Weaver, and R. Wiser. Tracking the Sun VI: An Historical Summary of the Installed Price of Photovoltaics in the United States from 1998 to 2012. Berkley, CA.: Lawrence Berkley National Laboratory.

16   "Large Solar Energy Projects." California Energy Commission, September 14, 2012. Web. October 9, 2013. <http://www.energy.ca.gov/siting/solar/>.

17   Randolph, Edward. "Advice Letter Filing of PG&E's Third Renewable Auction Mechanism Power Purchase Agreements". San Francisco: State of California - Public Utilities Commission, 29 May 2013. Print. <http://www.pge.com/nots/rates/tariffs/tm2/pdf/ELEC_4216-E.pdf>.

18   "Generator Interconnection Process Workshop." Southern California Edison, July 11, 2011. Web. October   9,   2011.   <https://www.sce.com/wps/wcm/connect/25696eeb-d5d5-4e81-852e-2472988ea45d/GeneratorInterconnctionProcessWorkshop.pdf?MOD=AJPERES&CACHEID=25696eeb-d5d5-4e81-852e-2472988ea45d>.

19   Cheszes, Jonathan. "Impact of Curtailment on Wind Economics." Renewable Energy World, March   20,   2012.   Web.   October   9,   2013. <http://www.renewableenergyworld.com/rea/news/article/2012/03/impact-of-curtailment-on-wind-economics>.

20   Zhang, X., X. Zhao, S. Smith, J. Xu, and X. Yu. (2012) Review of R&D progress and practical application of the solar photovoltaic thermal (PV/T) technologies. *Renewable and Sustainable Energy Reviews* **16**, 599-617.

21   Bergene, T., O. Løvvik (1995) Model Calculations on a Flat-Plate Solar Heat Collector with Integrated Solar Cells. *Solar Energy* **55** (6), 453-462.

22   Zondag, H., D. de Vries, W. van Helden, R. van Zolingen, A. van Steenhoven (2002) The Thermal and Electrical Yield of a PV-Thermal Collector. *Solar Energy* **72** (2), 113-128.

23   Zhang, X., X. Zhao, S. Smith, J. Xu, and X. Yu. (2012) Review of R&D progress and practical application of the solar photovoltaic thermal (PV/T) technologies. *Renewable and Sustainable Energy Reviews* **16**, 599-617.

24   Cristofari, C., J. Canaletti, G. Notton, C. Daras (2012) Innovative patented PV/TH Solar Collector: optimization and performance evaluation. *Energy Procedia* **14**, 235-240.

25   Hegenzy, A. (2000) Comparative study of the performances of four photovoltaic / thermal solar air collectors. *Energy Conversion and Management* **41**, 861-881.

26   Corbin, C., Z. Zhai (2010) Experimental and numerical investigation on thermal and electrical performance of a building integrated photovoltaic-thermal collector system. *Energy and Buildings* **42**, 76-82.

27   Chow, T. (2003) Performance analysis of photovoltaic-thermal collector by explicit dynamic model. *Solar Energy* **75**, 143-152.

28   Sandnes, B., J. Rekstad (2002) A Photovoltaic / Thermal (PV/T) Collector with a Polymer Absorber Plate. Experimental Study and Analytical Model. *Solar Energy* **72** (1), 63-72.

29   Chow, T., W. He, J. Ji (2006) Hybrid photovoltaic-thermosyphon water heating system for residential application. *Solar Energy* **80**, 298-306.

30   Charkakambous, P., G. Maidment, S. Kalagiron, K. Yiakournetti (2007) Photovoltaic Thermal (PV/T) collectors: A Review. *Applied Thermal Engineering* **27**, 275-286.

31   Ito, I., N. Miura, Y. Takano (2005) Studies of Heat Pumps Using Direct Expansion Type Solar Collectors. *Transactions of the ASME* **127**, 60-64.

32   Tripanagnostopoulos, Y., Th. Nousia, M. Souliotis, P. Yianoulis (2002) Hybrid Photovoltaic / Thermal Solar Systems. *Solar Energy* **72** (3), 217-234.

33   Joshi, A., A. Tiwari, G. Tiwari, I. Dincer, B. Reddy (2009) Performance evaluation of a hybrid

photovoltaic thermal (PV/T) (glass-to-glass) system. *International Journal of Thermal Sciences* **48**, 154-164.

[34] Kalogirou, S., Y. Tripanognostopoulos (2006) Hybrid PV/T solar systems for domestic hot water and electricity production. *Energy Conversion and Management* **47**, 3368-3382.

[35] Garg, H., R. Agarwal (1994) Some aspects of PV/T collector/forced circulation flat plate solar water heater with solar cells. *Energy Conversion Management* **36**, (2) 87-99.

[36] Ji, J., H. He, T. Chow, G. Pei, W. He, K. Liu (2009) Distributed dynamic modeling and experimental study of PV evaporator in a PV/T solar assisted heat pump. *International Journal of Heat and Mass Transfer* **52**, 1365-1373.

[37] Zhao, X., X. Zhang, S. Riffat, Y. Su (2011) Theoretical study of the performance of a novel PV/e roof module for heat pump operation. *Energy Conversion and Management* **52**, 603-614.

[38] Tonui, J., Y Tripanagnostopoulos (2007) Improved PV/T solar collectors with heat extraction by forced or natural air circulation. *Renewable Energy* **32**, 623-637.

[39] Dubey, S., G. Sandhi, G. Tiwari (2009) Analytical expression for electrical efficiency of PV/T hybrid air collector. *Applied Energy* **86**, 697-705.

[40] Ji, J., H. He, T. Chow, G. Pei, W. He, K. Liu (2009) Distributed dynamic modeling and experimental study of PV evaporator in a PV/T solar-assisted heat pump. *International Journal of Heat and Mass Transfer* **52**, 1365-1373.

[41] Otanicar, T., I. Chowdhury, P. Phelan, R. Prasher (2010) Parametric Analysis of a Coupled Photovoltaic/Thermal Concentrating Solar Collector for Electricity Generation. *J. Applied Physics* **108**, 114907.

[42] American Society of Heating, Refrigerating, and Air-Conditioning Engineers. *2000 ASHRAE Handbook – Heating, Ventilating, and Air-Conditioning Systems and Equipment.* Atlanta: American Society of Heating, Refigerating, and Air-Conditioning Engineers, Inc., 2000. Print.

[43] Mermoud, Andrè. "PV modules modeling." Sandia National Laboratories, n.d. Web. October 11, 2013. <http://energy.sandia.gov/wp/wp-content/gallery/uploads/Mermoud_PVSyst.pdf>.

[44] Mermoud, Andrè. "PV modules modeling." Sandia National Laboratories, n.d. Web. October 11, 2013. <http://energy.sandia.gov/wp/wp-content/gallery/uploads/Mermoud_PVSyst.pdf>.

[45] De Soto, W., S. Klein, W. Beckman (2006) Improvement and validation of a model for photovoltaic array performance. *Solar Energy* **80**, 78-88.

[46] Mermoud, Andrè. "PV modules modeling." Sandia National Laboratories, n.d. Web. October 11, 2013. <http://energy.sandia.gov/wp/wp-content/gallery/uploads/Mermoud_PVSyst.pdf>.

[47] Mermoud, Andrè. "PV modules modeling." Sandia National Laboratories, n.d. Web. October 11, 2013. <http://energy.sandia.gov/wp/wp-content/gallery/uploads/Mermoud_PVSyst.pdf>.

[48] Tonui, J., Y. Tripanagnostopoulos (2007) Improved PV/T solar collectors with hear extraction by forced or natural air circulation. *Renewable Energy* **32**, 623-637.

[49] Zondag, H., D. de Vries, W. van Helden, R. van Zolingen, A. van Steenhoven (2002) The Thermal and Electrical Yield of a PV-Thermal Collector. *Solar Energy* **72** (2), 113-128.

[50] Garg, H., R. Argrwal (1995) Some Aspects of a PV/T Collector / Forced Circulation Flat Plate Solar Water Heater with Solar Cells. *Energy Conversion and Management* **36** (2), 87-99.

[51] Santbergen, R. "Optical Absorbtion Factor of Solar Cells for PVT Systems." Doctoral Dissertation, Technische Universiteit Eindhoven, 2008.

[52] "POA Beam." Sandia National Laboratories, n. d. Web. October 17, 2013. <http://pvpmc.org/modeling-steps/incident-irradiance/plane-of-array-poa-irradiance/calculating-poa-irradiance/poa-beam/>

[53]   For an in-depth description, see pages 30.15-30.17 of:

American Society of Heating, Refrigerating, and Air-Conditioning Engineers. *2001 ASHRAE Handbook – Fundamentals.* Atlanta: American Society of Heating, Refrigerating, and Air-Conditioning Engineers, Inc., 2001. Print. or Appendix A - Calculation of the Angle of Incidence and Associated Module Angles

[54]   "Isotropic Sky Diffuse Model." Sandia National Laboratories, n. d. Web.   October 17, 2013. <http://pvpmc.org/modeling-steps/incident-irradiance/plane-of-array-poa-irradiance/calculating-poa-irradiance/poa-sky-diffuse/isotropic-sky-diffuse-model/>

[55]   "POA Ground Reflected." Sandia National Laboratories, n. d. Web. October 17, 2013. <http://pvpmc.org/modeling-steps/incident-irradiance/plane-of-array-poa-irradiance/calculating-poa-irradiance/poa-ground-reflected/>

[56]   "ASHRAE Model."   Sandia National Laboratories, n. d. Web. October 17, 2013.<http://pvpmc.org/modeling-steps/shading-soiling-and-reflection-losses/incident-angle-reflection-losses/ashre-model/>

[57]   Zondag, H., D. de Vries, W. van Helden, R. van Zolingen, A. van Steenhoven (2002) The Thermal and Electrical Yield of a PV-Thermal Collector. *Solar Energy* **72** (2), 113-128.

[58]   "E-8.5.2 Horizontal Plates." *The Handbook of Mechanical Engineering*. Piscataway, New Jersey: Research and Education Association, 2004. Print.

[59]   "E-8.5.2 Horizontal Plates." *The Handbook of Mechanical Engineering*. Piscataway, New Jersey: Research and Education Association, 2004. Print.

[60] "ESL Global Monitoring Division – GRAD Group." National Oceanic and Atmospheric Administration, n. d. Web. September 13, 2014.< http://www.esrl.noaa.gov/gmd/grad/isis/ste.html>

[61] "Pyranometer   Classification."   Middleton   Solar,   n.d.   Web.   September   13,   2014. <http://www.middletonsolar.com/documents/PyrClass.pdf>

[62] "The Eppley Laboratory – Normal Incidence Pyrheliometer." The Eppley Laboratory, Inc., n.d. Web. September 13, 2014. <http://www.eppleylab.com/instrumentation/normal_incidence_pyrheliometer.htm>

[63] Caldwell, D. B, (2010) NATIONAL WEATHER SERVICE INSTRUCTION 10-1301 Operations and Services Surface Observing Program (Land\. National Weather Service.

[64] Santbergen, R. *Optical Absorption Factor of Solar Cells for PVT Systems*. Diss. Technische Universiteit Eindhoven, 2008. Eindhoven: Eindhoven University Press, 2008. Print.

[65] American Society of Heating, Refrigerating, and Air-Conditioning Engineers. *2003 ASHRAE Handbook – Heating, Ventilating, and Air Conditioning Applications.* Atlanta: American Society of Heating, Refrigerating, and Air-Conditioning Engineers, Inc., 2003. Print.

[66] Zondag, H., D. de Vries, W. van Helden, R. van Zolingen, A. van Steenhoven (2002) The Thermal and Electrical Yield of a PV-Thermal Collector. Solar Energy 72 (2), 113-128.

[67] Bergene, T., O. Løvvik (1995) Model Calculations on a Flat-Plate Solar Heat Collector with Integrated Solar Cells. *Solar Energy* **55** (6), 453-462.

[68] Bell and Gosset. *In-Line Mounted Centrifugal Pump Performance Curves.* Morton, IL: ITT Industries, 2000. Print.

[69] "Cooling Tower Efficiency"   The Engineering Toolbox, n. d. Web.   December 27, 2013. <http://www.engineeringtoolbox.com/cooling-tower-efficiency-d_699.html/>

[70] Lindeburg, Michael R. *Mechanical Engineering Reference Manual for the PE Exam Twelfth Edition.* Belmont, CA: Professional Publications, Inc. 2006. Print.

[71] Fink, Donald G., H. Wayne Beaty. *Standard Handbook for Electrical Engineers*. New York: McGraw Hill. 1987. Print.

[72] *List of Eligible Inverters per SB1 Guidelines*. State of California, California Energy Commission, &

California Public Services Commission, 2013. Web. January 2, 2014

[73] "Cooling Tower Efficiency" The Engineering Toolbox, n. d. Web. December 27, 2013. <http://www.engineeringtoolbox.com/cooling-tower-efficiency-d_699.html/>

[74] Lindeburg, Michael R. *Mechanical Engineering Reference Manual for the PE Exam Twelfth Edition.* Belmont, CA: Professional Publications, Inc. 2006. Print.

[75] Fink, Donald G., H. Wayne Beaty. *Standard Handbook for Electrical Engineers*. New York: McGraw Hill. 1987. Print.

[76] *List of Eligible Inverters per SB1 Guidelines*. State of California, California Energy Commission, & California Public Services Commission, 2013. Web. January 2, 2014

[77] Marion, W. and K. Urban. User's Manual for TMY2s – Typical Meteorological Years; Derived from the 1961 – 1990 National Solar Radiation Data Base. National Renewable Energy Laboratory, Golden Colorado. 1995.

[78] "Copper Prices and Copper Price Charts" Infomine, January 4, 2014. Web. January 4, 2014. <http://www.infomine.com/investment/metal-prices/copper/>

[79] "Aluminum Prices and Aluminum Price Charts" Infomine, January 4, 2014. Web. January 4, 2014. <http://www.infomine.com/investment/metal-prices/aluminum/>

[80] Barbose, G. N. Darghouth, S. Weaver, and R. Wiser. Tracking the Sun VI: An Historical Summary of the Installed Price of Photovoltaics in the United States from 1998 to 2012. Berkley, CA.: Lawrence Berkley National Laboratory.

[81] Zhang, X., X. Zhao, S. Smith, J. Xu, and X. Yu. (2012) Review of R&D progress and practical application of the solar photovoltaic thermal (PV/T) technologies. *Renewable and Sustainable Energy Reviews* **16**, 599-617.

[82] American Society of Heating, Refrigerating, and Air-Conditioning Engineers. *2001 ASHRAE Handbook – Fundamentals.* Atlanta: American Society of Heating, Refigerating, and Air-Conditioning Engineers, Inc., 2001. Print.

[83] "Sandia Module Temperature Model." Sandia National Laboratories, n. d. Web. November 2, 2013. <http://pvpmc.org/modeling-steps/cell-temperature-2/module-temperature/sandia-module-temperature-model/>